

EXTENDED LIFETIME AND INCREASED ENERGY DENSITY STUDIES
FOR LI-ION CELLS

by

Lauren M. Thompson

Submitted in partial fulfilment of the requirements
for the degree of Doctor of Philosophy

at

Dalhousie University
Halifax, Nova Scotia
August 2021

© Copyright by Lauren M. Thompson, 2021

To my families and friends in Nova Scotia, Maine, and beyond

TABLE OF CONTENTS

LIST OF FIGURES	vi
ABSTRACT.....	ix
LIST OF ABBREVIATIONS AND SYMBOLS USED	x
ACKNOWLEDGEMENTS	xiii
CHAPTER 1 – INTRODUCTION	1
<i>Motivation.....</i>	<i>1</i>
<i>Overview of Li-ion Cells.....</i>	<i>2</i>
<i>Positive Electrode.....</i>	<i>3</i>
<i>Negative Electrode.....</i>	<i>5</i>
<i>Surface Coatings.....</i>	<i>6</i>
<i>Electrolyte.....</i>	<i>6</i>
<i>Degradation Mechanisms.....</i>	<i>7</i>
<i>Improving Li-ion Cells.....</i>	<i>8</i>
CHAPTER 2 – BACKGROUND.....	9
<i>Electrolyte Components.....</i>	<i>9</i>
<i>SEI.....</i>	<i>11</i>
<i>Electrolyte Reactions Overview.....</i>	<i>12</i>
<i>Electrolyte Reduction.....</i>	<i>12</i>
<i>Electrolyte Oxidation.....</i>	<i>15</i>
<i>Polymerization.....</i>	<i>17</i>
<i>Salt Reactivity.....</i>	<i>17</i>
<i>Crosstalk.....</i>	<i>18</i>
<i>Recent Electrolyte Studies.....</i>	<i>19</i>
<i>Oligomerization of Electrolyte.....</i>	<i>21</i>
<i>Electrolyte and Electrode Reactions.....</i>	<i>24</i>
CHAPTER 3 – METHODS	29
<i>Cell Specifications.....</i>	<i>29</i>
<i>General Electrolyte Mixing.....</i>	<i>30</i>

<i>General Cell Filling, Electrode Wetting, and Formation</i>	31
<i>Gas Measurements</i>	32
<i>EIS Measurements</i>	33
<i>General Cell Cycling</i>	35
<i>General Cell Storage</i>	37
<i>UHPC Cell Cycling</i>	37
<i>UHPC Differential Voltage Analysis</i>	38
<i>DTA</i>	40
<i>Electrolyte Sample Preparation for Analysis After Cycling or Storage</i>	41
<i>NMR Principles</i>	42
<i>NMR Specifications</i>	45
<i>GC-MS Principles</i>	46
<i>GC-MS Sample Preparation</i>	48
<i>GC-MS specifications</i>	48
<i>Calculation for Salt Concentration and Error</i>	49
<i>XRF Principles</i>	50
<i>μXRF Specifications</i>	52
CHAPTER 4 – ELECTROLYTE AND ELECTRODE STUDY VERSUS TIME...	53
<i>Motivation for Studying Long-Term Electrolyte Changes</i>	53
<i>Cells and Electrolytes in this Study</i>	55
<i>Cycling and Storage</i>	56
<i>Cell Cycling Results</i>	56
<i>Capacity, Voltage Polarization, Gas and Charge Transfer Impedance Results</i>	58
<i>EIS and dV/dQ Results</i>	64
<i>Electrolyte and Negative Electrode Analysis</i>	71
<i>DTA Results</i>	81
<i>Transesterification and Gas Production</i>	88
<i>Transition Metal Ratio on Neg. Electrode</i>	90
<i>Summary</i>	98

CHAPTER 5 – HIGH LOADING CELL STUDY.....	101
<i>Motivation and Additional Background</i>	<i>101</i>
<i>Cell Specifications</i>	<i>104</i>
<i>Electrolyte.....</i>	<i>104</i>
<i>Cell Formation.....</i>	<i>105</i>
<i>EIS Measurements</i>	<i>105</i>
<i>UHPC Cycling.....</i>	<i>106</i>
<i>Cell Cycling</i>	<i>106</i>
<i>UHPC Cycling Results.....</i>	<i>107</i>
<i>UHPC Gas Production.....</i>	<i>109</i>
<i>Long-Term Cycling Results</i>	<i>111</i>
<i>EIS Spectra after Cycling</i>	<i>118</i>
<i>Summary</i>	<i>119</i>
CHAPTER 6 – CONCLUSION.....	121
<i>Conclusions.....</i>	<i>121</i>
<i>Future Work.....</i>	<i>122</i>
REFERENCES.....	128
APPENDIX A – SUPPLEMENTAL FIGURES	142
APPENDIX B – TABLE OF CHEMICALS	158
APPENDIX C – COPYRIGHT STATEMENT	159

LIST OF FIGURES

Figure 1-1 – Schematic of a Li-ion cell.....	3
Figure 2-1 – Examples of reduction pathways for linear carbonate electrolytes.....	13
Figure 2-2 – Example of reduction pathways for EC	14
Figure 2-3 – Possible reduction pathways of FEC	14
Figure 2-4 – Proposed reduction mechanism for DTD.....	14
Figure 2-5 – Proposed oxidation reaction for EC	15
Figure 2-6 – Recent proposed mechanism for EC oxidation via O ₂	16
Figure 2-7 – Oxidation of linear carbonate via O ₂	16
Figure 3-1 – Example of formation protocol	32
Figure 3-2 – Example of equivalent circuit used for EIS fitting.....	35
Figure 3-3 – Example EIS spectra from models with and without CPE	35
Figure 3-4 – Example of cycling protocols.....	36
Figure 3-5 – Example of potential versus capacity curves from dV/dQ analysis.....	39
Figure 3-6 – Schematic showing spin, precessing motion, the net magnetic moment in applied magnetic field	43
Figure 3-7 – Schematic of magnetic moment orientation with and without external magnetic field and with and without 90° pulse.	43
Figure 3-8 – Example ¹ H-NMR spectra	45
Figure 3-9 – Schematic of a GC coupled to a MS	47
Figure 3-10 – Mechanism of fluorescent X-ray generation.....	51
Figure 4-1 – Capacity versus cycle number results for NMC532 and NMC622 cells at various temperatures and with various upper cutoff potentials.....	57
Figure 4-2 – Capacity and impedance results from NMC532 cells.....	59
Figure 4-3 – Capacity and impedance results from NMC622 cells.....	62
Figure 4-4 – Post-cycling/storage results from NMC532 and NMC622 cells.....	65

Figure 4-5 – Electrode and electrolyte analysis results	72
Figure 4-6 – Summary of DTA effects from electrolyte modification.....	82
Figure 4-7 – Results from DTA of NMC532 cells tested at 40 °C.....	84
Figure 4-8 – Results from DTA of NMC532 cells stored at 55 °C.....	85
Figure 4-9 – The effect of EC content on the liquidus temperature.....	86
Figure 4-10 – The effect on the liquidus temperature of the change in EC.....	87
Figure 4-11 – The fraction of transesterification versus measured gas produced in NMC532 cells	88
Figure 4-12 – The fraction of transesterification versus measured gas produced in NMC622 cells	89
Figure 4-13 – The Ni concentration versus Mn concentration measured on the negative electrodes from NMC532 cells.....	91
Figure 4-14 – The Ni concentration versus Mn concentration measured on the negative electrodes from NMC622 cells.....	93
Figure 4-15 – The Co concentration versus Mn concentration measured on the negative electrodes from NMC532 cells.....	94
Figure 4-16 – The Co concentration versus Mn concentration measured on the negative electrodes from NMC622 cells.....	94
Figure 4-17 – Moles of gas versus calculated total moles of transition metals on NMC532 negative electrodes.....	96
Figure 4-18 – Moles of gas versus calculated total moles of transition metals on NMC622 negative electrodes.....	97
Figure 5-1 – UHPC cycling results for high and regular loading cells containing additives 2% FEC + 1% LiPO₂F₂.	108
Figure 5-2 – UHPC cycling results for high and regular loading cells containing additives 2% VC and 1 % DTD.....	110
Figure 5-3 – Long-term cycling results from high and regular loading cells containing additives 2% FEC + 1% LiPO₂F₂	112
Figure 5-4 – Long-term cycling results from high and regular loading cells containing additives 2% VC + 1% DTD.....	115
Figure 5-5 – Capacity at ~6000 h versus areal current density	116

Figure 5-6 – Examples of EIS spectra from high and regular loading cells.....	119
Figure A-1 – Post-cycling/storage results from NMC532 cells.....	142
Figure A-2 – Post-cycling/storage results from NMC622 cells.....	143
Figure A-3 – Example of voltage versus capacity curves (from dV/dQ analysis)....	144
Figure A-4 – Electrode and electrolyte results for NMC532 cells.....	145
Figure A-5 – Electrode and electrolyte results for NMC622 cells.....	146
Figure A-6 – Illustration of electrode capacities and alignment determined via dV/dQ analysis on NMC622 cells.....	147
Figure A-7 – Example of ¹⁹F-NMR spectra.....	148
Figure A-8 – FTIR measured from electrolyte sample.....	148
Figure A-9 – All results from DTA on NMC532 cells cycled at 40°C to 4.4 V.....	149
Figure A-10 – Mn concentration on the negative electrode versus gas produced in NMC532 cells.....	150
Figure A-11 – Mn measured on the negative electrode versus gas produced in NMC622 cells.....	150
Figure A-12 – The fraction of transesterification versus Mn concentration on the negative electrode of NMC532 cells.....	151
Figure A-13 – The fraction of transesterification versus Mn concentration on the negative electrode of NMC622 cells.....	151
Figure A-14 – Discharge capacity versus cycle number for high and regular loading cells at various upper cutoff potentials measured via UHPC.....	152
Figure A-15 – Gas production after 1200 h of cycling on UHPC.....	153
Figure A-16 – Extended cycling results for cells containing additives 2% FEC and 1% LiPO₂F₂.....	154
Figure A-17 – Photos of negative electrodes showing Li deposition removed from cells with high loading.....	155
Figure A-18 – Extended cycling results for high and regular loading cells with additives 2% VC and 1% DTD.....	156
Figure A-19 – Examples of gas produced cycled high and regular loading cells.....	157

ABSTRACT

Strategies to improve Li-ion cells involve decreasing cost, increasing lifetime, increasing energy density, and increasing safety. This thesis presents work from two studies aimed at extending cell lifetime and improving Li-ion cell energy density. The first study analyzes Li-ion cells throughout their lifetime to construct a timeline of performance, electrolyte composition, and electrode changes. The matrix included $\text{LiNi}_{0.5}\text{Mn}_{0.3}\text{Co}_{0.2}\text{O}_2$ (NMC532)/graphite and $\text{LiNi}_{0.6}\text{Mn}_{0.2}\text{Co}_{0.2}\text{O}_2$ (NMC622)/graphite pouch cells with excellent performing electrolyte mixtures, both cycling and storage protocols at 40 °C and 55 °C with both 4.3 V and 4.4 V upper cutoff potentials. This study found that under conservative conditions, minimal change to electrolyte and electrode compositions occurred. Many cell metrics and electrolyte transformations, such as fraction of transesterification, gas production, and transition metal dissolution, appeared to have a constant rate of change in this 12-month observation period. In most cases, results from cells after three to six months of testing could be used to reasonably estimate the status of the cells (electrolyte composition, gas production, etc.) at 12 months.

The second work presented considers the cycling and performance effects due to higher electrode loadings. The short and long-term cycling results showed capacity retention and parasitic reactions comparable to regular loading cells. While cells were limited to low charge and discharge rates, such work indicates increased stack energy density is achievable via increasing electrode loading with minimal cycle life penalty. Impacts of the work presented in this thesis shows, under some conditions, that minimal change to electrolyte is observed in long-term aged cells and that high electrode loadings can increase the stack energy density without penalty.

LIST OF ABBREVIATIONS AND SYMBOLS USED

μ XRF	Micro X-ray fluorescence spectroscopy
acac	Acetylacetonate anion
B_0	External magnetic field
C	Capacitance
C/x	Charge rate, x = hours for charge or discharge
CC	Constant current
CCCV	Constant current constant voltage
CE	Coulombic efficiency
CPE	Constant phase element
C-rate	Charge and discharge rate
DEC	Diethyl carbonate
DEOHC	Diethyl-2,5-dioxahexane carboxylate
DMC	Dimethyl carbonate
DMOHC	Dimethyl-2,5-dioxahexane carboxylate
DMSO	Dimethyl sulfoxide
DTA	Differential thermal analysis
DTD	Ethylene sulfite
dV/dQ	Differential voltage analysis
EC	Ethylene carbonate
EIS	Electrochemical impedance spectroscopy
EMC	Ethyl methyl carbonate
FEC	Fluoroethylene carbonate
FID	Free induction decay
FTIR	Fourier-transformed infra-red spectroscopy
GC-MS	Gas chromatograph couple to mass spectrometer
HFI	High frequency intercept
HPLC	High performance liquid chromatography
HRMS	High-resolution mass spectrometer
ICP-MS	Inductively coupled plasma mass spectrometry

LCO	Li_xCoO_2
LEDC	Lithium ethyl dicarbonate
LEMC	Lithium ethylene mono-carbonate
LFI	Low frequency intercept
LFP	LiFePO_4
LiMO_2	Lithium transition metal oxide
LMC	Lithium methyl carbonate
LMO	LiMn_2O_4
LNO	Li_xNiO_2
m	Magnetic moment
MA	Methyl acetate
MMDS	Methylene methane disulfonate
m_p	Mass positive electrode
m_{p0}	Initial mass of positive electrode
MS^2	Tandem mass spectrometry
N:P	Negative electrode capacity to positive electrode capacity ratio
NaCMC	Sodium carbon methylcellulose
NIST	National Institute of Standards and Technology
NMC111	$\text{Li}[\text{Ni}_{1/3}\text{Mn}_{1/3}\text{Co}_{1/3}]\text{O}_2$
NMC532	$\text{Li}[\text{Ni}_{0.5}\text{Mn}_{0.3}\text{Co}_{0.2}]\text{O}_2$
NMC622	$\text{Li}[\text{Ni}_{0.6}\text{Mn}_{0.2}\text{Co}_{0.2}]\text{O}_2$
NMC811	$\text{Li}[\text{Ni}_{0.8}\text{Mn}_{0.1}\text{Co}_{0.1}]\text{O}_2$
NMR	Nuclear magnetic resonance spectroscopy
OEMS	Online electrochemical mass spectroscopy
PVDF	Polyvinylidene
Q	Capacity
Q_0	Initial capacity
q-NMR	Quantitative nuclear magnetic resonance
Q_p	Absolute positive electrode slippage
Q_{SEI}	Li inventory loss
r^2	Coefficient of determination

R_{CT}	Contact resistance
R_s	Solution resistance
SBR	Styrene butadiene rubber
SEI	Solid electrolyte interphase
THF	Tetrahydrofuran
TTFP	Tris(2,2,2-trifluoroethyl) phosphate
UCP	Upper cutoff potential
UHPC	Ultra-high precision charger
V	Voltage
VC	Vinylene carbonate
W	Warburg element
XPS	X-ray photoelectron spectroscopy
XRD	X-ray diffraction
XRF	X-ray fluorescence spectroscopy
Z_{img}	Imaginary component of impedance
Z_{real}	Real component of impedance
α	Aligned with external field
β	Anti with external field
Δ_0	Initial full-cell slippage
Δ	Full-cell slippage
Δw	Change in weight
δ_n	negative electrode slippage
δ_{n0}	Initial negative electrode slippage
ΔV	Voltage polarization
ρ_w	Density (of water)

ACKNOWLEDGEMENTS

I would like to thank Natural Sciences and Engineering Research Council of Canada (NSERC), Nova Scotia Graduate Scholarship (NSGS) program, as well as Tesla Canada for partial funding of this work.

I would especially like to thank my supervisor, Dr. Jeff Dahn, for the invaluable research and learning experience here at Dalhousie University. I am very fortunate to have learned from him during the past few years and will continue to be inspired by his enduring enthusiasm, guidance, feedback, and encouragement.

I would like to thank my committee members, Dr. Heather Andreas, Dr. Peter Wentzell, Dr. Alex Speed, and Dr. Kevin Hewitt for their time, suggestions, and feedback throughout this program. I would also like to thank Lea Gawne for her continued guidance.

I am very grateful for the supporting and engaging members of the Dahn Lab as well as for the valued friendships I have made along the way. I especially would like to thank Michael Johnson and Jessie Harlow; their help has been essential to the success of these projects and so many others.

I would like to thank my family and friends, near and far, for their love, encouragement, support, chats, snacks, and dice games throughout this degree.

Finally, I thank Dylan and Beta for endless joy and love every day.

CHAPTER 1 – INTRODUCTION

Motivation

Clean energy storage is vital to large-scale integration of renewable energy sources. As countries and provinces commit to converting to renewable energy sources in the coming years, energy storage must be employed to counter the variability of renewable sources to meet consumer demands.^{1,2} Lithium-ion batteries, while currently used in many portable electronic devices, are also suited to complement the diverse, large-scale energy storage needs of applications such as electric vehicles, home energy storage, grid energy storage, peak-load shifting, and incorporation into microgrid systems.³⁻⁵ As the demand for this technology continues to increase from countries, provinces, utilities, companies, and individuals, so must production.⁶ This will likely involve not one type of Li-ion chemistry, but a suite of affordable, safe, and adaptable cells for various applications.

Globally, corporations are investing in the future of Li-ion technology and preparing for increased demand. Companies, such as Tesla, BYD, Volvo, and GM are committed to building fleets of electric vehicles, with rollouts scheduled within the next few years. Meanwhile, new companies such as Apple and Rivian are entering the electric vehicle market. Companies such as Tesla, Volkswagen, and GM are investing in large Li-ion factories, capable of producing annually approximately 430+, 240 and 70 GWh of cells per year, respectively.⁷⁻⁹ To reach these annual energy targets, Li-ion cells must be less expensive and have higher energy densities.

Still, battery production is in the early stages of transforming our energy landscape. For Li-ion batteries to continue to be incorporated on the global scale, their production and implementation must be economically and realistically viable. Cells must be safe, less expensive, have longer lifetimes, have higher density, and have higher charge rate capabilities.¹⁰⁻¹² Strategies to decrease the effective cost of Li-ion cells include increasing specific energy, increasing lifetime, and using less expensive materials. This document will present two studies aimed at extending lifetime, improving performance, and increasing cell energy density of Li-ion cells.

Overview of Li-ion Cells

Li-ion batteries are composed of individual electrochemical cells (shown in Figure 1-1) that shuttle Li-ions between electrodes during charge and discharge. During charge, Li-ions are transported to the negative electrode, and, during discharge, Li-ions are returned to the positive electrode. The positive electrode materials typically consist of a lithium transition metal oxide (LiMO_2) which stores Li in its layered or spinel structure. The general equation for the reaction at the positive electrode is shown in Equation 1-1. The negative electrode typically consists of graphite (although Si is an emerging negative electrode material) where Li from the positive electrode is intercalated between the sheets of graphene during charge and remain stored until discharge (see Equation 1-2). In addition to the positive and negative electrodes, Figure 1-1 also shows the current collectors for both electrodes, the ionically conductive electrolyte, the electrically insulating separator, and the electron and Li-ion pathways. A brief background about these components and more will be discussed below.

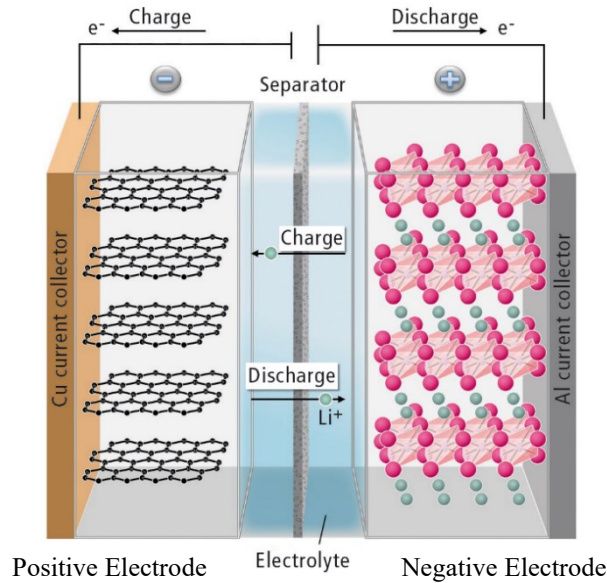
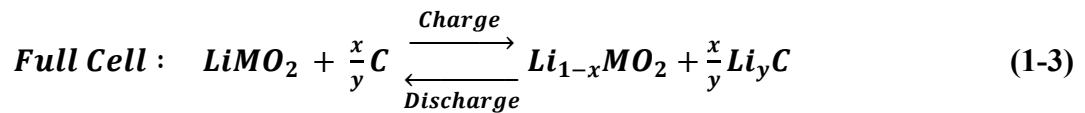
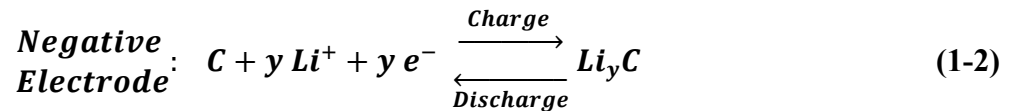
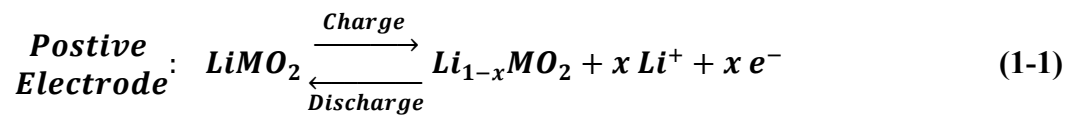


Figure 1-1 – Schematic of a Li-ion cell. Reproduced from Schultz et al.¹³



Positive Electrode

For Li-ion cells, it is desirable for positive electrode materials to be inexpensive, abundant, safe, and non-toxic, and to have high specific and volumetric capacities. It is also desirable for the materials to be stable at high potentials, high temperatures and during cycling.^{14,15}

In 1991, the first Li-ion cell was commercialized. This cell contained a Li_xCoO_2 (LCO) positive electrode and carbon negative electrode.¹⁴ LCO has a layered structure with high theoretical capacity ($\sim 270 \text{ mAh g}^{-1}$) and high energy density, however, can experience structural and thermal instability at increased temperatures, potentials, and charge rates.¹⁵

Other layered oxide materials in Li-ion cells such as Li_xNiO_2 (LNO), also have similar theoretical capacity ($\sim 270 \text{ mAh g}^{-1}$)¹⁶ but are less expensive and less toxic than LCO.¹⁵ This layered structure, however, is thermally unstable, which limits safety,¹⁷ and can undergo unwanted transformations, which result in Ni in the Li layer, or conversions to a non-layered, spinel structure.¹⁸ Additionally, their oxygen evolution at high potentials can accelerate cell degradation.¹⁹ A spinel material containing Mn, LiMn_2O_4 (LMO), is less expensive, but has a lower theoretical capacity ($\sim 150 \text{ mAh g}^{-1}$)¹⁶ as well as increased capacity fade at higher temperatures and reactivity causing Mn dissolution.^{14,15}

Other positive electrode materials use a mixture of these transition metals to achieve a higher specific capacity, stability at higher potentials, and increased safety. $\text{Li}[\text{Ni}_{1/3}\text{Mn}_{1/3}\text{Co}_{1/3}]\text{O}_2$ (NMC111) positive electrodes can achieve a high theoretical specific capacity ($\sim 280 \text{ mAh g}^{-1}$) and energy density, have good cycle life, and can be cycled to 4.6 V vs Li/Li^+ .^{15,16} Recently, sourcing concerns and the high cost of Co has motivated the industry to minimize the relative amount of Co in positive electrode materials.²⁰ This has led to materials such as $\text{Li}[\text{Ni}_{0.6}\text{Mn}_{0.2}\text{Co}_{0.2}]\text{O}_2$ (NMC622) and $\text{Li}[\text{Ni}_{0.5}\text{Mn}_{0.3}\text{Co}_{0.2}]\text{O}_2$ (NMC532) which show good cycling stability, increased safety, and good capacity. More recently $\text{Li}[\text{Ni}_{0.8}\text{Mn}_{0.1}\text{Co}_{0.1}]\text{O}_2$ (NMC811) and Co-free materials have also been investigated for Li-ion cells.²⁰⁻²² Additional positive electrode materials include phosphate-based LiFePO_4 (LFP) which has a very low cost, $\sim 170 \text{ mAh g}^{-1}$ theoretical specific capacity, excellent safety and thermal stability.^{14,16} LFP has a low operating potential and low density, which limits achievable energy density.¹⁵

Positive electrode materials used in this study are primarily NMC532 and NMC622. Both NMC materials have been studied extensively and shown, when combined with the right

electrolyte mixture, to yield Li-ion cells with long lifetime.²³ These materials are combined with small amounts (<5% total) of carbon black conductive material and binder to ensure good conductivity and contact with Al current collector, respectively.

Negative Electrode

Desirable negative electrode properties for Li-ion cells include high capacity, low capacity loss after the first cycle (low irreversible capacity), low volume expansion, low cost, and low active surface area.¹⁴ Graphene-based materials such as natural graphite and artificial(synthetic) graphite are common negative electrodes as they have high theoretical capacity ($\sim 370 \text{ mAh g}^{-1}$) and offer low operating potentials to increase overall battery voltage.²⁴ During the first charge and discharge cycle, a passivating film is formed from on the surface of the negative electrode called the solid electrolyte interphase (SEI). This formation causes irreversible capacity loss proportional to the electrochemically accessible specific surface area of the negative electrode.²⁵

Other materials used for negative electrodes include silicon-based materials. There is much motivation to incorporate Si materials for their high theoretical specific capacity ($\sim 3600 \text{ mAh g}^{-1}$),¹⁴ almost ten times that of carbon materials. Si, however, stores Li via forming an alloy, which incurs significant volume expansion (as much as 280%) during charge and subsequent mechanical failure.²⁶ Recently, SiO has been employed as a negative electrode material for its lower specific capacity ($\sim 1700 \text{ mAh g}^{-1}$) yet higher mechanical stability during cycling. Si-based materials could increase the energy density of the negative electrode to enable cells with higher energy density.²⁶ Like the positive electrode, negative electrode active materials must be combined with small amounts (<5% total) of conductive

carbon and binders to enable good electrical contact and adhesion onto the copper current collector.

Surface Coatings

Electrode materials often benefit from a protective surface coating. Some published surface coatings include Al_2O_3 , AlF_3 , TiO_2 and ZnO (Al_2O_3 -doped).^{15,16} Coatings can be added after electrode material synthesis via atomic layer deposition, sputtering, and wet chemistry methods.¹⁵ While this adds a small amount of inactive material to the mass of the cell, surface coatings can improve long-term cycling capacity, increase stability at high potentials, minimize transition metal dissolution, and minimize reactivity with electrolyte.¹⁴

Electrolyte

The electrolyte facilitates the transfer of Li-ions to and from the negative and positive electrodes. It is desirable for the electrolyte mixture to have a high ionic conductivity, be chemically stable in the operating potential window, be thermally stable, undergo minimal parasitic reactions, and improve cell safety and/or cycling performance.²⁷⁻²⁹ Electrolyte solvents for conventional Li-ions cells are typically liquid, carbonate-based compounds, such as ethyl methyl carbonate (EMC), dimethyl carbonate (DMC), and diethyl carbonate (DEC). These carbonates are safe and are mostly electrochemically and thermally stable within the operating potentials and temperatures of the Li-ion cell.^{14,30} A cyclic carbonate, such as ethylene carbonate (EC), is typically added to the solvent blend to increase the

ionic conductivity and can contribute to electrode passivation.²⁷ The salt component, typically lithium hexafluorophosphate (LiPF₆), imparts ionic conductivity to the solution. Depending on the mixture, salt and solvent concentrations are often adjusted to achieve maximum conductivity (around 1.2 m salt).^{14,31,32}

Changes to the electrolyte mixture are an especially cost-effective way to improve cell performance. For example, small amounts (< 5%) of additives are often employed to improve cell performance, extend lifetime, or improve safety.²⁸ In recent studies, co-solvents, such as methyl acetate (MA), have been incorporated to increase the ionic conductivity to enable faster charge and/or discharge.³³ The electrolyte is also responsible for passivating the negative and positive electrodes with the SEI during the first few charge and discharge cycles. This initial electrolyte reaction hinders further reactivity of electrolyte at electrodes thus extending cell lifetime.

Degradation Mechanisms

Much of Li-ion cell research focuses on the failure mechanisms of cells to inform material design and prescribe alternative chemistries/materials to prevent failure. Failure symptoms may include capacity, energy, and/or rate capability decrease over time. Sources of Li-ion cell degradation from active materials includes: SEI growth and decomposition, electrolyte decomposition, electrode particle cracking or structural disordering, transition metal dissolution, Li-plating, and/or graphite exfoliation.^{34,35} Inactive materials can also contribute to cell degradation via corrosion of current collectors, binder decomposition, and/or loss of electrical contact.³⁵

Improving Li-ion Cells

Considering the thousands of gigawatt hours of Li-ion cells projected to be produced each year, even small improvements to Li-ion cells can translate to better cells, lower costs, and more sustainable production. Such improvements could include using less expensive materials/reducing cost, increasing specific or volumetric energy density, improving lifetime, increasing rate capability, and improving safety.¹⁰⁻¹² In this work, results presented will include a long-term aged Li-ion cells study and a study of electrodes with increased energy density. To provide additional context, Chapter 2 will provide a brief introduction to Li-ion electrolyte degradation reactions as well as a literature review of recent, relevant advances in Li-ion battery electrolyte and electrode reactions. Chapter 3 will provide a description of the methods used in this work. Chapter 4 will present the results from the study of long-term aged Li-ion cells study with accompanying discussion. Chapter 5 will present results from a study of cells with increased electrode loading and increased energy density. Finally, Chapter 7 will summarize this work before describing future work related to this study and beyond.

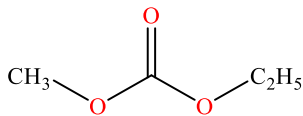
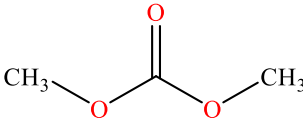
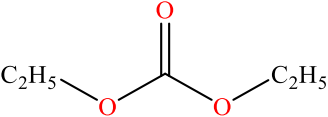
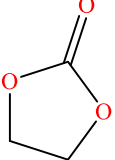
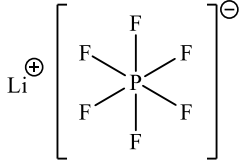
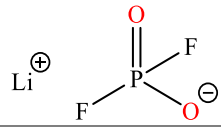
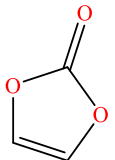
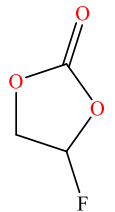
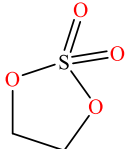
CHAPTER 2 – BACKGROUND

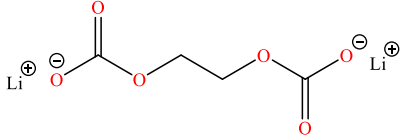
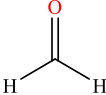
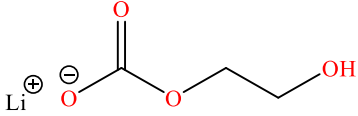
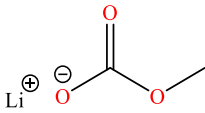
This chapter provides additional background on electrolyte reactions in Li-ion cells. First, common electrolyte components will be introduced, then a brief overview of reduction and oxidation reactions that occur in Li-ion cells will be presented. Reactions involving electrolyte salt and solid electrolyte interphase (SEI) will also be introduced. Finally, to complement the studies presented in this document, a review of recent, relevant work will be discussed. This includes recent findings involving chemical oxidation, electrolyte polymerization, and reactivity with the positive electrode.

Electrolyte Components

As introduced in Chapter 1, Li-ion electrolytes typically are composed of a salt dissolved in an organic, carbonate solvent. Common solvents and salts, along with their structures, are presented in Table 2.1. The solvent may be ~25-30% w/w ethylene carbonate (EC), to increase the overall conductivity of the solvent blend. The remaining portion of the solvent blend may be primarily dimethyl carbonate (DMC) or ethyl methyl carbonate (EMC), which are stable in the operating potential window of Li-ion electrodes that have been passivated. The primary salt used in Li-ion batteries is LiPF_6 . This salt has good thermal and chemical stability, low impurities,¹⁴ high conductivity in carbonate solvents, and minimal reactivity with the Al current collector.²⁷ Other salts may be included as an additive in small amounts such as lithium difluorophosphate, LiPO_2F_2 . Other additives common in electrolyte mixtures include vinylene carbonate (VC), fluoroethylene carbonate (FEC), and ethylene sulfate (DTD). VC has previously been shown to aid in negative

Table 2-1 – Common electrolyte components and reaction products listed with structure, abbreviation, and notes associated, when appropriate.

Structure	Name (Abbreviation)	Notes	Reference
<u>Solvents</u>			
	Ethyl methyl carbonate (EMC)	Low viscosity, good thermal stability window	14,30
	Dimethyl carbonate (DMC)	Low viscosity	30
	Diethyl carbonate (DEC)	Higher boiling point/Lower melting point	30
	Ethylene carbonate (EC)	Higher dielectric constant/conductivity	14,30
<u>Salts</u>			
	Lithium hexafluorophosphate (LiPF ₆)	Most common/ High thermal stability	14
	Lithium difluorophosphate (LiPO ₂ F ₂)	Improves lifetime/low solubility	14,36,37
<u>Additives</u>			
	Vinylene carbonate (VC)	Preferentially passivates electrodes	38
	Fluoroethylene carbonate (FEC)	Improves cycling performance/passivates electrodes	39
	Ethylene sulphate (DTD)	Improves cycling, decreases cell impedance	40

Pertinent Electrolyte Reaction Products (not provided in reaction mechanisms)		
	Lithium ethyl dicarbonate (LEDC)	41
	Formaldehyde	42
	Lithium ethylene mono-carbonate (LEMC)	41
	Lithium methyl carbonate (LMC)	41

electrode passivation via polymerization. FEC has been shown to extend cycle lifetime via improving the SEI and minimizing secondary electrolyte reactions.³⁹ DTD also extends lifetime and decreases gas production potentially by improving the negative electrode SEI.^{40,43–45}

SEI

The passivating SEI layer is an important feature of the Li-ion cell. Though some of the electrolyte and/or additives are consumed during initial SEI formation, the negative and positive electrode SEIs can hinder further electrolyte reactions while still conducting Li-ions from electrolyte into the active electrode particles. Many details of the negative electrode SEI are still unknown; however, it is expected that the layer contains lithium carbonate (Li_2CO_3), LiF, Li_2O , and Li-carbonates.⁴⁶ Some work has shown the layer becomes more inorganic with time.⁴⁷ SEI formation is the first of many reactions and secondary reactions that may change within the cell. If the SEI layer does not adequately

passivate the particles, continued electrolyte reactions could occur at particle surfaces. Alternatively, if the SEI layer increases cell resistance, this may hinder short and long-term cell performance. Film forming additives (such as VC) can form a more stable negative electrode SEI (presumably due to oligo(VC)) and improve cell lifetime.⁴⁶ Other work has identified some additives which may benefit the positive electrode SEI. For example, findings from Wu et al. (2018) indicates DTD can contribute to the positive electrode electrolyte interphase layer,⁴⁸ which could limit oxidation and potential gas production at the positive electrode surface.

Electrolyte Reactions Overview

Previous studies of Li-ion electrolyte have identified reduction pathways at the negative electrode which produce Li-carbonates, Li-alkoxides, CO₂, alkenes, and polymeric species²⁷ while oxidation pathways at the positive to produce CO₂ and CO have been proposed.⁴⁹ Some of these products can undergo secondary reactions and can even migrate to the opposite electrode to react further. The electrolyte solvent and salt have been shown to be sensitive to elevated temperatures and contaminants to produce polymeric species such as oligomers and oligo carbonates.⁵⁰ Additionally, some electrolyte components (such as EC) are prone to dimerization and polymerization, generating large, bulky molecules which can increase viscosity and therefore inhibit Li-ion transport.⁵¹

Electrolyte Reduction

Figure 2-1 and Figure 2-2 show examples of various reduction pathways of electrolyte species that have been proposed to occur at the negative electrode. These include the single

electron reduction of linear carbonates (Figure 2-1) ultimately forming Li-alkoxides, Li alkyl carbonates, CO, and/or esters.^{52,53} Cyclic carbonates will show preferential reduction versus linear carbonates, making them effective in SEI formation and preventing linear carbonate reaction. Figure 2-2 shows the reduction pathways for EC, a common cyclic carbonate in Li-ion cell, which can produce lithium ethyl dicarbonate (LEDC), C₂H₄, CO, and/or dilithium ethylene glycol.^{52,54} Other reduction species that may be present include the reduction products of additives. Some of these reduction reactions are summarized in Figure 2-3 and Figure 2-4. The reaction mechanisms include the double electron reduction of FEC producing fluoroethylene and Li₂CO₃ and/or LiF, CO₂, and a vinoxyl-radical.⁵⁵⁻⁵⁷ Another example is the double electron reduction of DTD to ultimately produce Li₂SO₄, C₂H₄, and/or C₄H₈O(OSO₂Li)₂.⁵⁸

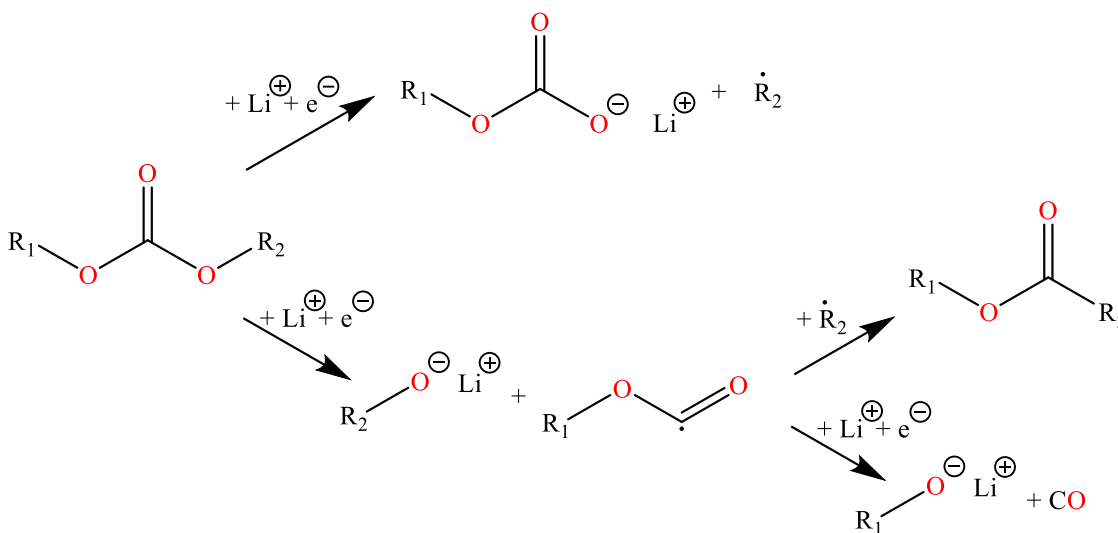


Figure 2-1 – Examples of reduction pathways for linear carbonate electrolytes proposed by Onuki et al. and Yoshida et al.^{52,53}

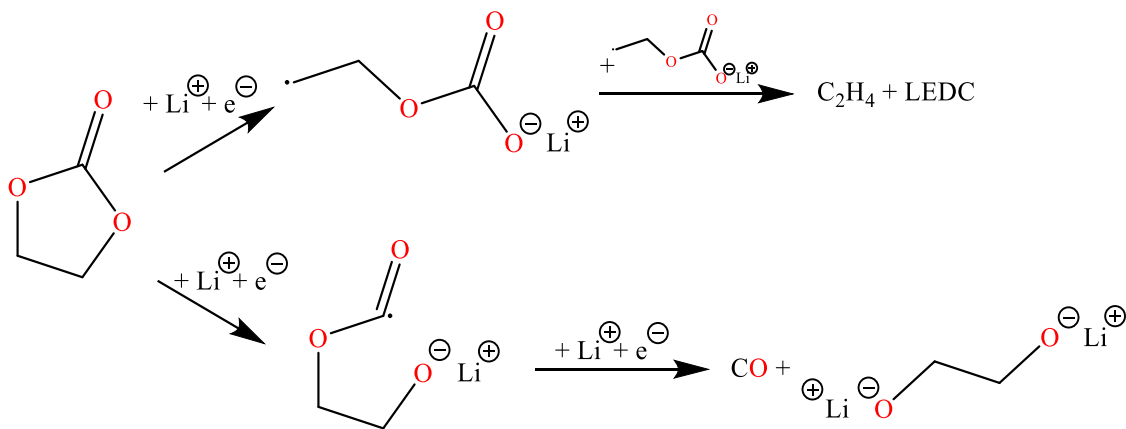


Figure 2-2 – Example of reduction pathways for cyclic carbonate, EC proposed by Onuki et al.⁵²

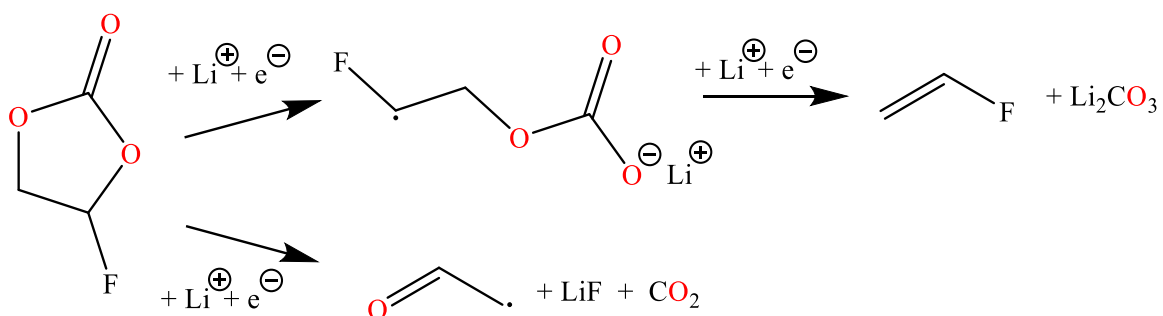


Figure 2-3 – Possible reduction pathways of FEC measured on Si or Si-C negative electrodes.⁵⁵⁻⁵⁷

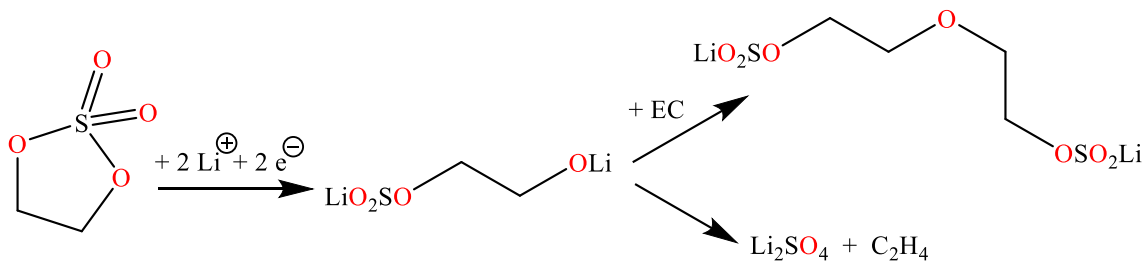


Figure 2-4 – Proposed reduction mechanism for DTD by Hall et al.⁵⁸

Electrolyte Oxidation

Figure 2-5 and Figure 2-6 show examples of electrolyte oxidation reactions. Figure 2-5 shows proposed oxidation pathways for EC which include the formation of CO, and an aldehyde radical⁵⁹ or the polymerization of multiple EC species, forming polyethylene carbonate.^{59,60} The ladder product may be the more probable of the two mechanisms involving loss of electrons and has been identified on positive electrodes.⁶⁰ Still, emerging research from Jung et al. has shown that electrolyte oxidation at NMC positive electrodes is likely due to chemical oxidation versus electrochemical oxidation at typical operating potentials (below 5.0 V vs Li/Li⁺).^{49,61} It was shown via online electrochemical mass spectrometry (OEMS), that EC oxidation products were preceded by oxygen release from the positive electrode and the rate of EC oxidation was dependent on the active surface area of the material. Figure 2-6 shows the proposed reaction involving O₂ and EC to produce H₂O, CO₂, and CO. Furthermore, Jung et al. justify the discrepancies of previously reported electrolyte oxidation potentials; as these discrepancies are now presumed to have originated from the positive electrodes oxygen release.^{49,61}

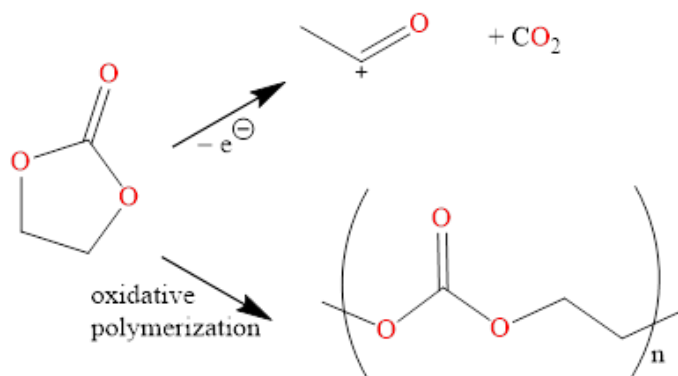


Figure 2-5 – Proposed oxidation reaction for EC, via loss of electron(s) from Xing et al. and polymerization reaction from Yang et al.^{59,60}

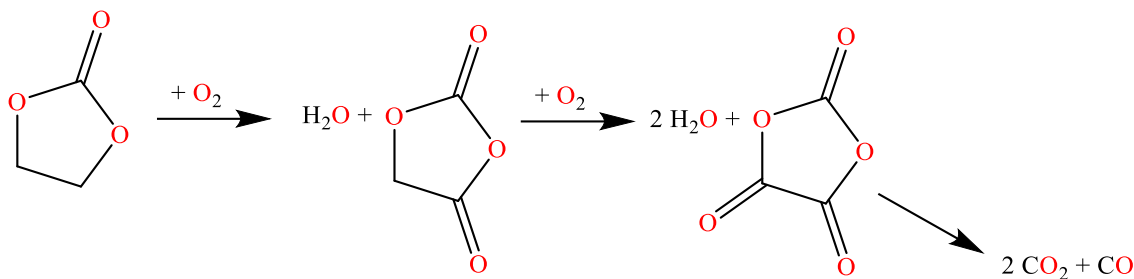


Figure 2-6 – Recent proposed mechanism for EC oxidation via reactive O₂ by Jung et al.^{49,61}

Work by Jung et al. has prompted additional investigation of electrolyte reactivity with lattice oxygen. This includes work from Rinkel et al. in 2020, who reported electrolyte reactivity at the positive electrode measured via ¹H and ¹⁹F – nuclear magnetic resonance (NMR) spectroscopy. Figure 2-7 shows the proposed reaction mechanism of O₂ and linear carbonate to form products such as lithium alkyl carbonates (cited as reaction intermediate), formic acid (RO₂H), H₂O, and CO₂.⁴² Rinkel et al. also suggest that some of these reaction products (CO₂ and formic acid) can transfer to the negative electrode, where they can reduce to form formaldehyde and Li₂O.⁴²

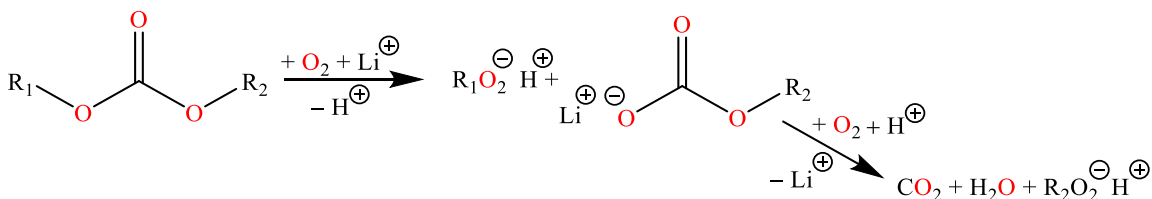


Figure 2-7 – Oxidation of linear carbonate via O₂ as proposed by Rinkel et al.⁴²

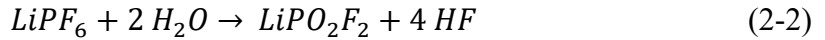
Polymerization

Previous studies investigating the composition of the SEI have suggested that EC, VC, and FEC undergo polymerization reactions to help form a stable, passivating SEI.^{28,62} Mechanisms for these polymerization reactions have included initiation steps such as cationic ring opening, reduction, and oxidation of EC and VC. It has been suggested that EC can polymerize to polyethylene carbonate (Figure 2-5)⁶⁰ and that VC can polymerize to poly(VC).^{63,64} FEC's reduction product, fluoroethylene, (Figure 2-3) has also been proposed to undergo polymerization on Si electrode surfaces to form polyvinyl fluoride and even polyene.^{29,57} Alternate mechanisms for possible FEC polymerization include the formation of LiF and VC, which then can polymerize,⁶² and the more complex formation of a cross-linked polymer observed on Si-C negative electrodes.⁵⁶ Recent studies involving cyclic carbonate polymerization/oligomerization mechanisms will be discussed further below.

Salt Reactivity

Equations 2-1, 2-2, and 2-3 show an example of proposed salt reactions that may be present in Li-ion cells. LiPF₆, though mostly stable, can breakdown into LiF and PF₅, especially at high temperatures (see Equation 2-1).^{65,66} Additionally, if excess water is present in solution LiPF₆ can react to form LiPO₂F₂ and hydrogen fluoride (HF) (see Equation 2-2).⁶⁷ The PO₂F₂⁻ anion is expected to improve cell performance, however, HF in Li-ion cells may be responsible for some transition metal dissolution at the positive electrode and/or reduction products at the negative electrode (H₂ and LiF) (see Equation 2-3).⁵⁷ Furthermore, it is possible that LiPF₆ can be removed from the electrolyte solution by

reacting with lithium carbonate (Li_2CO_3) in the SEI to form LiF , CO_2 , and LiPO_2F_2 or via the acid catalyzed reaction to form LiF , CO_2 and POF_3 .⁶⁸⁻⁷⁰



Crosstalk

Recent work has suggested that the electrolyte reaction products are not limited to a single electrode. Instead, reaction products can migrate to the opposite electrode and react further. In 2017, this crosstalk mechanism was investigated by Xiong et al., who compared electrodes, electrolyte, and gas production from pouch bags containing both separated, charged electrodes and full NMC532 cells to identify isolated and/or full cell reactions. The results indicated that oxidation products from the positive electrode, including CO_2 , could migrate to the negative electrode where they are reduced and can contribute to SEI formation and H_2 gas production.^{71,72}

Following this, additional work investigating crosstalk species identified the dissolution of Mn at the positive electrode and migration of Mn to the negative electrode. Here, it dominated the SEI composition, decreasing Li_2O and LiF content. The presence of Mn on the negative electrode was found to hinder SEI passivating properties, and instead allowed for electrolyte to be reduced at the negative electrode, in turn, contributing to cell

degradation.^{64,73} These crosstalk reactions highlight the complex, dynamic nature of Li-ion cells.

Recent Electrolyte Studies

Many papers, reviews, and proposed mechanisms in the Li-ion research field include LEDC (see Figure 2-2) as a major SEI component with high Li-ion and low electron conductivity.^{28,41} However, recent work by Wang et al. from the US Army Research Laboratory challenges LEDC's presence and suggests, rather, that lithium ethylene monocarbonate (LEMC) is the major SEI component.⁴¹ If LEMC is present rather than LEDC, it contradicts findings from major research labs, including previous reports from the US Army Research Laboratory. Wang et al. cite that the previous methods to synthesize LEDC synthesized LEMC and subsequently, characterization and chemical analysis for LEDC was LEMC. As SEI components, characteristics such as conductivity of Li-ions and chemical reactivity are important to the function and longevity of the SEI. After redesigning LEDC and LEMC synthesis, Wang et al. found that LEDC and lithium methyl carbonate (LMC) have low conductivities compared to LEMC.⁴¹

LEDC synthesis for standard analysis was previously performed in an ethereal solvent by reacting lithiation agents with ethylene glycol to produce di-lithium ethylene glycol.⁷⁴ This intermediate was then expected to react with CO₂ to produce LEDC. However, it was discovered that this intermediate was mostly insoluble in ethereal solvents, essentially limiting the reaction of di-lithium ethylene glycol with CO₂. Instead, Wang et al. suggest that the small amount of soluble intermediate and CO₂ undergo carbonate formation to

produce LEMC. Alternative and improved syntheses for both LEDC and LEMC were needed to confirm the identity of either product.

LEDC was instead synthesized in dimethyl sulfoxide (DMSO) solvent via deprotonation of LEMC and subsequent reaction with excess CO₂.⁴¹ This was shown via Fourier-transformed infra-red spectroscopy (FTIR), NMR, and elemental analysis to have formed LEDC·2DMSO. Under sonication with anhydrous tetrahydrofuran (THF), amorphous LEDC was formed and confirmed via X-ray diffraction (XRD) and NMR. It was found that this product is quite reactive. Equilibria studies in this report found LEDC to react readily with protons to form LEMC and to react with DMC to form LMC.

LEMC was synthesized via lithiation/deprotonation of ethylene glycol with n-butyllithium followed by reaction with excess CO₂.⁴¹ LMC was synthesized by the same reaction with methanol instead of ethylene glycol. Both products were insoluble from the reaction solution, and the structure confirmed via FTIR, NMR (solution and solid state), elemental analysis, XRD and X-ray photoelectron spectroscopy (XPS).⁴¹

Characterization via NMR of SEI (via DMSO-d₆ and D₂O extracts) showed evidence of LEMC and showed a small portion of LMC.⁴¹ Convinced that LEMC is the prominent SEI component, Wang et al. compared Li⁺ conductivity of the synthesized samples to show that LEMC had much higher conductivity, than LEDC and LMC, and that the conductivity of the negative electrode SEI matched that of LEMC. It is important to identify this prominent SEI component, both to establish its role in the passivating layer and to determine the mechanisms involved in its formation. A new reaction mechanism was proposed to suggest that LEMC in the SEI may be a derivative of LEDC or that EC can react with existing SEI/electrolyte to form LEMC.⁴¹

The results from this paper challenge the existing understanding of SEI formation. While additives such as VC can be preferentially reduced to limit EC reduction during initial SEI formation, EC reduction products may be present in long-term aged cells or once all VC is consumed. The previous results citing LEDC formation will need to be revisited and work is needed from additional research groups to recreate these findings. Finally, more work to identify the reaction mechanism producing LEMC and LMC in the SEI needs to be investigated.

Oligomerization of Electrolyte

Recent work by Henschel et al. (2019) from the Winter group at the University of Munster has attempted to expose some of the mechanisms in SEI formation and in electrolyte reactions via liquid chromatography.⁵⁰ Liquid chromatography, versus gas chromatography, allows less volatile electrolyte species to be identified. In this two-part report, high performance liquid chromatography (HPLC) coupled to a high-resolution mass spectrometer (HRMS) with tandem mass spectrometry (MS²) capabilities was used to identify the soluble oligomeric (and other polymeric) compounds.^{50,75}

Henschel et al found that exposure of electrolyte to thermal stress (elevated temperatures of 80 °C) caused formation of oligomeric carbonates, ethylene glycols, carbonate-ethylene glycols, and other structural isomers. The presence of oligomers with high ethylene glycol content were especially indicative of thermal stress.⁵⁰ Exposure of electrolyte to electrochemical stress (charge and discharge of cell) also produced oligomeric carbonates and ethylene glycol.⁷⁵ Additional products of solvent and salt reactivity were detected in electrolyte from charged and discharged cells such as phosphate carbonates. Electrolyte

analyzed after many charge and discharge cycles had phosphate carbonates with larger average mass than the electrolyte from cells after the initial formation charge and discharge. Ether carbonate co-oligomers were found in the same relative concentration in formation cells versus older cells.⁷⁵ The inclusion of the additive VC in electrochemically stressed electrolyte limited the total products identified. The differences were marked by a decrease in phosphate carbonates and increase in relative amounts of oligo phosphates.

Results of this study highlight a potential advantage of using the additive VC to prevent extensive electrolyte reactions after formation. Overall, these papers report over 300 unique compounds found in electrolytes,^{50,75,76} however, with VC, only a few were identified after formation.⁷⁵ After cycling, however, the control electrolyte showed fewer products than the electrolyte containing VC. Henschel et al. also noticed that the average mass of products increased from formation to post-cycled cells and proposed that the decrease in measured products could be due to continued elongation forming insoluble products.⁷⁵ These results are primarily based on National Institute of Standards and Technology (NIST) matching of identified species and are not quantified. While it is possible to estimate relative concentrations of each sample, these results would be strengthened by the inclusion of standards to confirm some of the prominent species and to quantify the degree to which these species are present in solution. This would help determine the degree of solvent loss in solution and confirm proposed mechanisms.

Work that followed by Henschel et al. from the Winter group in 2020⁷⁶ aimed to propose reaction mechanisms for these compounds via labeling carbons on EC with ¹³C. The increased mass on the EC's ethyl group was detectable via HRMS and MS². Again, thermal, and electrochemical stresses were applied to the electrolyte (either stored for

thermal degradation or used in cells for electrochemical stress).⁷⁶ Unlike the previous study, results from electrolyte with VC were not included, instead no additives were studied.

EC (via ^{13}C) was found to be the main component of oligo-carbonates and co-oligomers during thermal stress. Unlabeled linear carbonate derived alkyl groups were expected to terminate the elongation process of these chains. Co-oligomers were thought to originate from an additional de-carboxylation step. Glycols were also thought to be produced via further CO_2 removal. Under thermal stress, oligo(fluoro)phosphates, likely from solvent and salt reactivity, were found to have unlabeled carbonates and are estimated to originate from linear carbonates and salt versus EC and salt.⁷⁶

During electrochemical aging, however, oligo phosphates also show evidence of ^{13}C labeled, EC-originated ethyl groups. Phosphate carbonates showed evidence elongation via EC derived ethyl groups and evidence of termination via linear carbonate derived alkyl groups. Like thermal aging, co-oligomer and polycarbonate products in electrochemical aging indicated EC was the primary carbonate used in the initiation and elongation steps while linear carbonates were responsible for termination. This termination was proposed to originate from linear carbonate-derived alkoxide.⁷⁶ Considering LEMC formation proposed by Wang et al., Henschel et al. explored LEMC as a reactive species in solution and proposed a reaction mechanism to form phosphate carbonate oligomers.^{41,76}

Unlike previous studies, this work does not include additives in electrolyte blends studied. Since VC was previously shown to produce fewer oligomeric species after formation, less variety of products (and likely less EC reactivity) would be expected. Perhaps future work will explore differences upon additive addition; however, this study will need to be

designed carefully to differentiate carbons originating from EC, VC, or linear carbonate. It will also be important to quantify of the extent of polymeric formation and rate of solvent/salt consumption in cycled cells to determine electrolyte lifetime and temperature limitations. Quantifying oligomer formation and electrolyte consumption would help confirm reaction mechanisms and rates.

While Li-ion electrolyte research at Dalhousie does not yet include HPLC to measure larger, less volatile products, results from this study are important to consider as these products are likely still present. Additionally, many of the proposed mechanisms by Henschel et al. involve alkoxide in the terminating step. Increased presence of alkoxides in solution could limit elongation of oligomers, and therefore limit EC consumption, changes to electrolyte conductivity, and deposits of large, insoluble species on SEI. These alkoxides, a reduction product of linear carbonates, also catalyzed transesterification reactions between linear carbonates in solution (discussed further in Chapter 4).

Electrolyte and Electrode Reactions

Electrolyte reactions can also occur between the electrolyte and the electrode to cause transition metal dissolution. This phenomenon has been reported previously by many researchers, showing evidence of transition metals on the negative electrode.⁷⁷⁻⁸⁰ The extent of transition metal transfer from the positive electrode to the negative electrode is dependent on the extent of dissolution, migration, and deposition. Previous studies have found transition metal dissolution increases with increased upper cutoff potentials and increased temperature and is limited without salt in solution.⁸¹ Some also suspected HF, originating from salt decomposition (see Equation 2-2), to initiate transition metal

dissolution.⁸⁰ Many studies of transition metal dissolution or deposition cite major capacity fade and Li inventory loss associated with transition metal loss on the positive electrode,⁷⁸ while work from the Dahn laboratory showed that use of additives could minimize dissolution and/or deposition.⁷⁷

Recent work considering transition metal dissolution, migration, and deposition and electrolyte reactivity at the electrodes has also challenged some of the previously proposed mechanisms. Arguably the most comprehensive is Sahore et al.'s work measuring transition metal dissolution and solvation in the presence of charged and discharged electrodes. In this study, electrodes were exposed to electrolytes with exaggerated chemical properties to probe the effects on transition metal dissolution. These alterations involved the addition of water (to produce HF), removal of LiPF₆ (to remove solvated species), substitution of acetylacetonate Li salt (Li-acac) (to remove the effect of F⁻/HF), and addition of tris(2,2,2-trifluoroethyl) phosphate (TTFP) (to exaggerate effect of oxidatively unstable electrolytes).⁸²

Sahore et al. measured the transition metal content in electrolytes via inductively coupled plasma mass spectrometry (ICP-MS). The control electrolyte, containing solvent and salt, showed no measurable transition metal dissolution in uncharged positive electrode samples whereas showed Ni dissolution when charged positive electrodes were present. When no salt was included in the electrolyte mixture, no transition metal dissolution was measured for either charged or uncharged positive electrodes, indicating negative ions are needed to solvate transition metals and/or Li⁺ are needed to maintain charge balance. When HF was present in solution, there was no effect in the presence of charged positive electrodes, but there was a large increase in dissolution in the presence of uncharged positive electrodes.

Most of the transition metals measured in solution of the uncharged electrodes were Mn ions, indicating HF induced dissolution is present at low voltages.⁸²

Two alternative mechanisms were proposed by Sahore et al., who cited recent work by Jung et al. on the oxidation pathways of electrolyte at the electrode.⁴⁹ The first is described as electrochemical oxidation of the electrolyte where carbonates directly decompose, lose electrons, free protons, and form gasses (CO and CO₂) at the electrode. This would allow electrons to directly reduce transition metals. In the second mechanism, distinguished as chemical oxidation of the electrolyte, O₂ is released at the lattice (allowing electrons to reduce transition metals) and reacts with electrolyte to produce CO, CO₂, and H₂O.⁸² Jung et al. found that, for similar electrodes, chemical oxidation was the primary electrolyte oxidation route.⁴⁹ According to this mechanism and the expected reduction of transition metals (as electrons are not traveling through an external circuit) Sahore et al. expect cations (i.e. Li⁺) to be removed from solution to be incorporated into the positive electrode lattice to maintain charge balance.

The addition of Li-acac salt was used to further isolate transition metal dissolution from the potential presence of HF. It was also expected that transition metal-acac salts are more soluble in organic solutions than transition metal-PF₆ salts. The results showed no transition metal in electrolyte when exposed to uncharged electrodes and significant Mn and Co (no Ni) dissolution when exposed to charged electrodes. Sahore et al. present that the positive electrodes are more unstable (likely to release O₂) at the higher potentials, causing transition metal dissolution via chemical oxidation of the electrolyte. This effect was potentially amplified with the improved transition metal-acac formation in solution.⁸²

Solvent in this set up was also altered to include TTFP. TTFP is known to be oxidatively unstable, to oxidize at positive electrode, and to convert lattice O^{2-} to covalently bonded oxygen. This solvent showed no transition metal dissolution when exposed to uncharged positive electrodes, yet, showed elevated Ni dissolution in a charged electrode sample. This transition metal dissolution occurred without the presence of solvating anions or substituting cations in solution. This can be explained by the potential high solubility of transition metal-TTFP ligand and proton availability for replacement in the electrode.⁸²

It is possible that the lack of salt in the electrolyte containing only TTFP was limiting the extent of transition metal dissolution. To probe this while not introducing potential HF formation, Li-acac was added to electrolyte containing TTFP. These samples showed no transition metal dissolution in electrolyte exposed to uncharged electrodes and the highest dissolution (mostly Mn) in electrolyte exposed to charged electrodes. This larger, compounded effect highlights the extent of transition metal dissolution that is possible without HF but with chemical oxidation of the electrolyte and ions present.

These findings challenge the assumption that HF is to blame for transition metal dissolution. Instead, oxygen release at unstable electrodes could be the main transition metal reduction source for cycled cells and could cause significant chemical oxidation of the electrolyte at the positive electrode surface. While Sahore et al. present the various concentrations of Mn, Ni, and Co in solution, few conclusions are drawn regarding transition metal selectivity due to the unknown differences in transition metal-anion solvation. As a reader, however, some differences in transition metal dissolution stand out, such as the Mn-only dissolution in solutions containing HF at low potentials and the Ni-only dissolution present in solution where removal of O_2 was encouraged at high potentials.

This work is one that could be recreated by the Dahn lab to confirm these findings, to determine the extent of electrolyte oxidation, and to attempt to analyze negative electrode samples for transition metal deposition. More details will be described later in this document (see Chapter 6).

CHAPTER 3 – METHODS

Li-ion pouch cells used in this work can be easily mass-manufactured to ensure uniformity and can be supplied free from electrolyte. As such, they can be filled with various electrolyte mixtures to analyze the effect on cell performance and can be disassembled to study changes that occur within the cell. This chapter will present some cell specifications, details on cell formation and cycling protocols, outline post-cycling cell analysis methods referenced in subsequent chapters (also published in *J. of Electrochem. Soc.*, **168** (2), 020532 (2021)) as well as electrolyte analysis methods used in Chapter 4 of this document. The electrolyte analysis method was developed by the author and T. Taskovic. This work was published in *J. Electrochem. Soc.*, **168** (1), 010514 (2021).

Cell Specifications

402035-size (~240 mAh) Li-ion cells used in this study were manufactured by LiFun Technologies (Xinma Industry Zone, Golden Dragon Road, Tianyuan District, Zhuzhou City, Hunan Province, PRC, 412000). The cells consisted of a negative and positive electrode separated by a ceramic coated polyethylene separator and wound together to create the so-called “jellyroll”. The jellyroll was encapsulated by a laminated pouch bag. The positive electrodes in this work consist of either single crystal NMC532^{83,84} or polycrystalline NMC622 with a proprietary coating. NMC532 positive electrodes had 94 % active material, 2 % carbon back, 2 % KS-6, and 2 % polyvinylidene difluoride (PVDF) binder. NMC622 positive electrodes had 96 % active material, 2 % carbon back, and 2 % PVDF binder. Cells used in Chapter 4 have positive electrode loadings of 21.1 mg

cm⁻², while cells in Chapter 5 compare positive electrode loadings of 19.3 mg cm⁻² and 29.2 mg cm⁻² for regular and high loading cells, respectively.

The negative electrodes for both cells consist of artificial graphite 95.4 % (Kaijin, AML400), 1.3 % carbon black conducting material, 1.1 % sodium carbon methylcellulose (NaCMC) binder, and 2.2 % styrene butadiene rubber (SBR) binder. The relative loadings of negative electrode material for NMC532 and NMC622 cells used in Chapter 4 were 12.4 mg cm⁻² and 12.8 mg cm⁻² (both 1.55 g cm⁻³ density), respectively, to balance cells for 4.4 V potentials without Li deposition. The negative electrode active material loadings for cells used in Chapter 5 were 12.2 mg cm⁻² and 16.6 mg cm⁻² for regular and high loading cells, respectively, and were balanced with ~1.1 negative electrode capacity to positive electrode capacity (N:P ratio) for 4.3 V operation. These machine-made cells ensured uniform cell chemistries and minimized cell-to-cell variability, which could be seen in replicate cells that showed excellent performance agreement. The cells were received vacuum-sealed containing no electrolyte so various electrolyte mixtures could be added. Prior to filling with electrolyte, the gas bags of the cells were cut open and the cells were heated to (100 ± 1)°C under vacuum for 14 hours to remove residual moisture.

General Electrolyte Mixing

Various electrolyte mixtures were combined by mass in an Ar-filled glovebox and kept for 24 hours to ensure complete salt dissolution. Electrolyte solvents, additives, and salts included: EMC, DMC, EC, VC, DTD, FEC, methylene methanedisulfonate (MMDS), LiPF₆, and LiPO₂F₂. The names, suppliers and purities are reported in supplementary Table B-1 in Appendix B. In Chapter 4, electrolyte used for NMC532 cells in was 1.1 m LiPF₆

in EC:EMC (30% and 70% wt./wt.%, respectively) with the additives (in total weight percent) VC (2 %) and DTD (1 %) and the electrolyte used for NMC622 cells was 1.1 m LiPF₆ in EC:EMC (3:7 wt.%) with the additives (in total weight percent) VC (2 %), MMDS (1 %), and LiPO₂F₂ (0.5 %). These electrolytes were chosen for their demonstrated excellent performance with these cell chemistries.^{23,36,85,86} In Chapter 5, two different electrolyte blends were compared: 1.1 m LiPF₆ dissolved in EC:EMC:DMC (25 %, 5 %, and 70 % v./v.%, respectively) with additives VC (2 %) and DTD (1 %) and 1.1 m LiPF₆ in EC:EMC:DMC (25 %, 5 %, and 70 % v./v.%) with additives FEC (2 %) and LiPO₂F₂ (1 %).

General Cell Filling, Electrode Wetting, and Formation

Dried pouch cells were filled with approximately 1 g of mixed electrolyte and vacuum sealed (−90 kPa) with an MTI Corp. (Model MSK-115A) heat sealer at 165 °C. Soon after filling, cells with regular loading were held at a potential of 1.5 V for 24 hours to allow electrolyte to permeate the electrodes while preventing degradation of the copper current collector. Cells with high electrode loadings were held at 1.5 V potential for 48 h to fully permeate the thicker electrode coating. This longer wetting time was discovered in earlier cells when high loading with standard wetting time had irregular formations and cycling. After wetting, cells underwent their first formation charge and discharge cycle on a MACCOR series 4000 charger. During this formation cycle, cells were kept in a (40.0 ± 0.1) °C temperature box and cycled at a C/20 (11 mAh) charge and discharge current to the designated upper cutoff potential (UCP) (4.1 V – 4.4 V) before returning to the midpoint potential (3.8 V). Figure 3-1 shows an example of a 24 h wetting followed by a

formation cycle. The left axis (black line) shows the potential of the cell versus time and the right axis (red line) shows the current applied to the cell versus time.

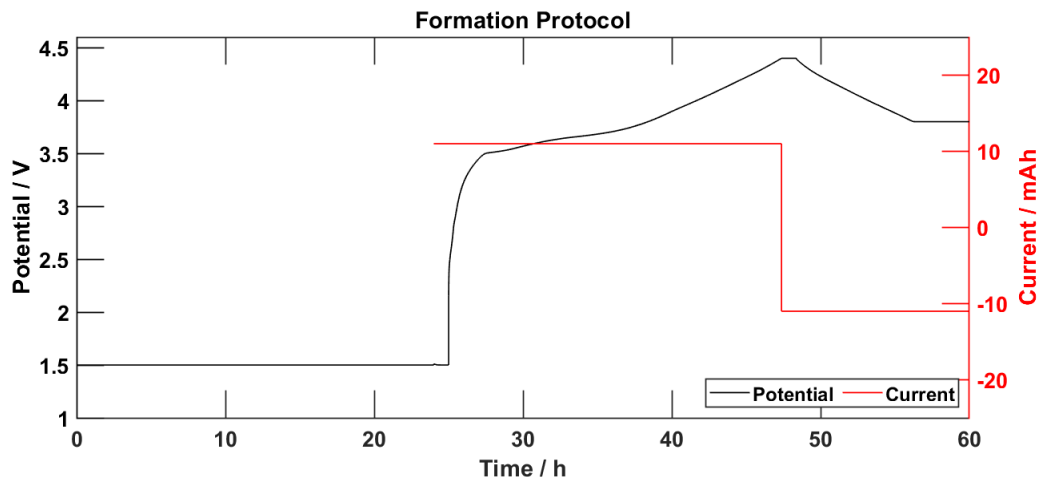


Figure 3-1 – Example of formation protocol. Left axis shows full cell potential versus time during cell wetting (0-24 h) and first charge and discharge. Right axis shows the current applied during the initial charge and discharge.

Gas Measurements

The amount of gas produced during the formation step was measured using Archimedes principle.⁸⁷ This measurement was taken by suspending cells from an analytical balance (AUW-D Series, Shimadzu, Japan) into room temperature de-ionized water (Thermo Scientific Barnstead Nanopure Water Purification System, 18.2 M Ω cm⁻²). The cells were then returned to an Ar-filled glove box, opened, and resealed (as described above) to remove formation gasses. The change in submerged weight before and after formation, and before and after cycling/testing is proportional to the volume of gas produced in the cell provided the gas bags of the pouch cells are not “firm” due to pressures in the cell greater

than 1 atm absolute. This occurs when total volume of gas in these 402035 cells is greater than about 3 mL.

Before cycling, cells were returned an Ar-filled glove box, opened, and re-vacuum-sealed to remove formation gases. The volume of gas produced before and after cycling was calculated using Archimedes principle.⁸⁷ Equation 3.1 shows the calculation to determine change in volume from the change in weight (Δm) measured divided by the density of water (ρ_w). Cells were suspended in de-ionized (Thermo Scientific Barnstead

$$\Delta Volume = \frac{\Delta m}{\rho_w} \quad (3.1)$$

Nanopure Water Purification System, 18.2 M Ω cm⁻²), room temperature water before and after the formation step and the weight recorded using an analytical balance (AUW-D Series, Shimadzu, Japan). The change in weight is proportional to the gas produced in the pouch bag. The amount of gas produced after long-term cycling was also measured.

EIS Measurements

The impedances of cells were measured using electrochemical impedance spectroscopy (EIS) after formation. EIS analysis uses an applied potential, at variable frequencies to measure impedance in a cell. The resulting spectra can be fit with equivalent circuit models to estimate the electron path resistance (R_e), solution resistance (R_s), charge transfer resistance (R_{CT}), SEI double layer capacitance (C), and diffusion within electrodes (via Warburg element, W) of a Li-ion cell.⁸⁸ Many equivalent circuits have been proposed for Li-ion cells,⁸⁹⁻⁹¹ some include the transmission line model to model the charge transfer resistance and double layer capacitance of multiple electrode particles in a cell.^{92,93} The

application of some of these advanced models is beyond the scope of this work. Here, a simplified model is employed. Figure 3-2 shows an example of an equivalent circuit used in some of this work. This simplified model uses a constant phase element (CPE), in place of a capacitor in parallel with R_{CT} , both in series with R_S and W . A CPE can aid in simplifying the modeling and analysis of EIS spectra by accounting for electrode particle inhomogeneities which would otherwise require a more advanced model to fit. Figure 3-3 shows an example Nyquist plot comparing the model using a capacitor (perfect semi-circle) and the updated model using a CPE (depressed semi-circle). The model using CPE more accurately fits actual Li-ion EIS spectra. A similar model is used to fit EIS spectra from cells in Chapter 4 and Chapter 5. First, cells were cooled to $(10.0 \pm 0.1) ^\circ\text{C}$ to increase spectral differences.⁹⁴ A BioLogic VMP3 potentiostat collected an alternating current impedance spectrum while applying a 10 mV amplitude AC potential signal, at variable frequencies (10 mHz – 100 kHz). The resulting Nyquist plot was then analyzed with the equivalent circuit below to extract the high frequency intercept (HFI), corresponding to solution resistance and intra particle electron path resistance, and the diameter of the semi-circle corresponding to the charge transfer resistance.^{92,93} Charge transfer resistance as used in this thesis includes desolvation and ion transport through the SEI layers.⁹⁵ In most measurements reported here, the feature in the EIS spectra from the contact resistances overlapped the charge transfer resistance and was included in R_{ct} . EIS measurements were repeated at the end of cycling and storage.

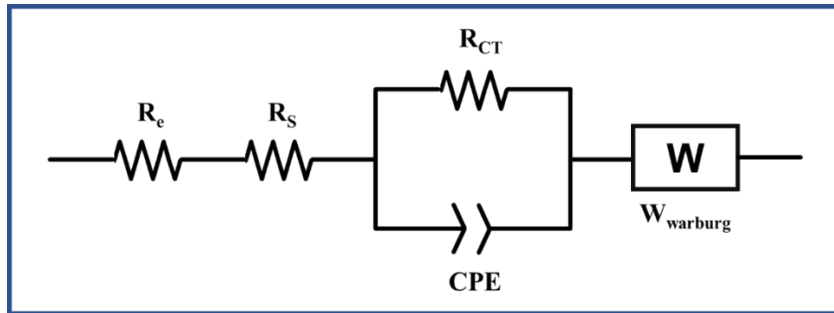


Figure 3-2 – Example of equivalent circuit used for EIS fitting. Includes R_{CT} in parallel with CPE, in series with R_e , R_s , and W element.

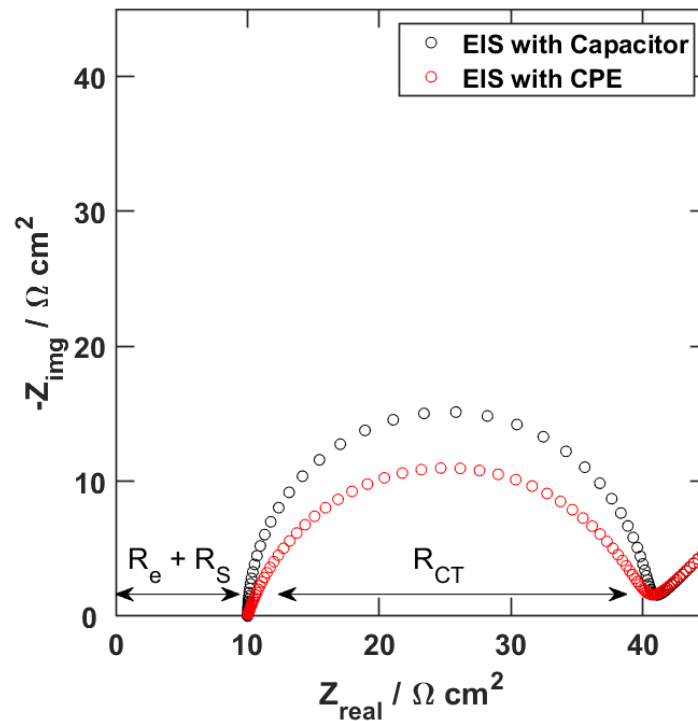


Figure 3-3 – Example EIS spectra for cell displaying effect of using CPE (with exponent = 0.8, for example) versus capacitor in equivalent circuit.

General Cell Cycling

Cells in this study were cycled anywhere from approximately 100 – 2000 cycles at various temperatures (20 °C, 40 °C, or 55 °C) on Neware (Shenzhen, China) battery charging systems. Cells were cycled from 3.0 V to their designated upper cutoff potential at various

charge rates using a constant current – constant voltage (CCCV) protocol for 50 charge and discharge cycles. After every 50 cycles, a C/20 discharge, charge, and discharge was applied to obtain the low-rate capacity before returning to the higher rate charge and discharging. Figure 3-4 shows an example of the current applied (right axis, red) and cell potential (left axis, black) versus time in this cycling protocol. The protocol was repeated as many times as required in the window of study. Charge rates for cells in Chapter 4 and Chapter 5 vary and will be addressed in the respective chapters. Voltage polarization (ΔV), proportional to internal resistance in Li-ion cells, was calculated from cycling data. The voltage polarization is equal to the average charge minus the average discharge voltage. The average charge and discharge voltages were determined by integrating the voltage versus capacity profile with respect to capacity and dividing by the total capacity for each cycle. After cycling, gas production, and EIS were re-measured for each cell.

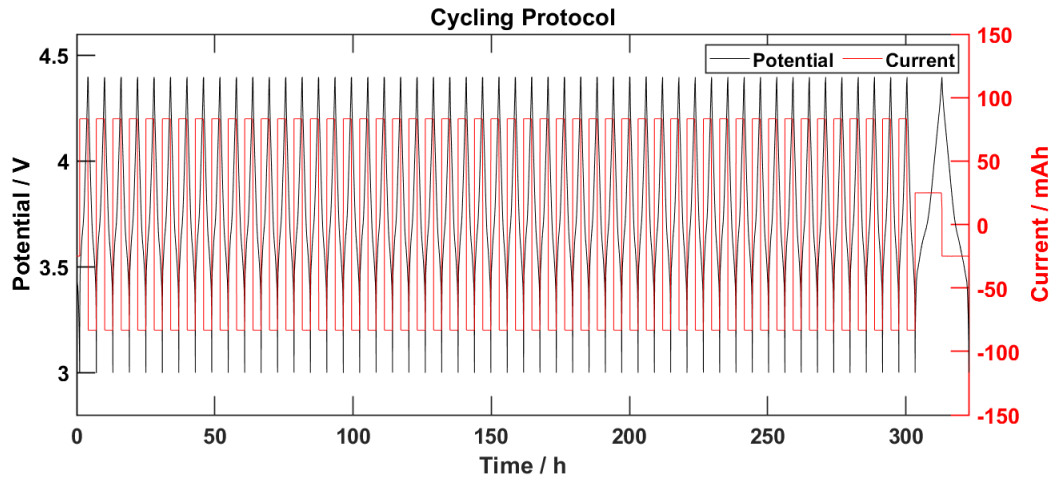


Figure 3-4 – Example of cycling protocol. Left axis shows potential versus time for first 50 cycles at C/3 charge and discharge rate followed by full charge and discharge at C/20. The right axis (red) shows the current versus time for the same cell.

General Cell Storage

Some cells in Chapter 4 also underwent high voltage storage testing on an in-house system.⁹⁶ Under this protocol, cells were stored at either 40 °C or 55 °C, charged to their designated upper cutoff potentials, then the open circuit potential drop was monitored periodically for one month before cells were recharged to their upper cutoff potentials and stored again. Drop in open circuit potential has been shown to originate from electrolyte oxidation at the positive electrode and shuttle reactions between the positive and negative electrodes.⁹⁶ When cells reached the end of their testing period, gas production, and EIS were re-measured for each cell. The author thanks J. Harlow (Dahn Laboratory, Dalhousie University) for running the storage experiments.

UHPC Cell Cycling

Some selected cells underwent cycling on the Ultra High Precision Charger (UHPC) developed at Dalhousie University.⁹⁷ Measurements on the UHPC allow small differences in capacity retention and parasitic reaction rates to be identified in a short period of time.^{97–}
¹⁰⁰ On the UHPC, cells were cycled at $C/20$ at constant current (CC) from 3.0 V to various upper cutoff potentials. Highly accurate and precise data from the UHPC allows differences in coulombic efficiency (CE), charge end point capacity, discharge capacity, and voltage polarization to be evaluated between cells sooner than would be distinguishable on a less precise system. Additionally, CE and charge end point capacity provide information on parasitic reactions rates present in cell and at the positive electrode, respectively.^{99,100} Minimizing these undesirable electrolyte reactions help identify more stable Li-ion chemistries for long term cycling.

UHPC Differential Voltage Analysis

The UHPC was also used to collect accurate and precise potential versus capacity curves before and after long-term cycling to evaluate cells' state of health. The derivative of this full cell data with respect to capacity was then calculated. This data can be fit with software, developed in-house,¹⁰¹ to fit the potential versus capacity profile of the full cell and to subsequently calculate potential versus capacity profile of both the positive and negative electrodes.¹⁰²⁻¹⁰⁴ Previous methods to obtain the respective voltage versus capacity curves would require the use of a reference electrode or disassembling cells after cycling to build coin cells with a single electrode (half-cells). However, incorporating reference electrodes was not practical due to the mass-produced nature of the cells in this study. Also, some of the inherent requirements of incorporating a reference electrode (consistent geometric and electric path)¹⁰⁵⁻¹⁰⁷ are difficult to achieve in the pouch cell design. Since cells studied in this work were destined for electrolyte analysis, construction of half-cells was also not desirable as they would require destroying the cell. Differential voltage analysis (dV/dQ versus Q, or dV/dQ) is a nondestructive, proven technique which allows for potential versus capacity profiles to be measured and calculated. Figure 3-5 shows an example of the potential versus capacity profiles derived from the dV/dQ analysis. Full cell and positive electrode potential are shown in black and blue, respectively, on the left axis and negative electrode potential is shown in red on the right axis. Figure 3-5 shows the positive and negative electrode potentials versus Li/Li⁺, whereas the full cell potential given as the potential of the positive electrode minus the potential of the negative electrode. In this thesis, all potentials (when referring to full cells or upper cutoff potentials) express the full cell potential unless otherwise stated.

Voltage versus capacity profiles can provide much information about the state of health of a Li-ion cell. By comparing profiles before and after cycling, it is possible to visualize and quantify the degree of Li-inventory loss, capacity loss from the negative electrode, capacity loss from the positive electrode and, relative electrode slippage. Li-inventory loss can be due to SEI building at the negative electrode or, in extreme cases, Li-plating.^{98,108} Relative electrode slippage occurs as cells age due to the change in relative capacity of both negative and positive electrode.⁹⁸ Voltage versus capacity profiles also allows the user to calculate active masses of either electrode before and after cycling.¹⁰¹

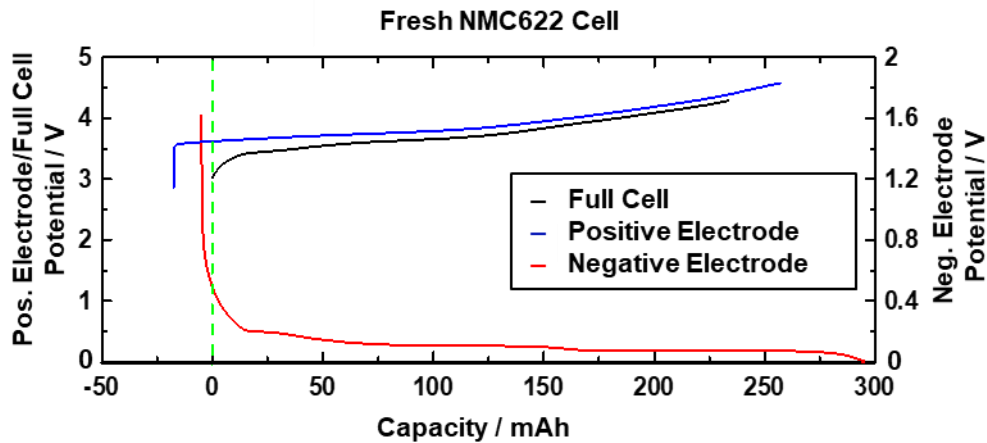


Figure 3-5 – Example of potential versus capacity curves extracted from dV/dQ analysis from UHPC data. The left axis shows the full cell potential (black) and positive electrode potential (blue) shown versus capacity. The right axis shows the negative electrode potential versus capacity.

For work presented in Chapter 4, several fresh cells of both NMC532/graphite and NMC622/graphite were also tested to obtain initial values of negative electrode mass, positive electrode mass and relative electrode slippage. All cells studied in Chapter 4 were then measured after cycling (or storage) using the UHPC at Dalhousie.⁹⁷ The dV/dQ versus

Q analysis was performed using software developed by Dahn et al.¹⁰¹ The difference between the values for the tested and fresh cells were used to calculate the change in relative electrode slippage, the Li inventory loss, the positive electrode mass loss and the negative electrode mass loss. Li inventory loss was calculated by summing relative slippage change after cycling/storage with positive electrode capacity loss.¹⁰⁸ Additional context and details of this calculation are discussed in Chapter 4. The author thanks J. Harlow and S. Cheng for fitting dV/dQ data.

DTA

Differential Thermal Analysis (DTA) is a non-destructive method of probing the state of an electrolyte inside a cell. This method, first developed by Day et al., involves cooling the cell down to a low setpoint, where the electrolyte will be frozen, and tracking the temperature of the cell as it heats back to ambient conditions at a constant rate.¹⁰⁹ In this case, the lower setpoint was -100 °C, while the upper setpoint was 25 °C. This range includes the entire freezing curve of 3:7 EC:EMC, and is within the liquid range of the reference cell, in this case, 1.0 M LiPF₆ in methyl acetate. In all cases, the cells were heated at a rate of 1.0 °C min⁻¹, cooled at a rate of 3.0 °C min⁻¹, and held at the lower setpoint for ten minutes, to allow for equilibration of cell temperature after cooling. The difference between the temperatures of the reference and sample cells can be used to identify temperatures and extents of phase transitions, which are dependent on the state of the electrolyte. Of note is the liquidus temperature, the highest temperature phase change that the electrolyte undergoes, which is particularly affected by the salt concentration and EC content of the electrolyte. In these cells, it was around -20 °C. The solidus feature, the

lowest temperature phase transition, is less affected by salt and EC contents, and is more dependent on the EMC content and the presence of other compounds created through transesterification. Cells were tested twice, once to obtain the initial signal, and once to remove an exothermic peak that appears in the heating curve at \sim -90 °C. This peak was removed by heating the cell to a temperature past that peak, cooling down to the lower setpoint, and then heating back through the entire heating range as normal. The author thanks M. Bauer (Dahn Laboratory) for making DTA measurements.

Electrolyte Sample Preparation for Analysis After Cycling or Storage

Measuring electrolyte compositional changes has become a critical area for Li-ion cell study as it can provide insight into cell failure and chemical degradation reactions occurring within the cell. Since electrolytes are designed (down to levels of 0.5% in composition) to achieve maximum conductivity, safety, and stability, even small changes to salt or solvent concentration can cause an increase or a decrease in cell performance. Tracking electrolyte composition also provides insight into the aging mechanisms occurring within cells. For example, as will be discussed in subsequent sections, presence of transesterification products indicates a linear carbonate has been reduced.

For safety, cells were discharged to 2.5 V before being transferred to an Ar-filled glove box. Under this inert atmosphere, a small opening was made in the corner of the pouch bag. About \sim 0.6 g of acetonitrile (Sigma, HPLC grade) was added via pipette and the jelly roll was agitated by hand to improve distribution of acetonitrile. Although acetonitrile has been shown to react with Li metal,¹¹⁰ Li deposition was unlikely to be present in the cells

of Chapter 4 considering their electrolyte composition, charge rates, and testing time/temperature. The bag was resealed with atactic polypropylene using a (Mastercraft, Canadian Tire, Canada) dual-temperature glue gun and allowed to mix for one day. The mass of the sealed bag was measured before and after mixing to ensure no significant mass loss. The next day, the extract was removed from the perimeter of the jelly roll via 1-mL syringe. Care was taken to remove as much solution as possible (~0.7-0.8 g). The solution was added to a (10.0 ± 0.1) mL volumetric flask containing acetonitrile, ~0.6 g of acetonitrile-d₃ (Sigma, >99.8%), and ~0.25 g of internal standard. 1,4-bis(trifluoromethyl)benzene (Sigma, >98%), then diluted with additional acetonitrile to the final volume. The solution was mixed and ~0.75 mL of solution was transferred to a sample tube with a gas tight cap (Wilmad). A more detailed description of sampling procedure is available in Reference 40.

NMR Principles

Nuclear magnetic resonance (NMR) spectroscopy uses a magnetic field and radio waves to observe nuclei within a sample. Because some nuclei have a net spin number, they can generate a magnetic moment (m). Magnetic moments normally take a random orientation, however, when an external magnetic field, B_0 , is applied, magnetic moments will align with the field.¹¹¹ Figure 3-6 shows the spinning nucleus “wobbling”, or precessing (blue arrow), about the magnetic moment (m) in the applied magnetic field (B_0 , grey arrow).¹¹² The frequency of the precession is equal to the Larmor frequency and is proportional to the magnetic field strength. Figure 3-7 shows the orientation these magnetic moments can take. Panel (a.) shows magnetic moments in random orientation when no applied field is

present; panel (b.) shows the alignment of magnetic moments that occurs when an external field is applied. Magnetic moments can either be oriented with (α) or against (β) the applied field. Figure 3-7c. shows the magnetic moments rotation when a pulse of radio frequency radiation is applied. To stimulate nuclei in this field, a radio frequency pulse is applied cause nuclei to rotate 90°. As in Figure 3-7d., Once the stimulus is removed, nuclei return to the beginning, lower energy states. The net signal is collected by a receiver coil, generating the free inductive decay (FID) spectrum.^{111,112}

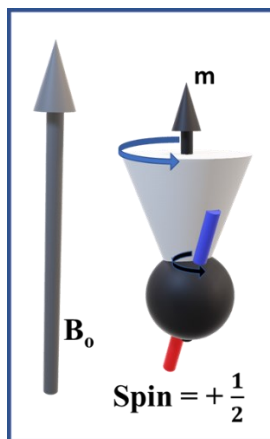


Figure 3-6 – Schematic showing spin of an unpaired particle (black arrow), the precessing motion (blue arrow), the net magnetic moment (m) and the orientation in applied magnetic field (B_0).

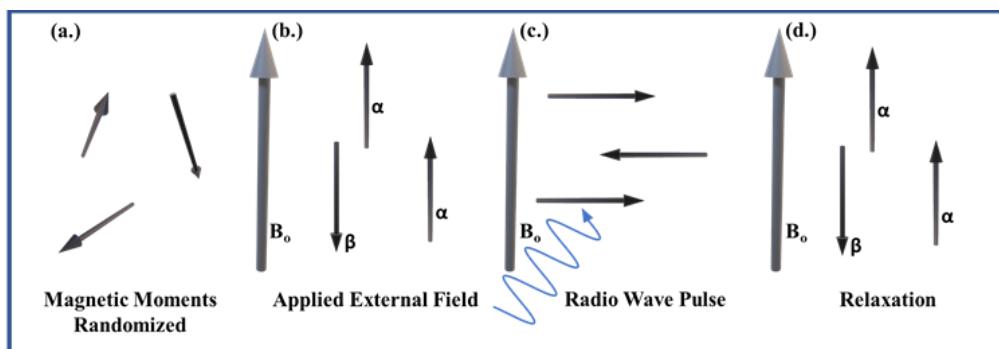


Figure 3-7 – Schematic of magnetic moment orientation when no field is applied (a.) a external field (B_0) is applied (b.), a 90° radio wave pulse is applied (c.), and the return to alignment after pulse is applied.

These signals are also sensitive to neighboring electrons, which interfere with, or shield, the applied magnetic field. A nucleus surrounded by higher electron density will feel a slightly lower field strength and as a result will have a lower frequency.¹¹² Fourier transformations of the FID can resolve individual protons to generate a typical NMR spectrum. Figure 3-8 provides an example of a Fourier transformed ¹H-NMR spectrum where the amplitude is plotted versus frequency (commonly in units of ppm). In this spectrum, shielded protons appear on the right, and protons that are deshielded (perhaps surrounded by electron withdrawing species) are shifted “downfield” to the left.¹¹¹

NMR is a powerful tool for identifying compounds based on their chemical shift and magnitude. For Li-ion electrolytes, NMR also can not only measure the organic components (carbonates, additives) of an electrolyte via ¹H-NMR spectra and ¹³C-NMR spectra, but can also measure the inorganic, salt species (LiPF₆, LiPO₂F₂) via ¹⁹F-NMR spectra present in the same sample. Since NMR peak areas are theoretically proportional to the number of nuclei in the sample, it is possible to use NMR quantitatively. This, however, requires careful evaluation of the acquisition program to ensure, for example, that adequate relaxation times (relaxation delays) are used and that spins are at steady state (via dummy scans), for the sample matrix. To achieve accurate quantification of organic and salt species present in electrolyte samples, acquisition parameters were carefully designed with the help of Dr. Mike Lumsden (Dalhousie Chemistry Department), to ensure quality quantitative spectra.

NMR Specifications

A small allotment of the prepared electrolyte sample underwent NMR analysis. Quantitative ^{19}F and ^1H -NMR measurements were conducted using a Bruker Avance 300 or 500 MHz spectrometer. The internal standard (1,4-bis(trifluoromethyl)benzene, Sigma, USA, 98% purity) allowed for quantification of PF_6^- , EC, and linear carbonates. ^{19}F -NMR acquisition consisted of 32 scans (0 dummy scans) with a 10 second relaxation delay and ^1H -NMR acquisition consisted of 16 scans (2 dummy scans) with an 80 second relaxation delay. Since some of the smaller, additive components and linear carbonate ratios are difficult to determine from the NMR spectra, additional characterization of the electrolyte was needed.

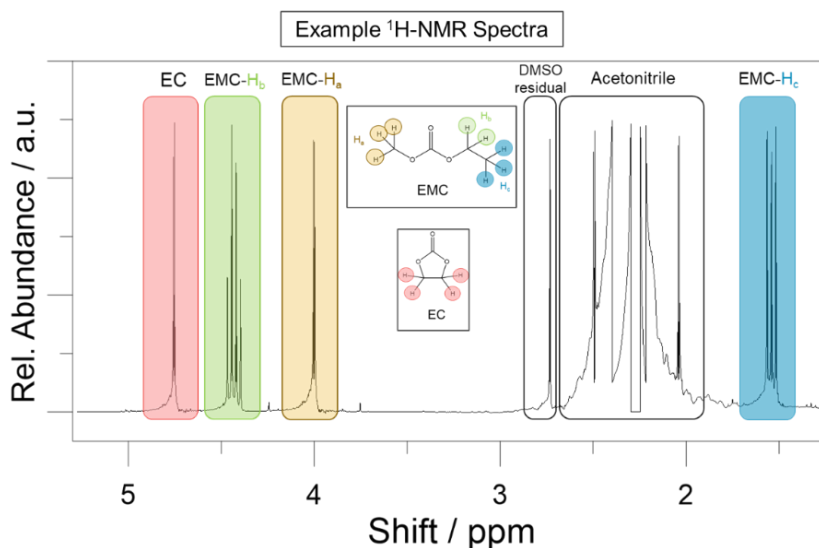


Figure 3-8 – Example ^1H -NMR spectra of linear carbonate EMC and cyclic carbonate EC (measured on a 300 MHz NMR instrument). Highlighted peaks include EC peaks in red, methyl groups from EMC in green and ethyl groups from EMC in yellow and blue.

GC-MS Principles

A gas chromatograph coupled to a mass spectrometer (GC-MS) combines the separation capabilities of chromatography with the identification and quantification capabilities of mass spectrometry. This instrument is ideal for separating and quantifying volatile organic species. Since primary electrolyte compounds meet this criteria, GC-MS is an excellent and sensitive tool for electrolyte analysis. Figure 3-9 provides a schematic of the major GC and MS components. During a liquid analysis, diluted samples are injected into the injection port, which is kept at high temperature to fully volatilize the sample.¹¹³ From here, a carrier gas (mobile phase), typically He or H₂, carries the gas sample from the port and onto the column. GC capillary columns are long (~30+ m) hollow tubes which are coated on the inside with a stationary phase (blue lining in Figure 3-9). The coating can be polar, non-polar or slightly polar, depending on the application.¹¹³ The retention time of any given species is dependent on the length of the column, average linear velocity, the stationary to mobile phase volume ratio, and the distribution constant between analyte in stationary phase and mobile phase. For the same GC column, species with varying distribution constants will separate. Those with more affinity for the stationary phase will have a longer retention time and those with less relative affinity for stationary phase will have a shorter retention time.^{113,114} The temperature of the column is also typically ramped up to decrease the retention time of more strongly retained species.¹¹³

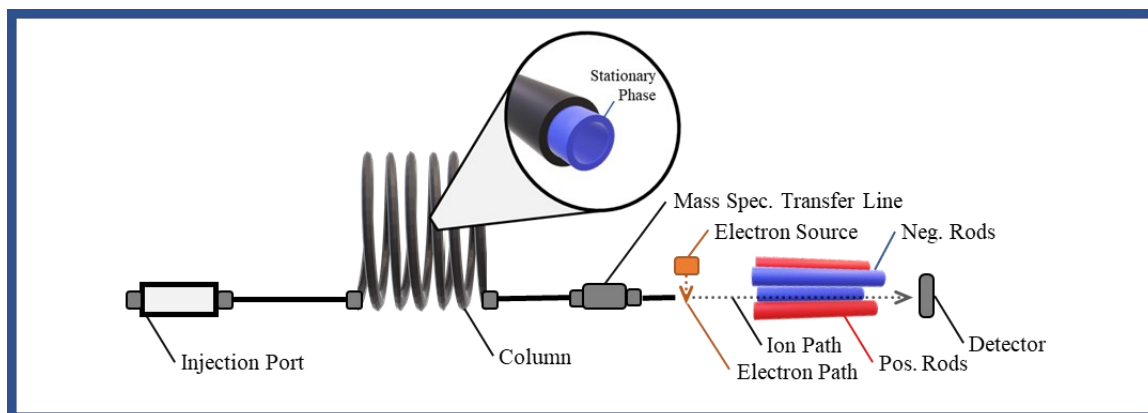


Figure 3-9 – Schematic of a GC coupled to a MS. Diagrams path of sample from injection port to the detector.

To identify and quantify the separated compounds, a MS is used. Mass spectrometers allow charged species to be separated and detected. First the compounds exiting the column are ionized. Most commonly an electron source is used, which bombards the sample with electrons to eject an electron from the compound. This can create an intact but charged molecular ions and/or smaller fragment ions (typically both with +1 charge). The ions then travel through the mass quadrupole to be separated. The quadrupole acts as a mass filter by altering the potential and variable frequency applied to oppositely charged rods. When the attractive force and repulsive force from the negatively charged and positively charged rods, respectively, are not sufficient to interfere with the cation's path through the quadrupole, the cation will successfully travel the length of the quadrupole and reach the detector. Target mass to charge ratios (m/z) can be selected by varying the applied voltages.^{113,115} The ions and ion fragments generated are characteristic of each compound and can be considered “fingerprints” of these species. These can be identified qualitatively

using a library of MS spectra (NIST), but a calibration solution is needed in GC-MS spectra to reliably quantify species.

GC-MS Sample Preparation

About 3 mL of remaining prepared electrolyte extract for the NMR was reserved for GC-MS analysis. First, the 3 mL solution was combined with ~0.2 mL of ~3 M ammonium sulfate solution. The addition of a highly concentrated salt solution allows for the removal of polar salt species (that may damage GC-MS) into a polar, aqueous layer.^{40,116} Solutions of analytes used in calibration underwent this salt extraction procedure to confirm relative concentrations were not affected. After mixing vigorously for 30 seconds, the aqueous and organic layers were centrifuged to ensure separation. A few drops of the organic layer were further diluted into 1.5 mL of acetonitrile before being measured with GC-MS.

GC-MS specifications

An Agilent autosampler injected 1.5 μL of sample onto a split inlet (260 $^{\circ}\text{C}$, split ratio 100:1) of an Agilent 7890 gas chromatograph. The sample was then carried onto a Bruker BR-5MS column via He carrier gas (99.999 %, 0.68 mL min^{-1} flow rate). The temperature profile of the oven was set to obtain maximum species separation during a 22-minute acquisition (hold at 35 $^{\circ}\text{C}$ for 5 minutes, ramp to 100 $^{\circ}\text{C}$ over ~4.3 minutes, ramp to 240 $^{\circ}\text{C}$ over ~4.7 minutes, then hold at 240 $^{\circ}\text{C}$ for 5 minutes). After traveling the column, species were transferred to the mass spectrometer. The Agilent 5977B mass spectrometer

uses electron ionization (70 eV, 200 °C ion source) to create charged species and a quadrupole to filter mass to charge ratios before reacting the detector.

Calibration solutions were prepared from analytes of known concentration (DMC, EMC, EC, DEC, FEC, VC, Dimethyl-2,5-dioxahexane carboxylate (DMOHC), MMDS, DTD, Diethyl-2,5-dioxahexane carboxylate (DEOHC), and MA). Purity of these analytes are listed in supplemental Table B-1. Any effect of the small levels of impurities on the calibration concentration is considered negligible. The calibration solution is then further diluted to generate a five to six-point calibration curve (with a quadratic equation with $r^2 > 0.998$). Samples underwent duplicate injections to determine replicate deviation while the variation in replicate calibration solution samples (before and after unknown sample testing) were used to estimate standard deviation of each analyte (~4 %).

Calculation for Salt Concentration and Error

Previous methods of determining salt concentrations relied on measuring the amount of salt in a known mass or volume of pure solvent. Since most aged Li-ion cells have small volumes of solvent, a liquid extraction was most practical to remove electrolyte. Therefore, instead, this method was developed to quantify both the moles of salt as well as mass of solvent in the same extracted sample. The mass of EC in the sample (determined from q-NMR) and the relative masses of all solvents (determined from GC-MS) were used to calculate the masses of all solvents in the sample. The individual masses then were combined to calculate the total mass of solvent in the sample. The moles of salt (determined by q-NMR) was then divided by the total kilograms of solvent to give molality of salt in the sample. The relative standard deviation in the NMR instrumentation is 2.4 % for ^1H

and 1.5 % for ^{19}F .⁴⁰ This variation, combined with replicate variation as well as variation associated with GC-MS (~4 %), is on average ~5 % relative standard deviation for salt concentrations.

XRF Principles

Figure 3-10 shows the mechanism of fluorescence radiation in an atom. X-ray fluorescence spectroscopy uses X-ray radiation (typically from a Ru source) to expel electrons from the inner, lower energy orbitals (K or L shell) of an atom (as in Figure 3-10a.). The fluorescent radiation is generated as electrons drop from higher energy orbitals to fill the vacancies at the lower energies (Figure 3-10b.). The energies emitted are characteristic and unique for different elements. XRF is typically limited to detecting elements with atomic number greater than eight since it is often difficult to detect low energy photons produced by atoms with lower atomic numbers with current technology. Additionally, much of the radiation produced by low atomic number atoms is often reabsorbed by the sample material or environment, interfering with quantification.¹¹⁷ Still, XRF can be especially useful for identifying and quantifying the amount of transition metals transferred from the positive electrode to the negative electrode in Li-ion batteries.

Where typical XRF instrumentation requires a uniform, homogeneous sample, μXRF instruments use advanced optics to focus the excitation beam into a small sample area (as small as $80\ \mu\text{m}^2$) and can focus the emitted fluorescence to the detector.^{117,118} This allows for a small sample area to be measured and, when combined with a moving sample stage, for a two-dimensional map of elements to be generated. Quality of XRF measurements can also suffer from interference within the sample. Often emitted energies from an element

can induce fluorescence in another, neighboring element inducing secondary fluorescence. This can result in falsely low or high characteristic signals for elements present in sample.

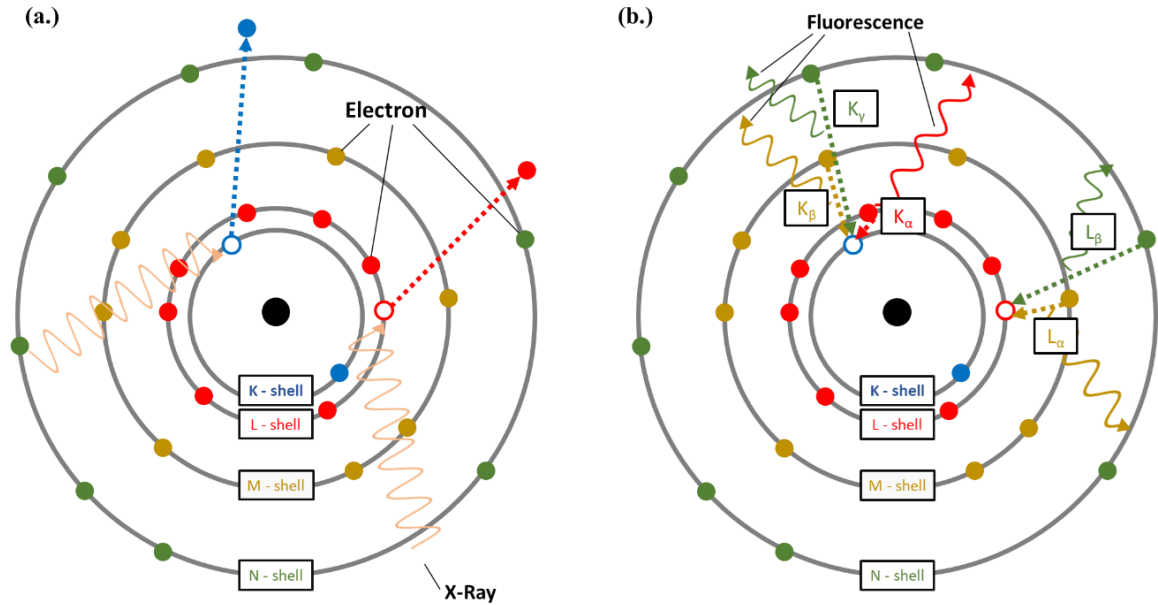


Figure 3-10 – Mechanism of fluorescent X-ray generation. Panel (a.) shows the ejection of lower energy electrons (K or L shell) creating an electron vacancy. Panel (b.) shows examples of radiation that can form when electrons drop from higher energy orbitals.

The phenomenon was previously overcome by comparing homogenous samples with homogeneous certified reference materials. Currently, more modern solutions to address the extent of secondary (and tertiary) fluorescence aims to model the interference using fundamental parameters. The result applies a physics-based model to predict the resulting spectrum and aids in the analysis of the measured spectrum to quantify elemental compositions.¹¹⁸ The author thanks A. Eldesoky (Dahn Laboratory) for making the XRF measurements.

μ XRF Specifications

μ XRF analysis was conducted as previously described by Thompson et al.⁷⁷ In summary, a M4 Tornado Micro-X-Ray Fluorescence instrument (Bruker, Madison, WI, USA) was used to quantify the presence of transition metals on a representative section of the negative electrode. Pristine graphite electrodes were sputter-coated with a linear gradient of Ni, Co, and Mn to calibrate signal count to a known mass concentration in terms of $\mu\text{g cm}^{-2}$. The calibrants were scanned using on the μ XRF and an average ratio of signal count per area to mass per area was calculated from four different positions along the calibrant. The fractional error in the data was taken to be the same as the ratio of the standard deviation of the four calibration measurements divided by their average. Samples and calibration standards were taped on a poly-acrylic plate and placed on a motion stage in a vacuum sealed chamber (>20 mbar). μ XRF scanning was done using a Rh X-Ray tube (200 μA tube current) in the 0-50 keV range, a scanning rate of 4 mm sec^{-1} and a spot size of 25 μm with either a 40 or 100 μm step. Signal calibration was carried out at 40 and 100 μm step sizes. Negative electrodes from pristine dry cells and freshly formed cells were scanned to determine any Ni, Mn, and Co traces. For pristine cells, Ni, Mn, and Co loadings were indistinguishable from the background. For freshly formed NMC532 cells, the Ni signal was indistinguishable from the background, while Mn and Co loadings were (0.23 ± 0.01) $\mu\text{g cm}^{-2}$, and (0.05 ± 0.01) $\mu\text{g cm}^{-2}$ (4.3 V UCP). For freshly formed NMC622 cells, Ni and Co loadings were indistinguishable from the background, while Mn loading was (0.23 ± 0.01) $\mu\text{g cm}^{-2}$ (4.3 V UCP).

CHAPTER 4 – ELECTROLYTE AND ELECTRODE STUDY VERSUS TIME

Results presented in this section have been published in *J. of Electrochem. Soc.*, **168** (2), 020532 (2021) and are reproduced, with permission, from Electrochemical Society (ECS) per copyright agreement (see Appendix C). Author contributions to this work include performing electrolyte analyses, preparing samples, tracking samples, compiling, analyzing, and presenting data, and writing of final manuscript. W. Stone made the matrix of cells, J. Harlow performed storage experiments and dV/dQ analysis, M. Bauer performed DTA measurements, and A. Eldesoky performed μ XRF analysis. All figures, except for those indicated, were produced by the author.

Motivation for Studying Long-Term Electrolyte Changes

Electrolyte design is an inexpensive way to improve the lifetime, improve the safety, and increase the charge rate capability of Li-ion cells.⁴⁵ Electrolytes can be altered via salt and solvent selection to achieve maximum conductivity and with additives to limit the parasitic reactions which hinder cell lifetime. Recently, Harlow et al. showed that cells with electrolytes containing the additives vinylene carbonate (VC) and ethylene sulfite (DTD) can last over 5000 cycles and over 3 years, with projections for 20 year lifetime at 20 °C.²³

Previous studies of Li-ion cell degradation have identified reactions such as the reduction of carbonates at the negative electrode, oxidation at the positive electrode,^{27,28,45} secondary reactions within the electrolyte,^{27,51,75,76} transition metal dissolution and deposition,^{78,81,82,119} and production and dissolution of gases.¹²⁰ These works and many

others have contributed to understanding the degradation mechanisms of Li-ion cells. However, due to limitations of charger and instrument availability, many of these studies are limited to a few charge and discharge cycles. As a result, little is known of the changes to Li-ion cell electrolyte that occur during long-term testing. While electrolyte is normally optimized at the beginning of life, changes to electrolyte composition during aging (such as decrease in conductivity, increase in viscosity) could affect cell performance later in life. Reactions occurring in electrolytes and reactions between the electrodes and electrolytes can often be symptoms of cell failure mechanisms. If these reactions can be identified then inhibited, longer-lasting, more tolerant electrolytes may be possible.

In this chapter, electrolyte composition is measured from aged cells throughout their lifetime. This work uses a new electrolyte extraction technique⁴⁰ presented in Chapter 3 to study electrolyte from cells 3 to 12 months old. This study was conducted to compare cycling and storage results for cells with two different positive electrode materials and established electrolyte blends at various temperatures, upper cutoff potentials (UCP), and times. Cells underwent post-cycling analysis (described in more detail in Chapter 3), including electrochemical impedance spectroscopy (EIS), and differential voltage analysis, before disassembly for electrolyte analysis, via gas chromatography-mass spectrometry (GC-MS) and quantitative nuclear magnetic resonance (q-NMR), and electrode analysis, via micro X-Ray fluorescence (μ XRF) spectroscopy.

This design matrix involved over 130 cells and a year of cycling and storage resources. Table 4-1 provides variables included in this study. Two upper-cutoff potentials and storage temperatures were used to identify how electrochemical potential and temperature affect cell performance and chemical changes. If electrolyte and electrodes are stable at

higher upper cutoff potentials, it may be possible to increase cell energy density with no penalty by operating at higher potentials. Cells were also cycled or stored to observe the outcome of the parasitic reactions induced by cycling or storage at high states of charge. These variables highlight the consequences of increased cycling or storage temperature and/or long-term storage at top of charge for Li-ion battery applications.

Table 4-1 – Table of variables included in matrix design for long-term electrolyte study.

Pos. Electrode Materials and Electrolytes	NMC532 (Single Crystal) 1.1 m LiPF ₆ in EC:EMC (3:7) + 2% VC + 1% DTD	NMC6222 (Polycrystalline) 1.1 m LiPF ₆ in EC:EMC (3:7) + 2% VC + 1%MMDS + 1% LFO		
Protocols	Cycling	Storage		
Temperatures	40 °C	55 °C		
Upper Cutoff Potentials	4.3 V	4.4 V		
Test Periods	3 months	6 months	9 months	12 months

Cells and Electrolytes in this Study

Pouch cells containing two different positive electrodes (single crystal NMC532 and polycrystalline NMC622) and AML-400 negative electrodes were used in this long-term study. The dried cells were filled with electrolyte according to the methods provided in Chapter 3. The electrolyte mixture included 1.1 m LiPF₆ in EC:EMC (3:7 wt./wt.%) with 2%VC and 1% DTD additives in NMC532 cells and 1.1 m LiPF₆ in EC:EMC (3:7 wt./wt.%) with 2% VC, 1% LiPO₂F₂, and 1% MMDS in NMC622 cells (see Appendix C for names, abbreviations, sources, and purities). These electrolytes were chosen for their excellent

performance with these cell chemistries.^{23,36,85,86} Cells were sealed, wet for 24 hours, and formed according to the methods presented in Chapter 3. Prior to cycling gas measurements, EIS spectra, and UHPC capacities were collected (please see Chapter 3).

Cycling and Storage

Cells of each chemistry were cycled at two temperatures (40 °C and 55 °C) and two upper cutoff potentials (4.3 V and 4.4 V) following the cycling protocol (at C/3 charge/discharge rate) described previously (please also see Figure 3-4). Due to limited charger space, some cells were paired during cycling. Post-cycling UHPC analysis of the individual cells determined the low-rate capacity that is reported in subsequent sections. Additionally, cells underwent open circuit storage at two temperatures (40 °C and 55 °C) and two upper cutoff potentials (4.3 V and 4.4 V). The capacities of these cells were also determined post-storage via UHPC analysis. Eight replicate cells for each chemistry and each condition were made. This allowed cells to be removed every three months for a 12-month total study. Due to accelerated capacity loss in NMC622 cells at 55 °C and with 4.4 V upper cutoff potential, the timeline for removal was adjusted to a maximum of nine months cycling. All cells underwent gas, EIS, UHPC, DTA, NMR, GC-MS, and μ XRF measurements after testing. Please see Chapter 3 for complete, detailed methods.

Cell Cycling Results

Figure 4-1 shows the capacity versus cycle number results for NMC532 cells (panels a. and c.) and NMC622 cells (panels b. and d.) at 55 °C (panel a. and b.) and 40 °C (panel c.

and d.). Cells cycled to an upper cutoff potential of 4.3 V are shown in black and those to 4.4 V are shown in red. The cycling results show that NMC532 cells had good capacity retention (>90%) throughout the year long sample period. NMC622 cells, however, especially those at higher cycling temperature and higher upper cutoff potential, started to experience increased rates of capacity fade. The overlap of cycled cells under the same conditions shows the repeatability of these machine-made cells. Cells were removed about every three months during this 12-month period. Some of these cells at high temperature and 4.4 V upper cutoff potential were removed ahead of schedule due to increased rates of capacity loss.

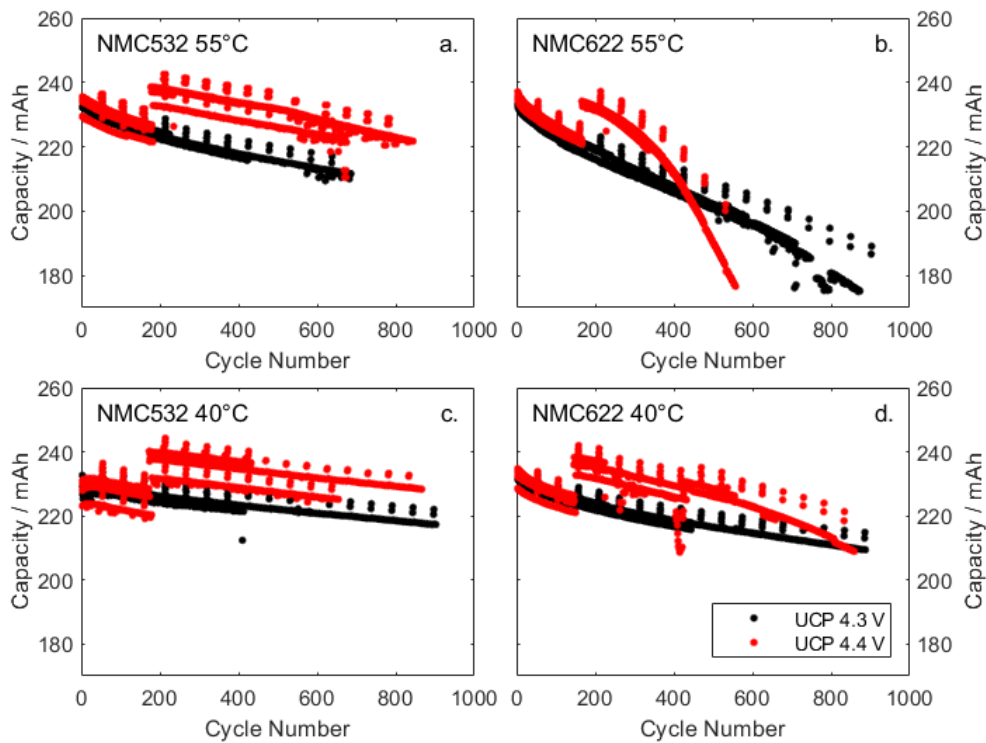


Figure 4-1 – Capacity versus cycle number results for cells cycled at C/5 CCCV to 4.3 V UCP (black) and 4.4 V UCP (red). Panels a. and c. show results for NMC532 at 55 °C and 40 °C, respectively. Panels b. and d. show results for NMC622 at 55 °C and 40 °C, respectively. The 4.4 V cells were tested to an upper cutoff of 4.3 V (in error) for their first 170 cycles).

Capacity, Voltage Polarization, Gas and Charge Transfer Impedance Results

Since cells which underwent storage testing were not fully charged and discharged until the end of their test period, the low-rate discharge capacity was determined for all cycled and stored cells after testing. Figure 4-2 summarizes results for NMC532 cells after cycling (blue squares) and storage (orange circles) experiments versus time (months). Data point markers are filled to indicate the length of test; 3 mo. to 12 mo. (black to white, respectively). The numbers of completed charge and discharge cycles are not shown, however, cells cycled to 4.3 V for 12 months achieved over 900 cycles as shown in Figure 4-1. Figures 4-2(a. – d.) show the end discharge capacity for cells at 40 °C (a. and b.) and 55 °C (c. and d.) and with upper cutoff potentials of 4.3 V (a. and c.) and 4.4 V (b. and d.). The cells charged to higher upper cutoff potentials have larger initial capacity, as expected. The discharge capacity (uncertainty determined by replicate cells) decreased slightly over 12 months for cycled cells at 40 °C ((9.8 ± 0.6) mAh for 4.3 V UCP and (13.6 ± 0.9) mAh for 4.4 V UCP) and more for cells at 55 °C ((22 ± 2) mAh for 4.3 V UCP and (21 ± 3) mAh for 4.4 V UCP). Stored cells at 40 °C lost a small amount of capacity after 12 months ((14 ± 5) mAh for 4.3 V UCP and (16 ± 5) mAh for 4.4 V UCP) and more for cells at stored at 55 °C ((29 ± 4) mAh for 4.3 V UCP and (30 ± 1) mAh UCP 4.4 V).

Figures 4-2(e. – h.) show the normalized capacity for cells in the same respective conditions as Figures 4-2(a. – d.). Cells cycled at 40 °C show minimal relative capacity loss after 12 months (~6%), whereas cells stored at 55 °C show the most relative capacity loss after 12 months (~14%). Cycled and stored cells at 40 °C show minimal observable difference in normalized capacity, however, stored cells at 55 °C have a lower normalized capacity than their equivalent cycled cell, indicating capacity retention is dependent on

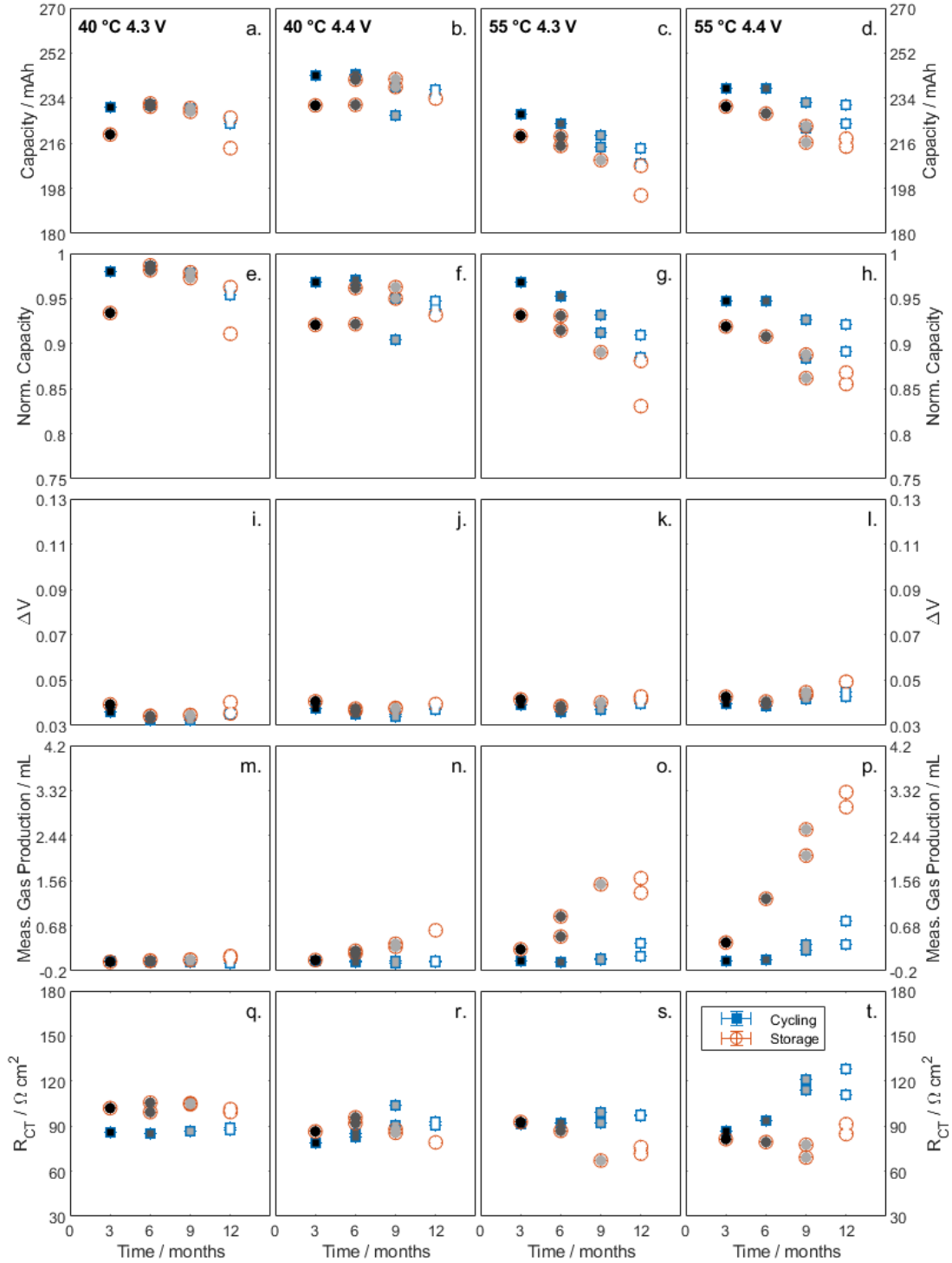


Figure 4-2 – Results from NMC532 cycled and stored cells (blue squares and orange circles, respectively) versus time. Panels (a.-d.) include the cycling or storage conditions for the columns of below. Panels (a.-d.) show discharge capacity at end of test, and panels (e.-h.) show the normalized discharge capacity. Panels (i.-l.) show ΔV at the end of testing. Panels (m.-p.) show the volume of gas produced during testing via Archimedes' measurement. Panels (q.-t.) show R_{CT} estimated via EIS.

temperature and time at upper cutoff potentials. Figures 4-2(i. – l.) show the voltage polarization (ΔV). The change in voltage polarization has previously been shown to be proportional to DC impedance growth.¹²¹ Results for NMC532 showed minimal change in ΔV and little observable difference between cycled and stored cells at all temperatures and upper cutoff potentials. [Note that the y-axis scale has been selected for comparison to the NMC622 cells in Figures 4-3(i. – l.)].

Figures 4-2(m. – p.) show the measured gas production. Gas production remains low (<0.5 mL) throughout the observation period for most cycled cells and for cells stored at 40 °C and 4.3 V UCP. When the storage upper cutoff potential increased from 4.3 V to 4.4 V at 40 °C, gas production increased slightly to (0.6 ± 0.2) mL over the 12-mo. observation period (standard deviation based on replicate cells, $n = 2$). When the storage temperature increased from 40 °C to 55 °C, the gas production for stored cells occurs at a higher rate until reaching (1.4 ± 0.1) mL (4.3 V UCP) and (3.1 ± 0.1) mL (4.4 V UCP) after 12 months. For cells that experienced increased gas production, it is possible to observe a linear, constant rate of gas production. When the temperature is increased from 40 °C to 55 °C, the rates approximately quadrupled. When the upper cutoff potential is increased from 4.3 V to 4.4 V, gas production doubles. This indicates both temperature and storage upper cutoff potential can increase the rate of gas production. While gas analysis was not performed on these cells, it is expected the gas created at higher upper cutoff potential is due to CO₂ production.⁶⁸ The difference between cycling and stored cells could be due to the longer time spent at the higher potential for the stored cells.

Figures 4-2(q. – t.) show the effective charge transfer resistance measured by EIS at 10 °C. This includes desolvation and resistance of ion transport through the SEI layers at both

electrodes.⁹⁵ For similar NMC532 cells, it has been shown that the increase in charge transfer resistance is primarily from the positive electrode/electrolyte interphase.¹²² For cells cycled or stored at 40 °C there were minimal changes to the charge transfer resistance throughout the 12-month period. For cells cycled at 55 °C, there was minimal change to charge transfer resistance at 4.3 V, however, when the upper cutoff potential increased to 4.4 V, the charge transfer resistance increased throughout the observation period. Stored cells at 55 °C, with both upper cutoff potentials, did not incur large changes to charge transfer resistance.

Figure 4-3 summarizes similar results as Figure 4-2, but for polycrystalline NMC622 cells during cycling and storage experiments. Markers, scales, dependent variables, and conditions are consistent with Figure 4-2 for ease of comparison. Figures 4-3(a. – d.) show the discharge capacity at the end of cycling or storage. Cells stored at 40 °C had the least capacity loss during the 12-month period ((10.0 ± 0.4) mAh for 4.3 V UCP and (11.6 ± 0.9) mAh for 4.4 V UCP) where cycled cells had higher capacity loss ((17.0 ± 0.3) mAh for 4.3 V UCP and (19.8 ± 0.7) mAh for 4.4 V UCP). Stored cells at 55 °C had lower capacity loss during the 12-month period ((27 ± 2) mAh for 4.3 V UCP and (29 ± 2) mAh for 4.4 V UCP) than cycled cells at 55 °C ((35 ± 1) mAh for 4.3 V UCP and (39.4 ± 0.4) mAh for 4.4 V UCP). Figures 4-3(e. – h.) show the normalized capacity. Cells cycled at 40 °C showed about 8 % relative capacity loss for both upper cutoff potentials during the 12-month observation period. When the temperature is increased to 55 °C, the relative capacity decreases by about 20 % for the 12-month period in cells cycled to 4.3 V UCP and in the 7.5-month period for cells cycled to 4.4 V. Stored cells at both temperatures appear to retain slightly higher relative capacity over the observation periods (~ 5 % and ~13 % relative

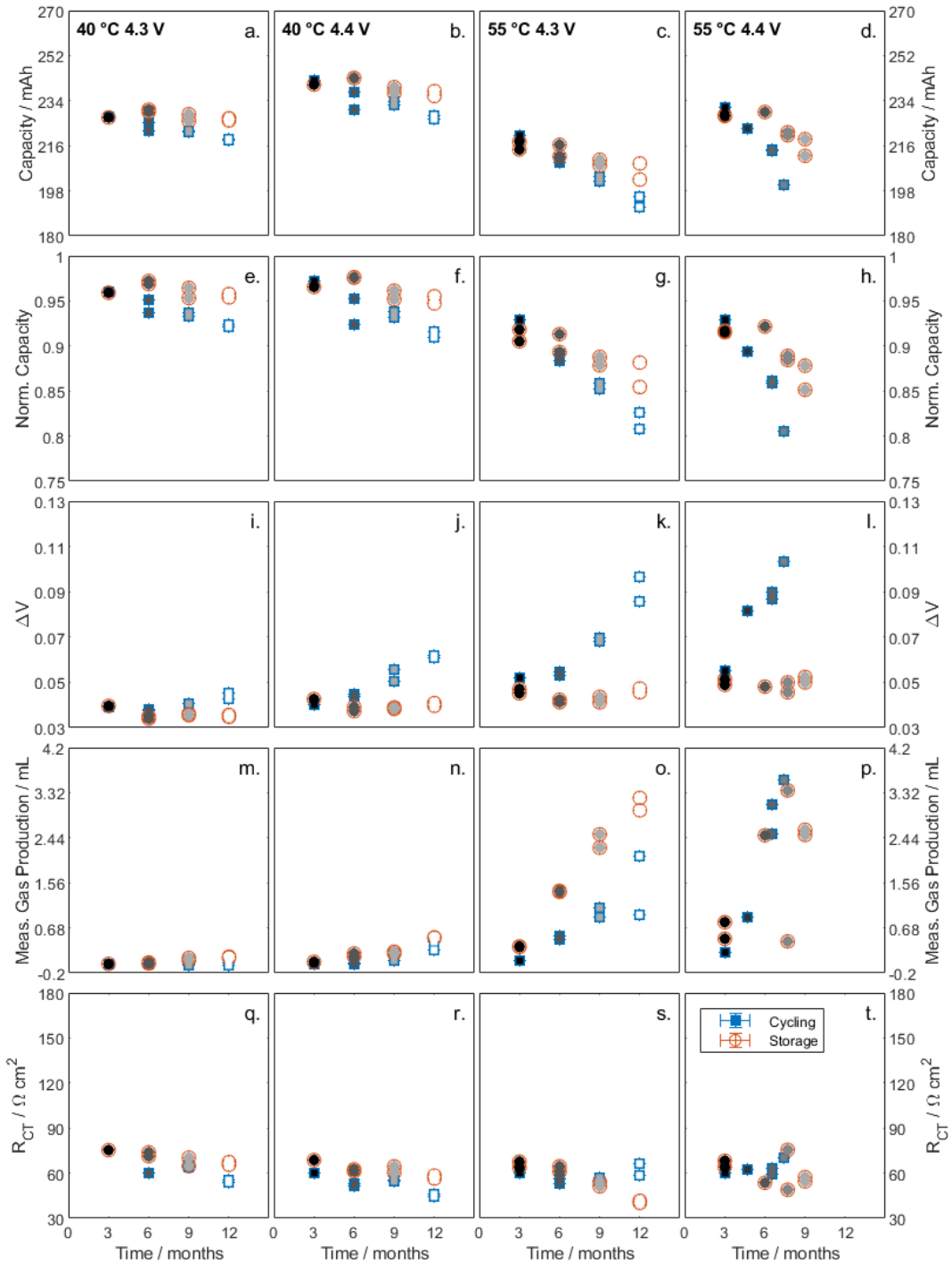


Figure 4-3 – Results from NMC622 cycled and stored cells (blue squares and orange circles, respectively) are presented versus time. Panels (a.-d.) include the cycling/storage conditions for the panels that follow below. Panels (a.-d.) show ending discharge capacity and panels (e.-h.) show the normalized discharge capacity. Panels (i.-l.) show ΔV at the end of testing. Panels (m.-p.) show the volume of gas produced during testing via Archimedes' measurement. Panels (q.-t.) show R_{CT} estimated via EIS.

capacity loss in cells at 40 °C and 55 °C, respectively). As mentioned in the Methods section, cells cycled and stored at 55 °C with UCP of 4.4 V were removed after ~7.5 and 9 months, respectively, rather than completing the 12-month testing due to rapid capacity loss. For ease of comparison on these figures, the marker fill is consistent with cell age. For example, in Figures 4-3(g. and h.) the 9-month cells are filled with the same shade.

Figures 4-3(i. – l.) show the voltage polarization versus time. Results for stored cells show minimal change in ΔV versus time at all upper cutoff potentials and temperatures. Results for cycled cells show minimal change at 40 °C and an UCP of 4.3 V. ΔV increased slightly when the upper cutoff potential was increased and more significantly when the temperature was increased. Increasing the temperature and upper cutoff potential compounded the effect on ΔV for cycled cells.

Figures 4-3(m. – p.) show the measured gas production. Gas production is minimal (< 0.5 mL) for all cycled and stored cells at 40 °C. When the storage temperature is increased from 40 °C to 55 °C, the gas production for stored cells occurs at a higher rate, reaching (3.1 ± 0.1) mL (4.3 V UCP) and (2.55 ± 0.05) mL (4.4 V UCP) over 12 and 9 months, respectively. Cells cycled at 55 °C showed an increase in gas production to (1.5 ± 0.6) mL over 12 months for 4.3 V UCP and over 7.5 months to (3.7 ± 0.1) mL for 4.4 V UCP. The larger volumes (greater than about 3 mL) are at the upper limit of what is measurable via Archimedes method. As discussed in Chapter 3, it is likely that gas pressure is no longer at standard temperature and pressure to accurately quantify with this method.

Gas generation in the NMC622 cells appears to be linear with time under most conditions. Data from cells at 55 °C with an UCP of 4.4 V show increased variability for older stored cells (7.5 and 9 months). It is expected that the outlying storage cell data point at ~7 months

is due to pouch bag rupture. For most conditions, there is minimal difference between gas produced in cycling versus storage cells. However, at 55 °C and to an UCP of 4.3 V, stored cells have about twice the gas produced than cycled cells.

Figures 4-3(q – t.) show the charge transfer resistance measured by EIS. For cells cycled and stored at 40 °C, there was a slight decrease in charge transfer resistance throughout the 12-month period. Cells stored at 55 °C also showed a small decrease in charge transfer resistance at both upper cutoff potentials (except for the 7-month cell at 4.4 V). For cells cycled at 55 °C, there was minimal change to charge transfer resistance at 4.3 V and 4.4 V UCPs. Minimal changes to charge transfer resistance indicate there was minimal SEI impedance growth. This suggests the large changes observed in ΔV for NMC622 cells cycled at 55 °C originated from a different source.

Most noticeable differences between results from NMC532 cells and NMC622 cells (Figure 4-2 and Figure 4-3) include higher relative capacity loss in NMC622 cells cycled and stored at 55 °C, significantly higher ΔV growth in cycled NMC622 cells, more gas production in NMC622 cycled cells at 55 °C and smaller changes in charge transfer resistance for NMC622 cells cycled to 4.4 V UCP at 55 °C compared to NMC532 cells at the same condition.

EIS and dV/dQ Results

Figure 4-4 summarizes EIS and dV/dQ results for NMC532 and NMC622 cells after cycling and storage. Here, the change in measurement (per month) was calculated using the slope of the data (fitted via linear regression) and reported versus testing temperature.

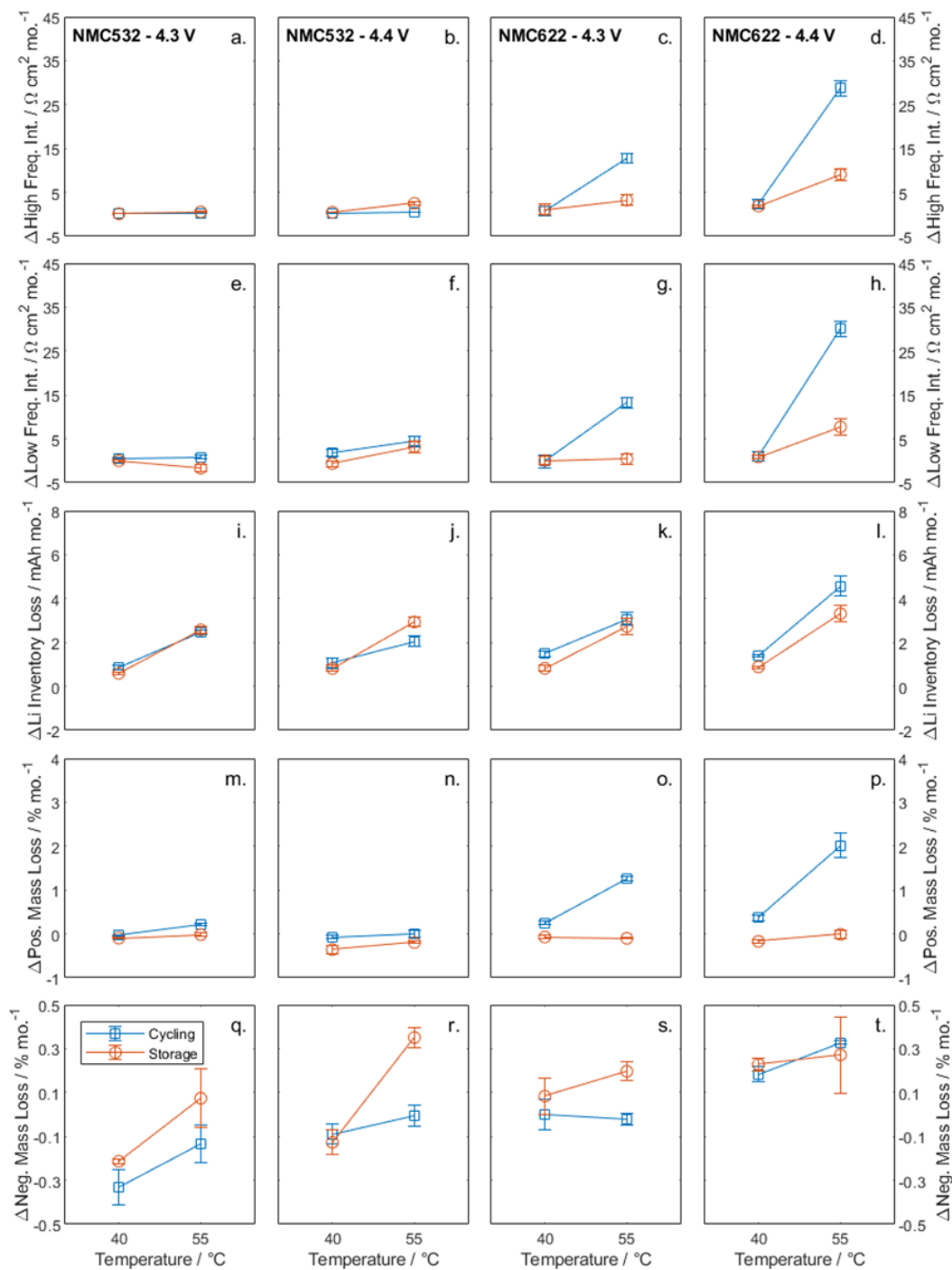


Figure 4-4 – Post-cycling/storage results from cycled and stored cells (blue squares and orange circles, respectively) are presented versus test temperature. Panels (a.-d.) include the cell type and UCP for the panels that follow below. Panels (a.-d.) show the change in high frequency intercept per month and panels (e.-h.) show the change in low frequency intercept per month measured via EIS. Panels (i.-l.) show change in Li inventory loss per month and panels (m.-p.) show the change in positive electrode mass loss per month measured via UHPC. Panels (q.-t.) show the estimated change in negative electrode mass loss percent per month measured via UHPC.

For example, the change in high frequency intercept per month versus cycling or storage temperature is shown in Figures 4-4(a. – d.). Panels a. and b. show results from NMC532 cells and panels c. and d. show results from NMC622 cells. Panels a. and c. show results from cells with 4.3 V UCP. Panels b. and d. show results from cells with 4.4 V UCP. Blue square markers indicate data from cycled cells while orange, circle markers from stored cells. Error bars show the calculated error based on weighted regression. Most linear fits did not include fixed intercepts, however some linear fits included fixed intercepts where values at zero months were expected to be zero (transesterification, dimerization, Li inventory loss, positive mass loss, negative mass loss). Figures showing raw data for NMC532 and NMC622 cells (like Figure 4-3, respectively) are provided in supplementary material (Figure A-1, Figure A-2, Figure A-4, and Figure A-5) and provide individual measurement errors.

Figures 4-4(a. – b.) show minimal changes ($<5 \Omega \text{ cm}^2 \text{ mo.}^{-1}$) to the high-frequency intercept of EIS measurements at both 40 and 55 °C, indicating little change to the electron path resistance through the electrodes and/or ionic path resistance through the electrolyte in NMC532 cells.^{92,121} Figures 4-4(e. – f.) show the low frequency intercept (HFI + charge transfer resistance) also has minimal change ($<5 \Omega \text{ cm}^2 \text{ mo.}^{-1}$) at both 40 and 55 °C for NMC532 cells.

Figures 4-4(i. and j.) show results from dV/dQ fitted Li inventory loss (due to negative electrode SEI growth) versus temperature for cells with an UCP of 4.3 V and 4.4 V, respectively. A limited number of NMC532 cells underwent dV/dQ fitting due to limited charger availability. The Li inventory loss is estimated using the change in electrode slippage and the estimated mass loss as described in supplemental information Figure A-3

and Equation A-1 and Equation A-2. The rate of Li inventory loss is shown to increase for NMC532 cells from 40 to 55 °C to a maximum of ~3 mAh mo.⁻¹. The rate of Li-inventory loss is also similar for cells with a 4.3 V UCP versus a 4.4 V UCP. An example the results of dV/dQ fitting to extract the parameters needed for the Li inventory calculation for NMC622 cells is illustrated in supplementary Figure A-6. Li inventory losses are also consistent with the respective absolute capacity loss measured in these cells. The rate of increase in Li inventory loss is larger for cells cycled or stored at higher temperatures. The rates of active positive and negative material loss were also determined by dV/dQ fitting and are shown in Figures 4-4(m. and n.) and Figures 4-4(q. and r.), respectively. These rates show <5 % change in active mass over 12 months for both electrode materials indicating minimal changes to the electrode materials.¹⁰¹ Thus, in these cells, the dominant capacity loss mechanism is Li inventory loss building the SEI at the negative electrode. Based on Figures 4-2(q. and r.) this does not increase the charge-transfer resistance of the cell significantly, suggesting the composition of the SEI must change over time or that the negative electrode SEI plays a small role, compared to the positive electrode in making up R_{CT} .

Figure 4-4 also shows EIS and dV/dQ results versus test temperature for NMC622 cells after cycling and storage. Figures 4-4(c. and d.) show the rate of high frequency intercept (HFI) change determined via EIS. For cells cycled and stored at 40 °C, there is minimal change to this intercept (< 40 Ω cm² over 12 months), indicating little change to the electronic path resistance through the electrodes and the ionic path resistance through the electrolyte.^{92,121} The results for cycling versus stored cells are similar. For cells cycled and stored at 55 °C, however, the rate of high frequency intercept increases to as much as ~160

$\Omega \text{ cm}^2$ over 12 months for cells cycled to 4.3 V and $\sim 150 \Omega \text{ cm}^2$ over 9 months for cells cycled to 4.4 V. Cells stored at 55 °C show about 1/3 the change in high frequency intercept as the equivalent cycled cells throughout the observation period. The rate of high frequency intercept increase is slightly higher for cells cycled to 4.4 V than 4.3 V UCP. These results indicate that at higher temperature, the electronic and/or ionic path resistances increases at a higher rate, indicating solution or electrode changes. The increase in HFI is like that seen in ΔV for the same cells (Figures 4-3(i. – 1.)), suggesting that electronic resistance increases in the electrodes, or increases in the ionic path resistance are responsible for the changes in cell polarization with time. We will return to this point later once electrolyte compositions have been discussed.

Figures 4-4(g. and h.) show the changes in low frequency intercept for cycled and stored cells. At 40 °C, the low frequency intercept has minimal change from the intercept measured at 3 months ($\sim 95 \Omega \text{ cm}^2$). Cells stored at 55 °C also have minimal change over 12 months when held at 4.3 V, however, when held at 4.4 V UCP, there is an increase in rate (up to $\sim 150 \Omega \text{ cm}^2$ for the 9-month period). Cells cycled at 55 °C show the highest change in low frequency intercept throughout the observation period. The low frequency and high frequency intercept are used to determine the charge transfer resistance as provided in Figure 4-2 and Figure 4-3. For NMC622 cells, it appears all resistance increase is attributed to the electron/ion path resistance rather than the charge transfer resistance. Origins of electron or ion path resistance increase could be from changes to electrolyte or electrode conductivity, such as compositional changes to electrolyte or particle cracking in the electrode, respectively.

Figures 4-4(k. and l.) show the rate of Li inventory loss calculated via dV/dQ fitting as described by Dahn et al.¹⁰¹ At 40 °C, a slight increase in Li inventory loss was observed and was similar for both cycled and stored cells with UCPs of 4.3 V and 4.4 V. When the temperature increased to 55 °C the rates of Li inventory loss increased for cycled and stored cells. Increasing upper cutoff potential exaggerates these effects. These results indicate Li inventory loss increases over time for all cycled and stored NMC622 cells. Supplementary Figure A-3 shows exemplar data to illustrate how Li inventory loss was determined in cells which experienced positive electrode mass loss. Figure A-6 shows voltage versus capacity data from NMC622 cells in this study.

The active mass change on either electrode is estimated via dV/dQ fitting as described by Dahn et al.¹⁰¹ Figures 4-4(o. and p.) show the rate of positive electrode active mass loss. Again, at 40 °C, there was minimal change to the active mass of positive electrode and minimal difference between cycled and stored cells. When the temperature was increased to 55 °C and the UCP kept at 4.3 V, the rate of positive electrode active mass loss remained constant for stored cells but increased to triple that of the equivalent cell at 40 °C for cycled cells. Finally, when the upper cutoff potential was also increased to 4.4 V at 55 °C, the rate of positive active mass loss in cycled cells is over quadruple the loss of the equivalent cells at 40 °C. Positive mass loss could be due to micro-cracked particles, which is consistent with the observed increase in high frequency intercept. This is likely related to the repeated expansion and contraction of positive electrode materials undergoing many cycles, whereas cells stored at upper cutoff potentials experienced little expansion and contraction and positive active material loss. Results from dV/dQ analysis have a strong correlation to observed cell performance.

Other capacity loss mechanisms in the literature include rock salt surface layer formation¹²³ or acid dissolution of the positive material.^{80,124} Each of these mechanisms can lead to positive electrode active material loss. Microcracks create fresh surfaces for acid attack and, in the acid dissolution mechanism, LiPO_2F_2 is expected to be produced.¹²⁵ ^{19}F -NMR allows LiPO_2F_2 to be identified qualitatively. While q-NMR showed that LiPO_2F_2 concentrations remained relatively low for most cells, it is worth noting that the largest concentrations of LiPO_2F_2 (< 50 mM) were measured in older cycling and stored NMC622 cells at 55 °C. Figure A-7 shows an example ^{19}F -NMR spectra and the relative magnitude of the LiPO_2F_2 peaks. While all samples (including those prepared with fresh electrolyte) showed the weak PF_5 peak, not all samples showed LiPO_2F_2 peaks. Cycled cells could develop microcracks which could accelerate acid attack, while stored cells were held at high voltage for long durations which also accelerates acid attack. Even though cycled NMC622 cells had more positive active mass loss than stored cells, it is possible for the amounts of created LiPO_2F_2 to be similar.

Figures 4-4(s. and t.) show the rate of negative active mass loss for these NMC622 cells. For all cells, there is minimal change to the negative electrode active mass. The small variations observed could simply be due to the quality of the dV/dQ fitting. Considering Figure 4-4, some major differences between single crystal NMC532 cells and polycrystalline NMC622 cells can be observed. This includes increased change to high frequency intercept for NMC622 cells under all conditions, indicating a more rapid change to electrolyte and/or electrode resistance. The NMC532 cells under all conditions show virtually no changes to active electrode masses with all capacity loss due to Li inventory loss. By contrast, cycled NMC622 cells at 55 °C show significant positive electrode active

material loss as well as Li inventory loss. This difference is primarily attributed to the fact that NMC532 particles, which are resistant to microcracking,¹²⁶ are single crystals while NMC622 particles are polycrystalline. Li et al. have clearly shown the advantages of single crystal NMC532 over polycrystalline NMC532.⁸³ Additionally, NMC532 and NMC622 have similar volume changes (versus potential and versus lithium content) in this potential range (< 4.4 V).¹²⁷ Therefore, any differences in structural changes between the two materials are minor and, instead, differences in active material loss are attributed to single crystal versus polycrystalline particles.

Electrolyte and Negative Electrode Analysis

Figure 4-5 summarizes electrolyte and negative electrode chemical analysis for NMC532 and NMC622 cells. Markers, conditions, positive electrode material, and rate/error calculations are consistent with Figure 4-4. Individual cell results per time (replicate cells shown, when available), as well as their measurement error, are shown in supplementary Figure A-4 and Figure A-5.

Figures 4-5(a. and b.) show the change in measured PF_6^- concentrations for NMC532 cells. This concentration was determined as described in the Methods section. The error bars shown in supplementary Figure A-4 and Figure A-5 represent the propagated error from $^1\text{H-NMR}$ (~2.4 %), $^{19}\text{F-NMR}$ (~1.5 %) and GC-MS (~4 %) measurements. Considering the large cell variability and the large variability in error associated with rate calculations, it is not possible to determine significant differences between change in PF_6^- concentrations measured for cells with different upper cutoff potentials, nor to differentiate between

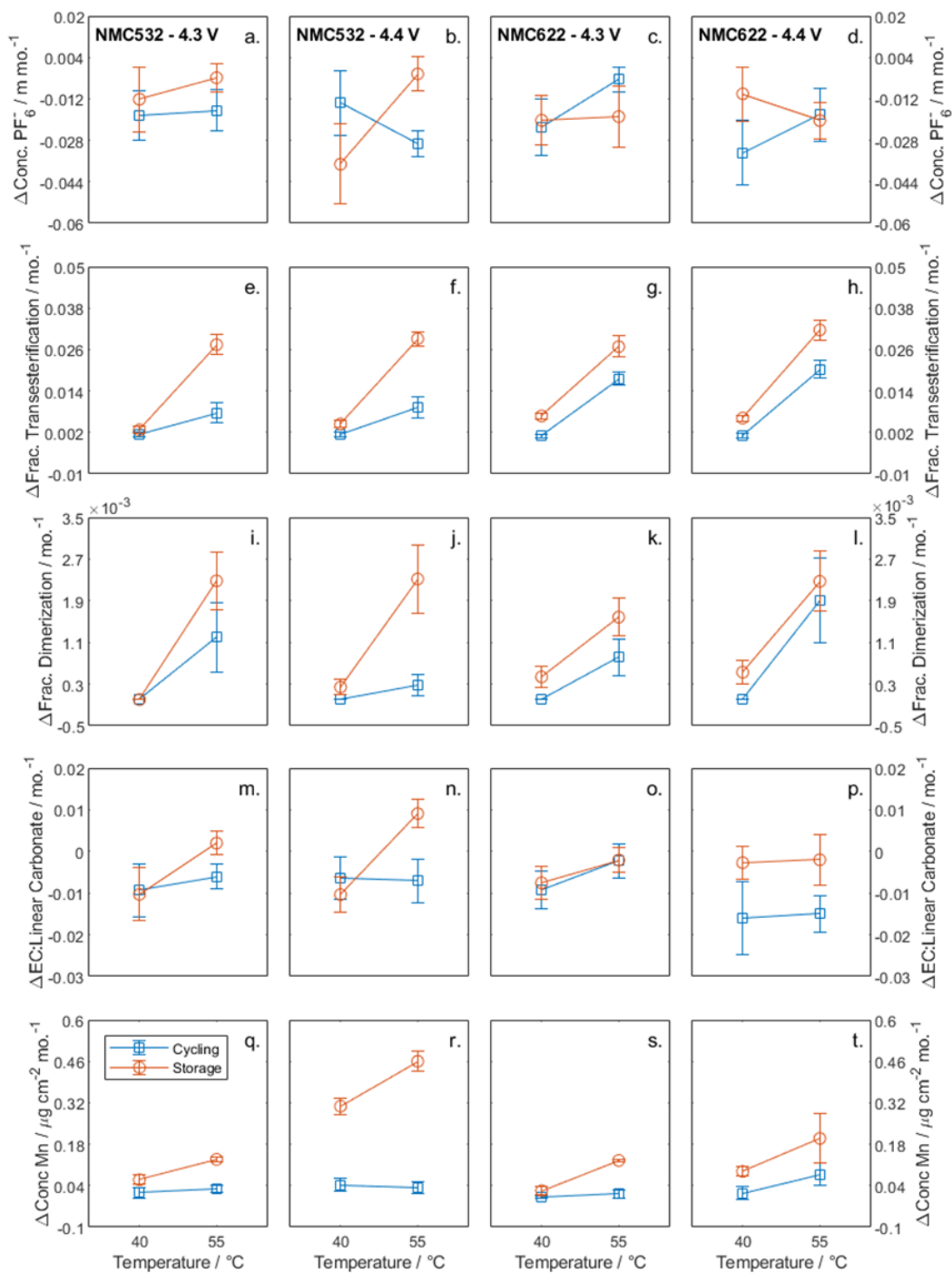


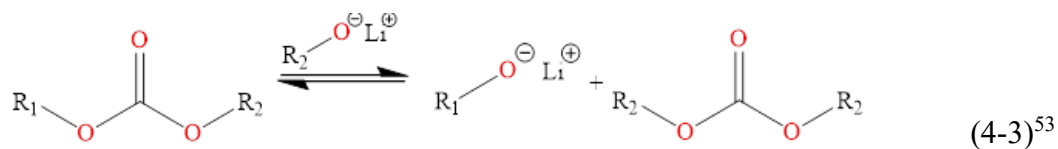
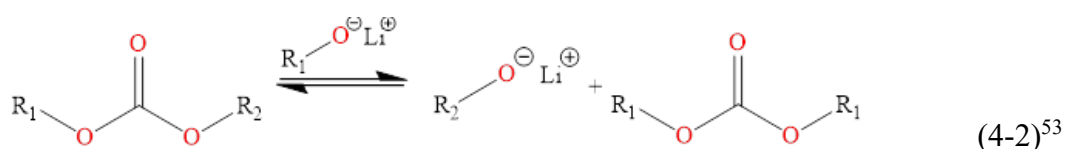
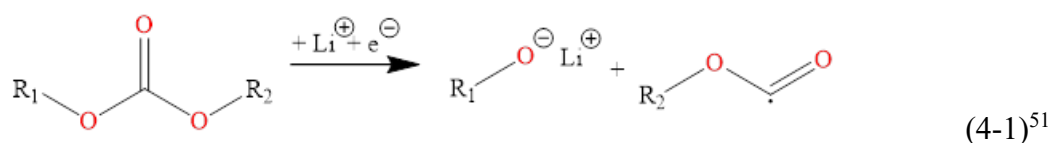
Figure 4-5 – Electrode and electrolyte analysis results for cycled and stored cells (blue squares and orange circles, respectively) are presented versus testing temperature. Panels (a.-d.) include the cell type and cycling/storage UCPs for the panels that follow below. Panels (a.-d.) show the change in PF₆⁻ concentration in the electrolyte per month. Panels (e.-h.) show the rate of transesterification and panels (i.-l.) show the rate of dimerization. Panels (m.-p.) show the change in EC:linear carbonate ratio of electrolyte per month. Panels (q.-t.) show the change in Mn loading on the negative electrode per month.

cycling and stored cells. However, following the initial increase in PF_6^- concentration after cell formation (to ~ 1.3 m), all conditions appear to result in slightly negative changes in PF_6^- concentration. The observed changes are like those of the initial cells and are consistent with previous trends in electrolyte salt concentrations where the salt concentrations increase after formation from about 1.1 m to 1.25 m (due to consumption of solvent) then gradually decrease over time.⁷⁷ Solely considering the range of salt concentrations measured during this study, the electrolyte conductivity is not expected to change dramatically.³²

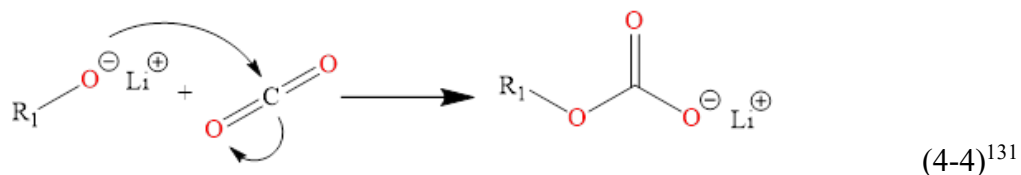
Figures 4-5(e. and f.) show the change to fraction of transesterification per month in NMC532 cells (fraction of DMC and DEC created compared to the total linear carbonates, calculated as the quotient (mol. DEC + mol. DMC)/(mol. DEC + mol. DMC + mol. EMC)) measured via GC-MS. Cells cycled or stored at 40 °C experience minimal conversion of EMC to DEC and DMC for both upper cutoff potentials. Cells cycled at 55 °C show an increased rate of transesterification to $\sim 0.15 \pm 0.05$ after 12 months for both upper cutoff potentials. The rate of transesterification for cycled cells is about twice at 55 °C compared to that at 40 °C. Stored cells at 55 °C show over four times the rate of transesterification compared to cycled cells at 55 °C. The rate of transesterification measured for cells tested at 55 °C are independent of upper cutoff potential. The additive VC has been shown to passivate electrodes to prevent Li-alkoxide formation via the reduction of linear carbonates, however, the presence of transesterification products suggests that Li-alkoxides could be generated later in cycling or storage lifetime, especially at 55 °C.

Equations 4-1, 4-2, and 4-3 show a proposed reaction for Li-alkoxide formation (4-1) and subsequent reactions with linear carbonates (4-2 and 4-3). Because Li-alkoxides are

regenerated in the transesterification process, any Li-alkoxides have the potential to continue converting EMC over time.¹²⁸ It has been previously reported that an EMC solution containing 1 % Li-alkoxide will reach equilibrium (~25:25:50 DEC:DMC:EMC ratio) in ~20 days at $(25 \pm 5) \text{ }^\circ\text{C}$.¹²⁹ It is possible that EMC undergoes self-conversion to DMC and DEC over time; however, no change to linear carbonate ratios were observed in a 1 litre bottle of electrolyte (1.0 M LiPF₆ in EC:DMC:DEC (1:1:1 by wt.)) stored at room temperature in a sealed aluminum can for 16+ years in Jeff Dahn's office (confirmed via Fourier-transformed infrared spectroscopy,¹³⁰ see Figure A-8 – it may also surprise some readers that the electrolyte was colorless after this 16+ year storage as well.). Rates of conversion from Figures 4-5(e. and f.) project a minimum (linear extrapolation) of ~15 months (55 C stored cells) to ~40 months (55 C cycled cells) for equilibrium to be established (~0.5 fraction of transesterification). Both rates of conversion suggest either a concentration of Li-alkoxides below 1%, a shorter residence time of Li-alkoxides, or an alternative mechanism.

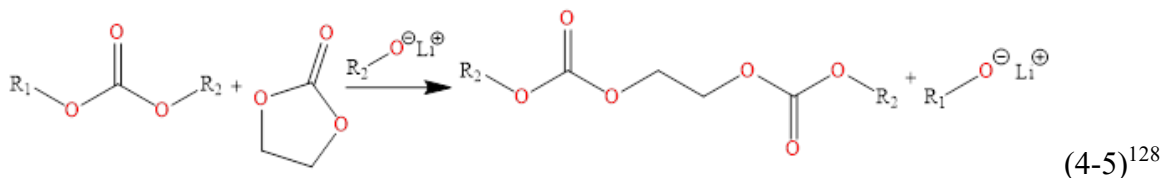


Some recent work shows CO₂ gas is beneficial to Li-ion batteries in suppressing transesterification.¹²⁰ It is likely that CO₂ produced can react with alkoxides (reported up to 2 · 10⁻² M solubility,¹²⁸ also found in small amounts in SEI) to form Li-alkyl carbonates,¹³¹ a more insoluble (found via conductivity measurements)¹³² and less reactive product than lithium alkoxides.^{74,132} This mechanism (Equations 4-4) would consume alkoxides, limit the residence time of Li-alkoxides in the electrolyte, and slow the rate of transesterification in cells. Considering this mechanism, the rate of EMC conversion would be dependent on Li-alkoxide production (electrolyte reduction) and reaction with CO₂. For cycled cells, where Li-alkoxides are expected to be produced at top of charge,^{53,64} Li-alkoxides would be produced for a limited time during each cycle while scavenging of Li-alkoxides (by CO₂) could always occur. For cells stored at top of charge, Li-alkoxide formation would occur continuously, while the rate of Li-alkoxide scavenging (via CO₂) would remain the same. This would result in a larger presence of Li-alkoxides and transesterification in stored cells, as observed. Other mechanisms that have recently been proposed to consume Li-alkoxides indicate they can be responsible for the terminating step in oligomers, oligo carbonates, phosphate-carbonates, and polyethylene glycols.^{76,86} Under these cases, LiF (thought to be beneficial to SEI layer) could be formed and polymerization chain length could be limited by the presence of Li-alkoxides. Analysis of these products was not conducted but will be considered in future work.



Equation 4-5 shows the Li-alkoxide initiated dimerization reaction between EC and a linear carbonate. Figures 4-5(i. and j.) show the rates of dimerization per month (measured by the

quotient of (mol. DMOHC + mol. DEOHC)/(mol. DMOHC + mol. DEOHC. + mol. EC) measured via GC-MS. When stored at 40 °C, cycled and stored cells show no dimerization products with a UCP of 4.3 V and only show a slight increase in rate of dimerization after



12 months with a UCP of 4.4 V. When the temperature increases to 55 °C, cycled cells still show a low rate of dimerization in cells with UCPs of 4.3 V and 4.4 V. Cells stored at UCPs of 4.3 V and 4.4 V and at 55 °C show an increase in the rate of dimerization throughout the observation period to a maximum of 5 % conversion over 12 months. The rate of dimerization is similar for cells stored at 55 °C at 4.3 V and at 4.4 V. Dimerization (Figures A-4(i. – l.) shows a similar set of trends as does transesterification (Figures A-4(e. – h.)). However, at certain times and under certain conditions, 0% dimerization is measured where transesterification is present, for example, cycled cells with both upper cutoff potentials and at both temperatures and stored cells at 40°C. This could indicate dimerization products are produced via Lewis acid assisted ring opening of EC^{133,134} rather than by the presence of Li-alkoxide.⁵¹ It is expected that small amounts of dimerization products will not hinder cell performance, however, larger concentrations could increase viscosity and decrease conductivity of the electrolyte solution and impact cell performance.⁵¹

Figures 4-5(m. and n.) show the change in EC to linear carbonate ratio per month versus temperature. For all cells, the original EC:linear carbonate mass ratio was about 0.43. Although the cell variability and linear fits prevent a more definitive conclusion to be

drawn, overall, it is clear there are no major (> 20 %) changes to the EC:linear carbonate ratio throughout 12 month period. Some results suggest the ratio of EC: linear carbonate is decreasing (negative rates measured). This could originate from EC (versus linear carbonate) reactivity. Some possible mechanisms would include reduction at the negative electrode (see Figure 2-2), EC polymerization as reported by Henschel et al. discussed in Chapter 2,⁷⁶ and EC oxidation reported by Jung et al..^{49,61} Further investigation is needed to identify the extent EC is lost over linear carbonate. This would likely require more significant changes to occur in the electrolyte. This could be achieved by allowing cells to cycle beyond 12 months or perhaps accelerating electrolyte reactivity via increase temperature study.

Figures 4-5(q. and r.) show the change in mass of Mn per unit area on the negative electrode as determined by μ XRF. The mass loadings measured for cells at 3 months were like that after formation (given in Methods section). Under all conditions, cycled cells appear to have minimal change in Mn deposition (maximum of $\sim 0.75 \mu\text{g cm}^{-2}$) after 12 months of cycling. Storage cells at 40 °C and 4.3 V UCP show minimal increase in Mn deposition over 12 months whereas, when the UCP was increased to 4.4 V, the rate of Mn deposition approximately tripled and a maximum loading of $(3.2 \pm 0.3) \mu\text{g cm}^{-2}$ was observed after 12 months (transition metal deposition errors estimated via replicate cell relative standard deviation). When the temperature was increased to 55 °C and the UCP kept at 4.3 V, the Mn deposition rate approximately doubled and a maximum loading of $(1.94 \pm 0.07) \mu\text{g cm}^{-2}$ was observed after 12 months of storage. When the UCP was also increased to 4.4 V and cells were stored at 55 °C the rate of deposition quadrupled and a loading of $(4.8 \pm 0.4) \mu\text{g cm}^{-2}$ was observed after 12 months of storage. These results indicate that time at

higher upper cutoff potential controls the degree of Mn deposition at the negative electrode while temperature has a smaller effect. Still, these cells only show a maximum Mn loading of $\sim 5 \mu\text{g cm}^{-2}$, corresponding to $< 0.16\%$ of the Mn in the positive electrode material. This is substantially smaller than the degree of dissolution measured by Gilbert et al.⁷⁸ (no electrolyte additives in their cells) and is consistent with our previous work (cells contained electrolyte additives).⁷⁷

Figures 4-5(c. and d.) show the change in PF_6^- concentration for NMC622 cells. These errors are not small enough to statistically distinguish between measured concentrations as a function of time or across various conditions. Still, the measured concentrations are within 20% of the original salt concentration. Of the concentrations measured (Figure A-5(a. – d.)), the slight increase in PF_6^- concentration to $\sim 1.25 \text{ m}$ at 3 months is consistent with previous studies showing a drop in solvent concentration after formation.⁷⁷ This was followed by a gradual decrease in salt concentration throughout cell storage/cycling to $\sim 0.9\text{-}1.0 \text{ m}$ after 12 months. Overall, there are no extreme, measurable, changes to salt concentration. Additionally, the changes are unlikely to change ionic conductivity by more than 20 %.³²

Figures 4-5(g. and h.) show the rate of transesterification measured via GC-MS. Cells cycled at 40°C show minimal rates of transesterification. Cells stored at 40°C show an increase in the rate of transesterification (maximum of ~ 0.1 during 12-month observation period). Cells cycled at 55°C show an increase in rate of transesterification to a maximum of ~ 0.2 after 9 months. Cells stored at 55°C show higher rates of transesterification to a maximum of ~ 0.3 over 9 months. Under most conditions, it is possible to observe higher fractions of transesterification for stored cells versus cycled cells as was the case for the

NMC532 cells. There is little observable difference between extents of transesterification measured in cells at an UCP of 4.3 V versus 4.4 V, as was the case for the NMC532 cells. As discussed above, even the highest rates of EMC conversion in these cells at 55 °C are small compared to EMC conversion in an electrolyte containing 1% Li-alkoxide at 25 °C.¹²⁹

Figures 4-5(k. and l.) show the rate of dimerization versus temperature in cycled and stored cells. When stored at 40 °C, cycled and stored cells show minimal increase in dimerization after 12 months (0 % at 3 months to < ~2.3 % after 12 months). For all cells, the extent of dimerization remains low (below ~ 5 % during study), as was the case for NMC532 cells. There is minimal measurable difference in the rate of dimerization between both upper cutoff potentials and between cycling versus storage cells.

Figures 4-5(o. and p.) show the change in EC to linear carbonate ratio for NMC622 cells versus temperature. For all cells, the original EC:linear carbonate ratio was about 0.43. For all conditions, minimal change to ratios were measured. The initial increase in EC:linear carbonate ratio observed in 3-month cells (Figures A-5(m. – p.)) is expected due to consumption of linear carbonate during initial formation cycles. Subsequently, although there is large replicate cell variability, a negative change in EC to linear carbonate ratio could be observed, especially in cells cycled to 4.4 V. This would suggest higher stoichiometric rates of EC consumption than linear carbonate consumption since formation. Some cells show elevated EC:linear carbonate ratios (also associated with elevated PF₆⁻ concentration), suggesting significant linear carbonate consumption and/or solvent loss in cells.

Figures 4-5(s. and t.) show the rate of change in mass of Mn per unit area of negative electrode for NMC622 cells determined by μ XRF. The loading measured for cells at 3 months is similar to that seen after formation ($(0.24 \pm 0.01) \mu\text{g cm}^{-2}$ and $(0.24 \pm 0.01) \mu\text{g cm}^{-2}$ for UCPs of 4.3 V and 4.4 V, respectively) (see Methods section). All cycled cells show slight increases in Mn loading ($(0.78 \pm 0.07) \mu\text{g cm}^{-2}$) after 12 months of cycling. Storage cells at 40 °C and a 4.3 V UCP also show little change in Mn loading on the negative electrode, $(0.65 \pm 0.01) \mu\text{g cm}^{-2}$ after 12 months (comparable to cycled cells), whereas when the upper cutoff potential is increased to 4.4 V the rate of Mn deposition approximately doubles to yield a maximum loading of $(1.4 \pm 0.2) \mu\text{g cm}^{-2}$ after 12 months. When the storage temperature is increased to 55 °C and UCP held at 4.3 V, the Mn deposition rate approximately doubles to yield a maximum loading of $(1.25 \pm 0.08) \mu\text{g cm}^{-2}$ after 9 months of storage. When the UCP is also increased to 4.4 V and cells are stored at 55 °C the rate of Mn deposition quadruples to yield a loading of $(2.00 \pm 0.04) \mu\text{g cm}^{-2}$ after the 9 months storage. NMC532 cells also showed more Mn on the negative electrode for stored cells compared to cycled cells. These Mn concentrations indicate that time at higher upper cutoff potential contributes to the degree of Mn deposition at the negative electrode while temperature has a smaller effect. Still, NMC622 cells show a maximum Mn deposition of $\sim 2 \mu\text{g cm}^{-2}$ corresponding to $< 0.07\%$ of the Mn in the positive electrode material. This is substantially smaller compared to the degree of dissolution measured by Gilbert et al. (no electrolyte additives in their cells).⁷⁸

Notable differences in measured electrolyte properties between NMC532 and NMC622 cells include transesterification in cycled cells at 55 °C. Where cycled NMC532 cells had low fractions of transesterification, NMC622 cells at 55 °C showed elevated fractions,

more comparable to stored cells. Differences between PF_6^- concentration, fractions of dimerization, and EC:linear carbonate ratio results are not deemed significant between NMC532 and NMC622 cells.

DTA Results

The DTA analysis conducted here depends on DTA work done on two sets of previously constructed reference cells. Results from these cells are shown in Figures 4-6(a. and b.). These show the DTA curve of 1.0 M LiPF_6 in 3:7 EC:EMC, and a set of curves as the EC content is increased (Figure 4-6a.), and a set of curves as the LiPF_6 concentration is increased (Figure 4-6b.). Figures 4-6(c. and d.) then show the effect of the change in EC and LiPF_6 concentration on the liquidus temperature, as determined from experiment. This shows that the LiPF_6 content affects the liquidus temperature linearly, while the EC content affects it in a way that has been effectively modelled with a second order polynomial. While these trends have been measured experimentally in these limited ranges, this work will assume that they will roughly hold for nearby concentrations. Particularly, the cells used here used an initial concentration of 1.1 m LiPF_6 , which is just outside of the experimentally studied range of LiPF_6 concentrations.

All NMC532 and NMC622 cells in the matrix were tested via DTA, per the method described in the Methods section of this work. The resultant data shows that, as per Figure 4-7, the DTA curves of the cells cycled or stored at 40 °C, and particularly the NMC532 cells, did not change significantly through the testing period. This is the case for all the 40 °C cells, as shown in Figure A-9. However, DTA tests on the 55 °C cells show that there

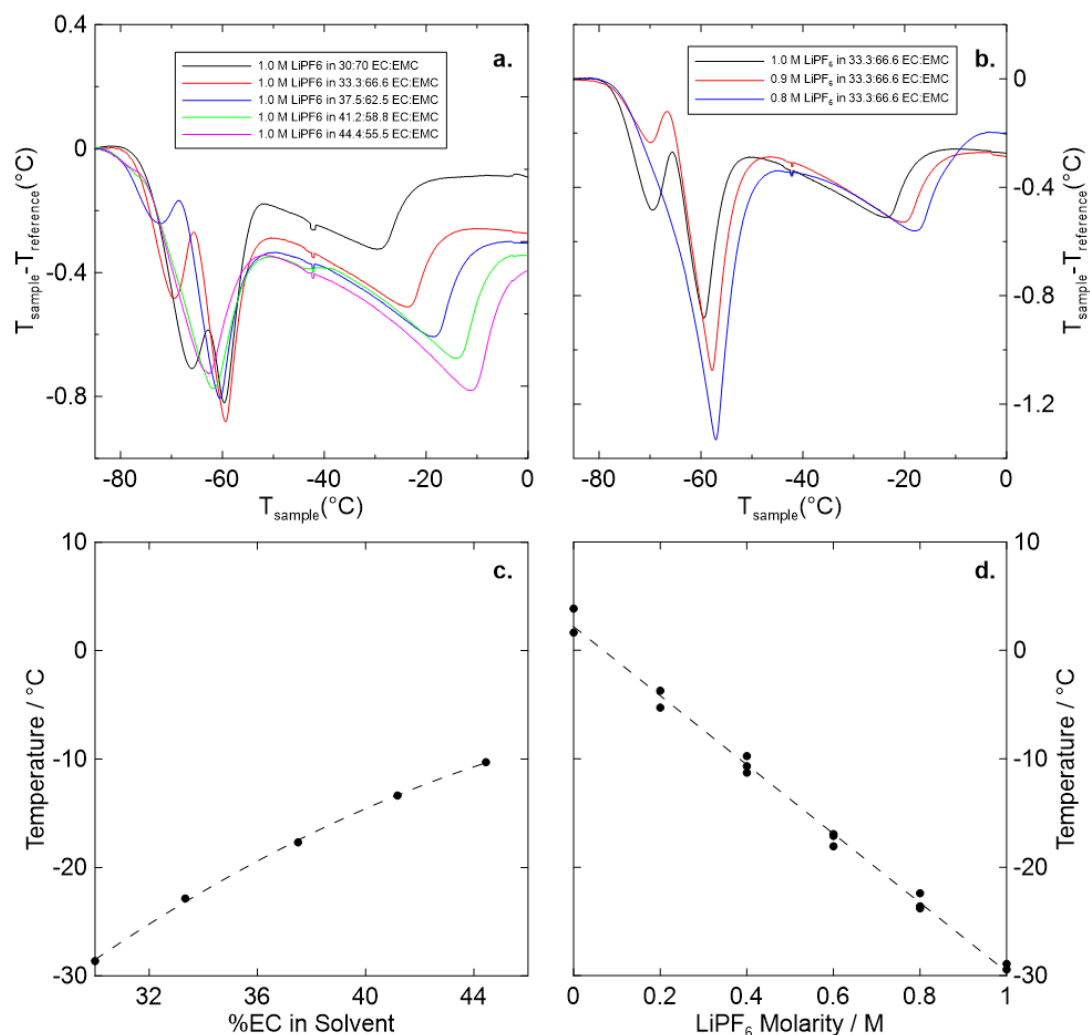


Figure 4-6 – Summary of effects of modification of electrolyte composition on 1.0 M LiPF_6 in 3:7 EC:EMC, as studied via DTA. Panels (a. and b.) show the effect of varying EC ratio and LiPF_6 content, respectively, on the DTA signal of a cell. Panels (c. and d.) show the relationships between the change in EC ratio and salt concentration on the liquidus temperature, respectively. Figure produced by M. Bauer for publication in *J. Electrochem Soc.* 168, 020532 (2021). Reproduced with permission (see Appendix C).

are significant changes in the electrolyte state, and there is considerable transesterification at longer cell lifetimes, as shown in Figure 4-8. This agrees with the results obtained by GC-MS and NMR, as shown in the other portions of this work.

As discussed above, NMR and GC-MS results show salt consumption and solvent composition changes over the observation period for cells tested at 40 °C. However, Figure 4-7 shows virtually no changes to the DTA signal and virtually no change to the liquidus temperature, suggesting no changes to the electrolyte. This apparent contradiction puzzled us until we realized that decreasing the EC content (as observed in Figure 4-5) drives the liquidus temperature down, while decreasing the LiPF₆ concentration (see Figure 4-5) drives it up, as shown by Figures 4-6(a. and b.). Figure 4-9 and Figure 4-10 show that the changes in the electrolyte composition (as measured in Figure 4-5) effectively counteract using the data from Figures 4-6(c. and d.). Thus, for the changes in the electrolyte which occur in the cells tested at 40 °C, one expects the liquidus temperature to remain nearly constant as is observed. This shows that the liquidus temperature cannot, by itself, be used to probe the state of the electrolyte in the 40 °C tested cells.

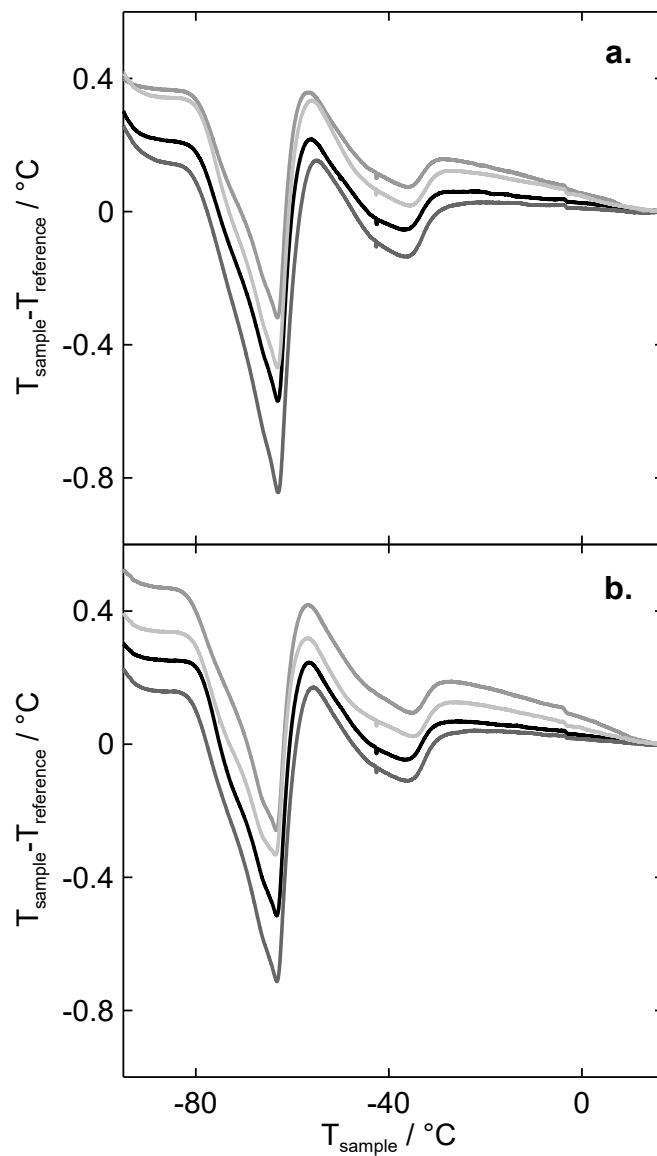


Figure 4-7 – Results from DTA of NMC532 cells tested at 40 °C to an upper cutoff of 4.3 V. Panel (a.) shows data from cycled cells and panel (b.) shows data from stored cells. Time of testing is represented by line color, ranging from 3 to 12 months (black to grey, respectively). Figure produced by M. Bauer for *J. Electrochem Soc.* 168, 020532 (2021) publication.

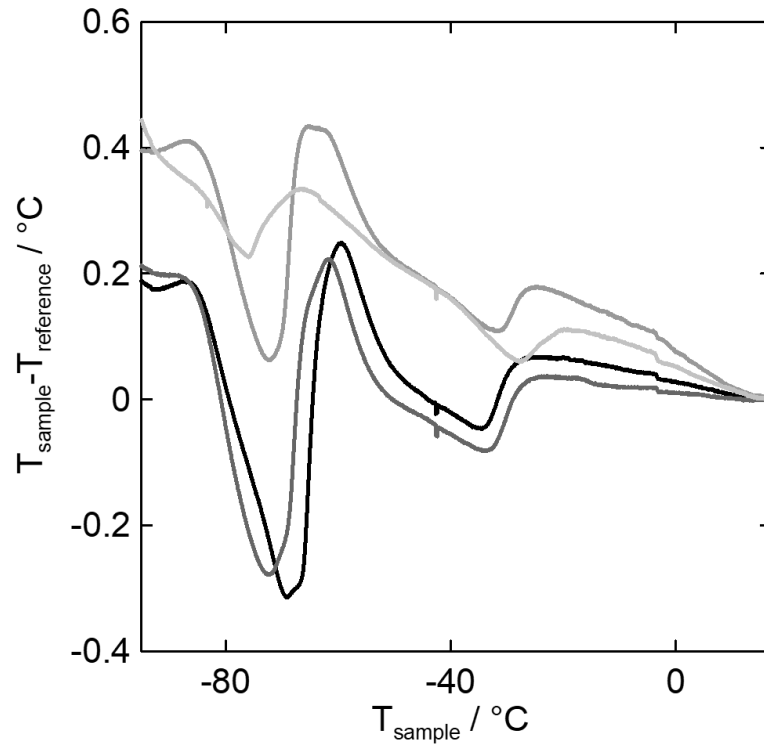


Figure 4-8 – Results from DTA of NMC532 cells stored at 55 $^{\circ}\text{C}$ at an upper cutoff of 4.4 V. Time of testing is represented by line color, ranging from 3 to 12 months (black to grey, respectively). Note that these cells showed increasing fractions of transesterification (See Figure 4-5) with testing time and the conversion of EMC to DEC and DMC is responsible for the changes to the electrolyte phase diagram as reflected in the DTA signal. Figure produced by M. Bauer for publication in *J. Electrochem Soc.* 168, 020532 (2021).

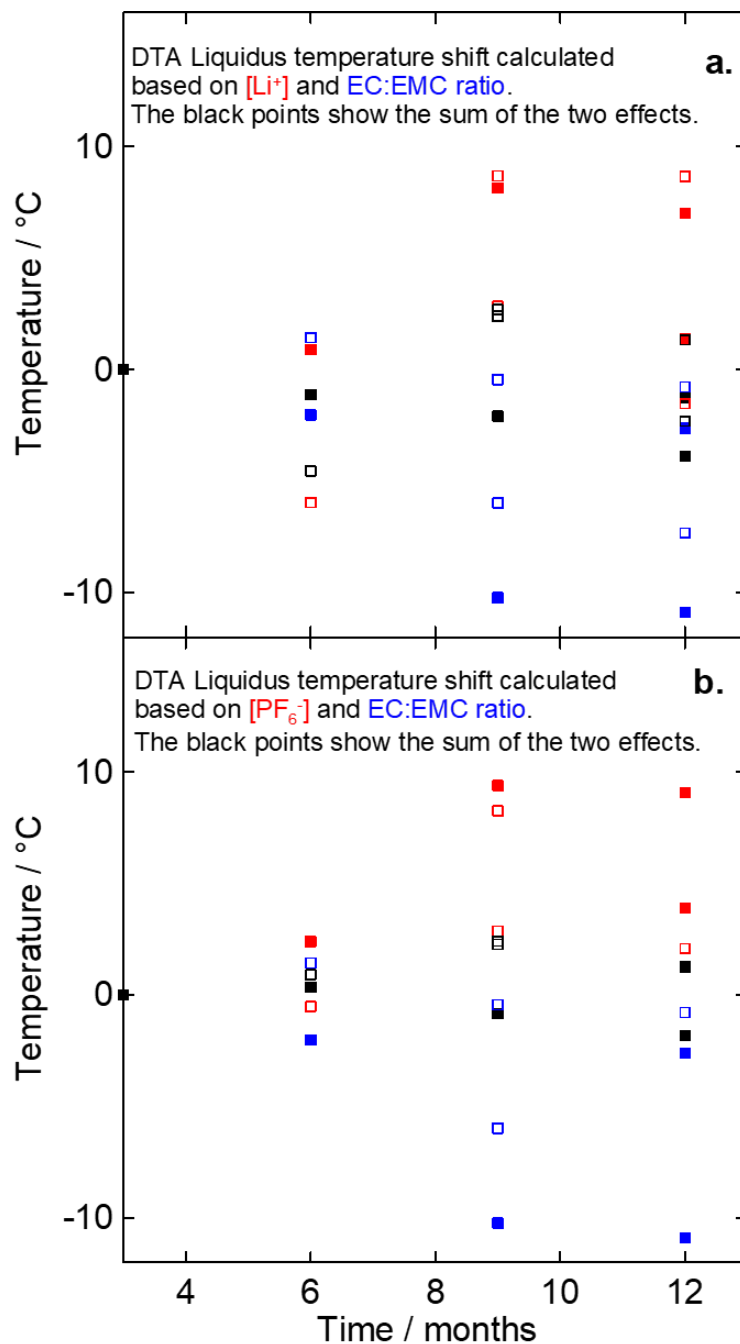


Figure 4-9 – The effect on the liquidus temperature of the change in EC content (blue squares) and Li⁺ concentration (a.) and PF₆⁻ concentration (b.) in NMC532 cells tested to an upper cutoff of 4.3 V at 40 °C, according to data in Figure 4-5 and the DTA results shown in Figure 4-8. The combination of these effects (black squares) is shown to be near zero in both storage (empty squares) and cycling (filled squares) cells. This figure was produced by M. Bauer for publication in *J. Electrochem Soc.* 168, 020532 (2021).

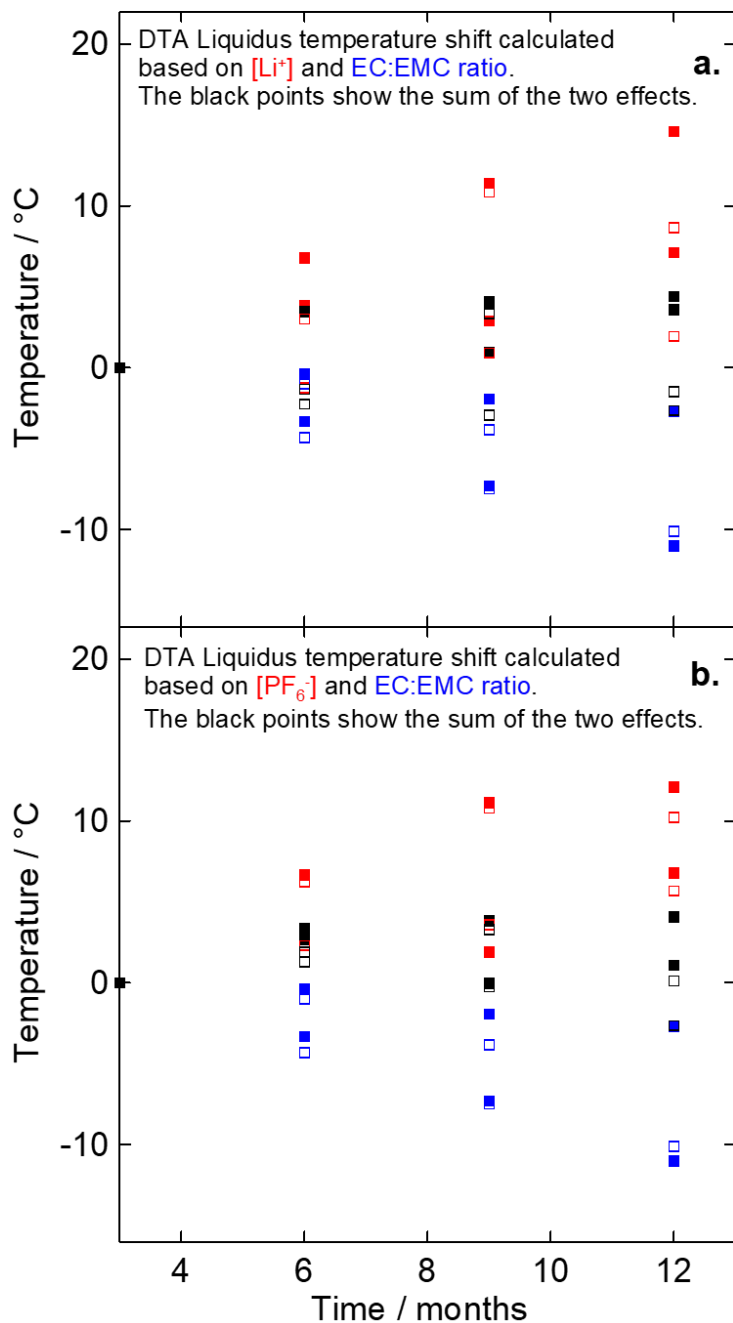


Figure 4-10 – The effect on the liquidus temperature of the change in EC content (blue squares) and Li⁺ concentration (a.) and PF₆⁻ concentration (b.) (red squares) in NMC622 cells tested to an upper cutoff of 4.3 V at 40 °C, according to data in Figure 4-5 and the DTA results shown in Figure 4-7. The combination of these effects (black squares) is shown to be near zero in both storage (empty squares) and cycling (filled squares) cells. This figure was produced by M. Bauer for publication in *J. Electrochem Soc.* 168, 020532 (2021).

Transesterification and Gas Production

Figure 4-11 shows the fraction of transesterification plotted versus gas production for cycled and stored NMC532 cells. Markers, fill colors and conditions are consistent with Figure 4-2. Figures 4-11(a. and b.) show that at 55 °C, as the measured gas increases, the fraction of transesterification also increases. The relationship between gas production and transesterification appears linear for cycling and storage and for both upper cutoff potentials. When considering the test protocol at 55 °C, it is possible to observe a slightly lower fraction of transesterification to gas volume ratio in stored cells versus cycled cells. At 40 °C, Figures 4-11(c. and d.) show too little gas production and too little transesterification to identify a linear relation.

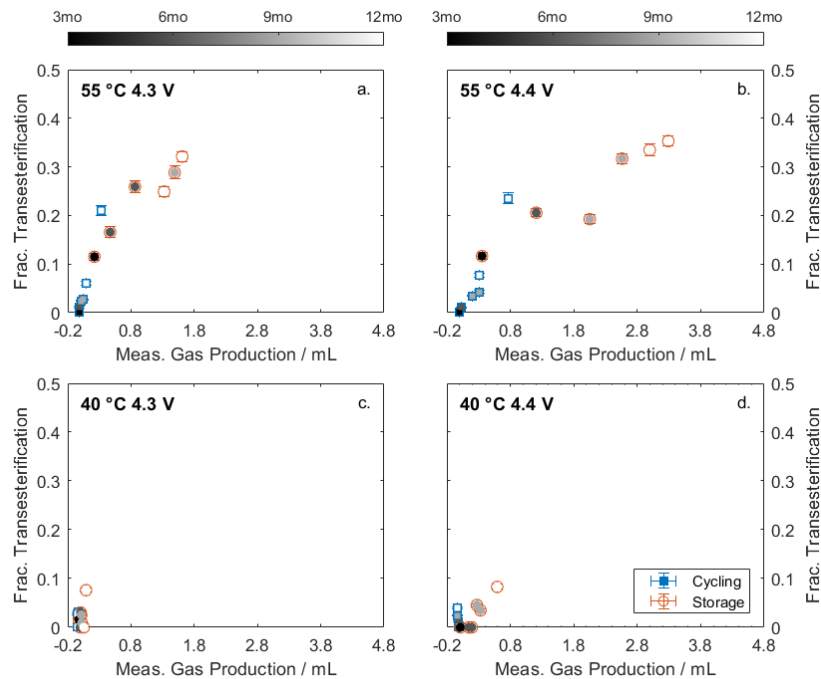


Figure 4-11 – The fraction of transesterification is shown versus measured gas produced in NMC532 cycled (blue squares) and stored cells (orange circles). Time of cycling/storage is represented in the fill color ranging from black to white (3 mo. and 12 mo., respectively). Cycling/storage conditions are shown in the top left of each graph.

Figure 4-12 shows the fraction of transesterification versus gas production for NMC622 cells. Markers, fill color, condition and scales are consistent with Figure 4-11 for ease of comparison. Cycled and stored cells at 55 °C show increased fractions of transesterification with increased gas production in most cases. As mentioned in previous sections, gas production of about 3 mL is close to maximum volume measurable by the Archimedes method. Like NMC532, cycled cells at 4.3 V UCP show a slightly lower ratio than stored cells. Cycled cells at 55 °C and with 4.4 V UCP appear to have a lower ratio than stored cells. For cells at 40 °C (Figures 4-12(c. and d.)), minimal transesterification and gas production inhibit drawing correlations between transesterification and gas production.

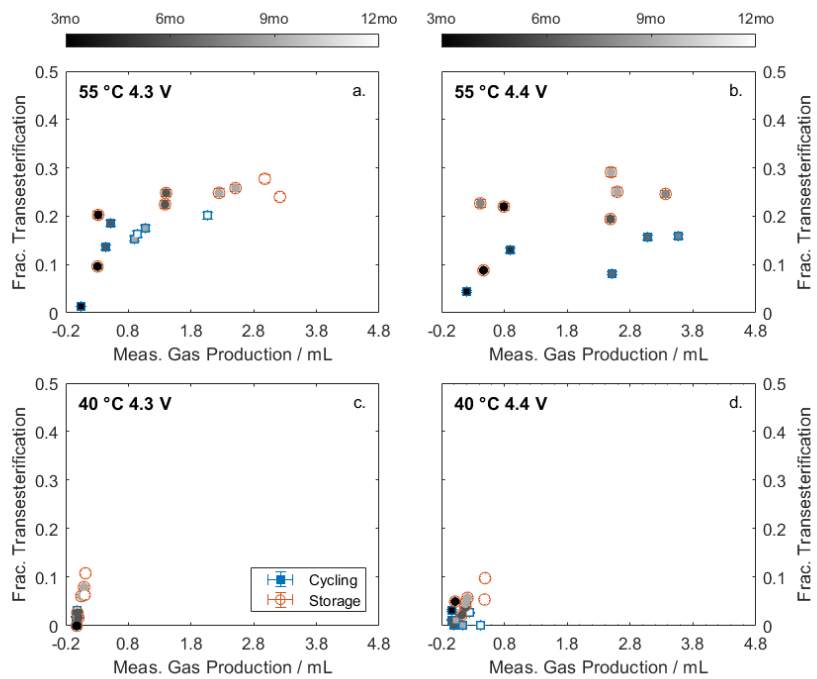


Figure 4-12 – The fraction of transesterification is shown versus measured gas produced in NMC622 cycled (blue squares) and stored cells (orange circles). Time of cycling/storage is represented in the fill color ranging from black to white (3 mo. and 12 mo., respectively). Cycling/storage conditions are shown in the top left of each graph.

Both NMC532 and NMC622 cells appear to have a similar transesterification to gas production ratios at 55 °C, except for ratios measured for NMC622 cells with 4.4 V UCP. While transesterification, facilitated by linear carbonate derived Li-alkoxides, is expected to be accompanied by gas formation (likely CO via linear carbonate reduction),⁵³ the extent of this relationship is not well known.^{52,68,120} Recent work has shown that CO₂ can react with alkoxides to form an insoluble, less reactive product.^{74,120} This reaction would remove CO₂ and decrease the gas volume. Additional quantitative work (electrolyte and gas composition analysis) is necessary to identify the gases in these cells and to uncover the extent of this CO₂ removal.

Transition Metal Ratio on Neg. Electrode

Figure 4-13 and Figure 4-14 show the loading of Ni versus the loading of Mn found on the negative electrode for NMC532 and NMC622 cells, respectively. Markers, fill colors and conditions match those of Figure 4-11. Scales are consistent between Figure 4-13 and Figure 4-14 and solid lines represent the expected mass ratio of Ni:Mn based on the positive electrode composition.

Figures 4-13(a. and b.) show that both cycled and stored cells at 55 °C have less Ni deposition at the negative electrode than expected based on the positive electrode composition. Cycled and stored cells show that the ratio of Ni:Mn deposition is roughly constant for each condition. Cells with an UCP of 4.4 V show higher Mn loadings throughout the observation period. Cells at 40 °C, shown in Figures 4-13(c. and d.), appear to show closer agreement with expected Ni:Mn ratio, yet, still show a lower Ni:Mn ratio

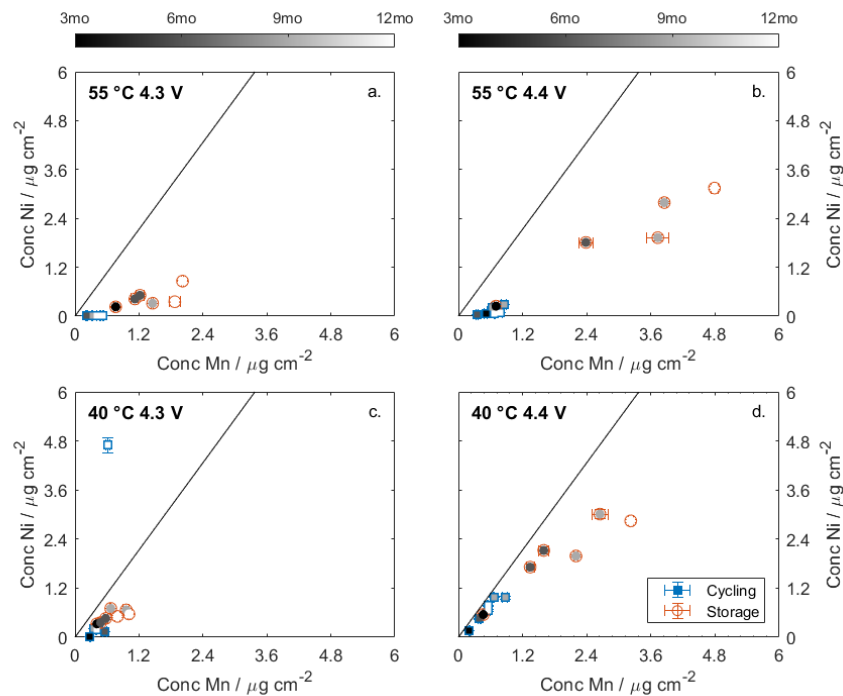


Figure 4-13 – The concentration of Ni is shown versus concentration of Mn measured on the negative electrode of NMC532 cycled (blue squares) and stored cells (orange circles). Time of cycling/storage is represented in the fill color ranging from black to white (3 mo. and 12 mo., respectively). Cycling/storage conditions are shown in the top left of each graph.

than expected. The ratio for cells at 40 °C appears consistent with the two upper cutoff potentials and with cycled versus stored cells. Additionally, cells measured after formation showed low concentrations of Mn (and Co) on the negative electrode as discussed above, however, no Ni deposition was measured after formation.

The decreased Ni:Mn ratio indicates the dissolution, solvation, and deposition processes favor Mn over Ni. Recent studies have shown that these transition metal can dissolve in different relative concentrations depending on the dissolution mechanism. For example, Sahore et al. found that Ni was primarily dissolved via chemical decomposition and/or via presence of F^- or PF_6^- and Mn and Co were primarily dissolved from charged electrodes

via electrochemical oxidative decomposition of the electrolyte and solvated via metal complex formation.⁸² Sahore et al. also hypothesized that chemical (versus electrochemical) oxidation via O^{2-} loss⁴⁹ is more likely to involve surface transition metal dissolution and lithium insertion in the electrode whereas electrochemical oxidation⁴⁹ is more likely to keep transition metals in the positive electrode but require lithium insertion to maintain charge balance. The former scenario would allow transition metal to replace Li^+ and could lead to a lower Li^+ concentration and more transition metal dissolution. The latter oxidation mechanism would preserve Li^+ concentration and result in less transition metal dissolution. This was observed in cells at 55 °C where the extent of Ni deposition is less than expected. The higher Mn concentration relative to Ni concentration was also observed by Sahore et al. in cells where electrochemical oxidation was presumed.⁸²

Figure 4-14 shows results for NM622 cells. At 55 °C, as shown in Figures 4-14(a. and b.), the Ni:Mn ratio is lower than expected. Cycled versus stored cells appear to have different mass ratios and extents of deposition. Results at 40 °C, Figures 4-14(c. and d.), show that cycled cells have good agreement with the expected ratios. Stored cells at 40 °C show better agreement than cells at 55 °C, but the ratio remains slightly lower than expected. The results from NMC532 and NMC622 cells, considering this mechanism, suggest there is more electrochemical oxidation occurring at elevated temperature.

Figure 4-15 and Figure 4-16 show the Co concentration versus Mn concentration on the negative electrodes of NMC532 and NMC622 cells, respectively. Markers, fill colors, and conditions are consistent with previous figures such as Figure 4-11. The solid line plotted displays the expected Co:Mn mass ratio based on positive electrode content. Figures 4-15

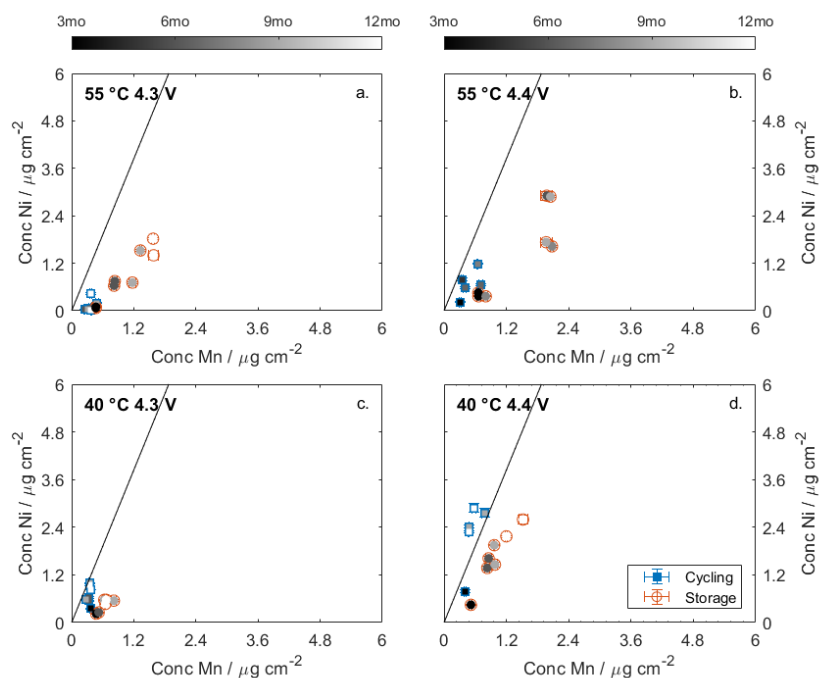


Figure 4-14 – The concentration of Ni is shown versus concentration of Mn measured on the negative electrode of NMC622 cycled (blue squares) and stored cells (orange circles). Time of cycling/storage is represented in the fill color ranging from black to white (3 mo. and 12 mo., respectively). Cycling/storage conditions are shown in the top left of each graph.

(a. and b.) show that the Co:Mn ratio for cycled and stored NMC532 cells at 55 °C agree with the expected ratio. Figures 4-15(c. and d.) also show that the Co:Mn ratio for stored NMC532 cells agree with the expected ratio at 40 °C. Some stored cells at 40 °C show slightly lower Co:Mn ratio than expected for older cells. Figures 4-16(a. and b.) show the Co:Mn ratios measured in NMC622 cells mostly agree with the expected ratio, apart from older, stored cells. In this case, older, stored cells at 55 °C show slightly higher Co:Mn ratios. Figures 4-16(c. and d.) show that transition metal loadings measured in NMC622 cells at 40 °C show good agreement with the expected Co:Mn ratios.

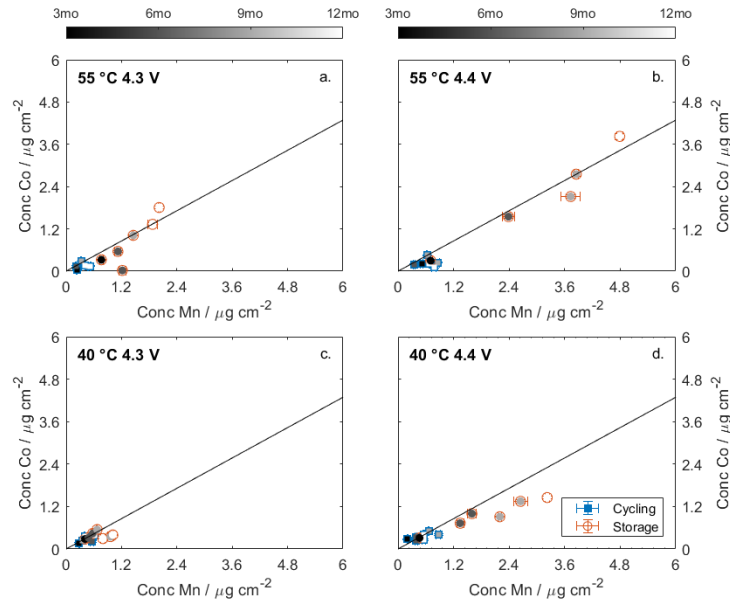


Figure 4-15 – The concentration of Co is shown versus concentration of Mn measured on the negative electrode of NMC532 cycled (blue squares) and stored cells (orange circles). Time of cycling/storage is represented in the fill color ranging from black to white (3 mo. and 12 mo., respectively). Cycling/storage conditions are shown in the top left of each graph.

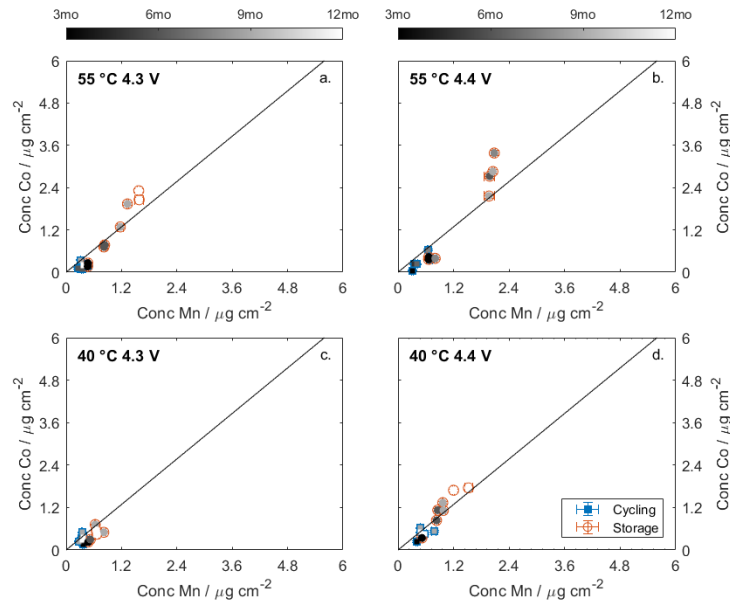


Figure 4-16 – The concentration of Co is shown versus concentration of Mn measured on the negative electrode of NMC622 cycled (blue squares) and stored cells (orange circles). Time of cycling/storage is represented in the fill color ranging from black to white (3 mo. and 12 mo., respectively). Cycling/storage conditions are shown in the top left of each graph.

Supplementary Figure A-10 and Figure A-11 show the relationship between Mn deposition at the negative electrode versus gas production in cells. Here, increases in Mn deposition correspond with increases in gas production in NMC532 cells and somewhat in NM622 cells. While many mechanisms can evolve gas in cells,^{27,28} to evaluate the effect of transition metal deposition and gas production, the total moles of transition metals deposited on the negative electrode were calculated and compared to the total moles of gas produced. Figure 4-17 and Figure 4-18 show these results for NMC532 and NMC622 cells, respectively. Markers, fill color, and conditions match previous figures (as in Figure 4-11). Plotted solid, dotted, and dashed lines provide guides to determine the mole ratio of gas: transition metal (1:1, 10:1, and 100:1, respectively).

Figures 4-17(a. and b.) show moles of gas versus moles of transition metal at the negative electrode for cycled and stored NMC532 cells at 55 °C. Cells cycled or stored to 4.4 V (Figure 4-17b.) appear to produce about 10 moles of gas for every 1 mole of transition metal transferred to the negative electrode. Most cells cycled and early cells stored at 55 °C and to 4.3 V UCP show agreement with 10:1 ratio, however, older (9 and 12 month) cells show slightly higher gas to transition metal ratio. Figures 4-17(c. and d.) show gas production to transition metal dissolution for cells at 40 °C. Cycled and stored cells with both upper cutoff potentials appear to correspond with a gas to transition metal mole ratio of 1:1. Cells at 40 °C also showed minimal transesterification (Figure 4-11), so it could be that, for these cells, the gas generation is dominated by transition metal dissolution rather than electrolyte reduction. This reaction could involve decarboxylation during transition metal-complex formation (1:1 transition metal to CO₂ gas ratio)¹³⁵ or transition metal reacting with EC to form transition metal-(CO₃)_n and C₂H₄ (also 1:1 ratio).¹³⁶ Whereas for

cells at 55 °C gas production originates predominantly from electrolyte reduction and subsequent reactions.

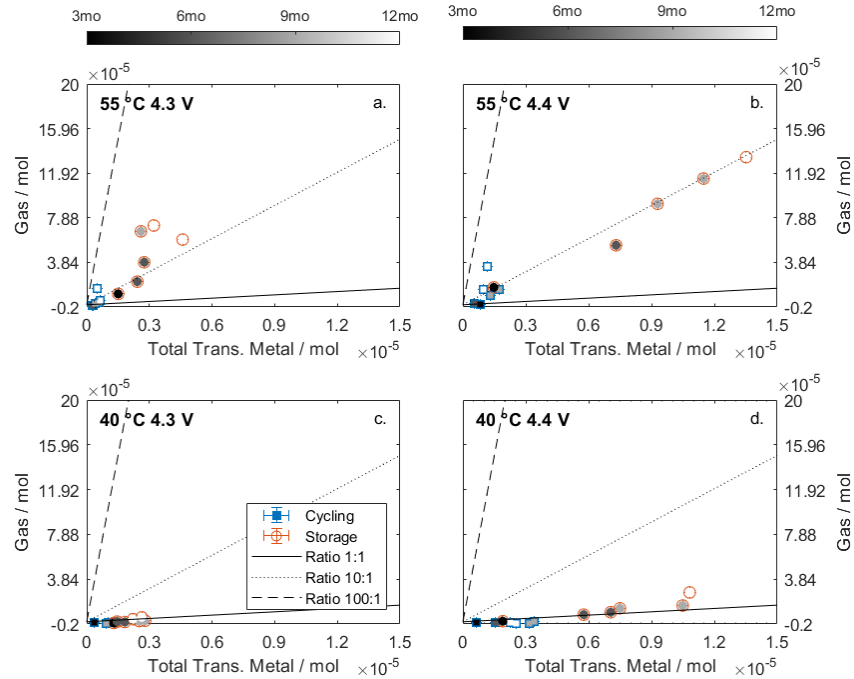


Figure 4-17 – Moles of gas measured shown versus calculated total moles of transition metals on NMC532 negative electrode. Cycled (blue squares) and stored cells (orange circles) are shown with fill color (ranging from black to white) representing the time of cycling/storage (3 mo. and 12 mo., respectively). Cycling/storage conditions are shown in the top left of each graph.

Figure 4-18a. shows the moles of gas produced versus moles of transition metals on the negative electrode for NMC622 cells with UCP 4.3 V at 55 °C. Cycled cells at this temperature follow a gas to transition metal ratio of ~100:1, whereas stored cells show a lower ratio of about ~25:1. Cells cycled and stored to 4.4 V UCP and 55 °C (Figure 18b.) show cycled cells have a gas to transition metal ratio higher ~40:1 and stored cells have slightly lower ratio (~ 20:1). Figures 4-18(c. and d.) show the moles of gas versus the

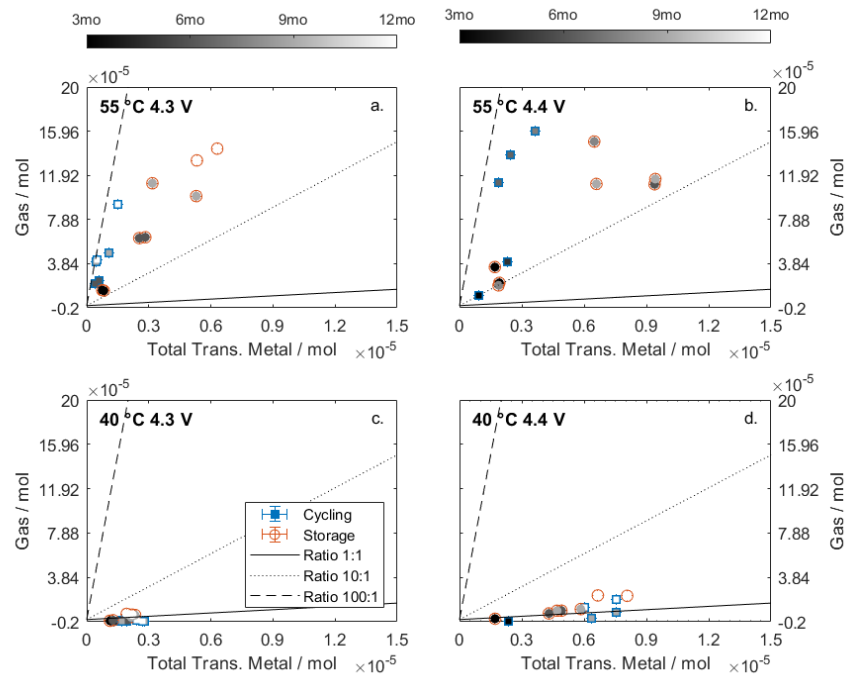


Figure 4-18 – Moles of gas measured shown versus calculated total moles of transition metals on NMC622 negative electrode. Cycled (blue squares) and stored cells (orange circles) are shown with fill color (ranging from black to white) representing the time of cycling/storage (3 mo. and 12 mo., respectively). Cycling/storage conditions are shown in the top left of each graph.

transition metal deposition for cells cycled and stored at 40 °C. Cycled and stored cells at both upper cutoff potentials show gas to transition metal ratios are closest to 1:1.

NMC532 and NMC622 cells at 40 °C show similar gas to transition metal mole ratios (1:1) for both cycled and stored cells and both upper cutoff potentials. When the temperature is increased to 55 °C, the gas to transition metal ratio for NMC532 cycled and stored cells is closest to 10:1, whereas the mol ratio for NMC622 cells appear larger. Additionally, NMC532 cells show consistent ratios for cycled and stored cells within each condition, however, NMC622 cells at 55 °C show different ratios for cycled and stored cells.

Summary

The numerous results presented in this chapter can be summarized by the following findings:

- Under selected conditions (cycling, 40 °C) electrolytes had minimal changes, even at increased upper cutoff potentials. This indicates that under some conditions, cells can operate at higher potentials without penalty, thus increasing their energy density.
- The main capacity loss mechanism for the single crystal NMC532 cells was lithium inventory loss. The dV/dQ analysis results are consistent with no active mass loss at either electrode.
- Capacity loss for the polycrystalline NMC622 cells was caused by lithium inventory loss while positive electrode mass loss also occurred.
- Gas generation increased throughout cycling and increased for cells at higher temperature or with higher upper cutoff potential. In general, gas generation was larger for stored cells.
- There were no dramatic changes to charge transfer resistance throughout observation period.
- Salt concentration increased slightly after early cycling then gradually decreased over 12 months for all conditions.
- Fraction of transesterification increased when temperature increased and was larger for stored cells. Rate of conversion suggests alkoxides are quickly consumed.
- EC:linear carbonate ratio increased slightly after early cycling then decreased as cycling/storage continued.

- DTA measurements alone are not able to detect small differences in salt and solvent concentrations due to the cancelling effect of salt content and EC:linear carbonate ratio on DTA signals. However, DTA can easily detect transesterification which occurred in the cells tested at 55 °C.
- Transition metal deposition increased more when the upper cutoff potential increased from 4.3 V to 4.4 V than when temperature increased from 40 °C to 55 °C.
- The ratio of Ni:Mn:Co on the negative electrode reveals the extent of Ni deposition was less than expected, indicating dissolution, solvation, and deposition processes differ for different transition metals.
- Transition metal dissolution remained small (< 0.15% of the transition metals in the positive electrode) and was a tiny fraction of the positive electrode mass loss determined by dV/dQ for NMC622 cells.
- Many products/reactants (such as fraction of transesterification, gas production, transition metal dissolution) appear to have a constant rate of increase in this 12-month observation period. In most cases, results for cells from 3 to 6 months could be used to reasonably estimate the changes at 12 months. Extrapolations beyond 12 months are not able to be made with certainty, as important factors such as solvent volume remaining and approaching reaction equilibria, will have limits. Future work by others should consider cells aged beyond 12 months.

Findings from this study also indicate gas formation at 55 °C is more likely dependent on parasitic reactions such as electrolyte reduction and oxidation rather than induced by transition metal dissolution and deposition. At 40 °C, the ratio of moles of gas produced and moles of transition metals deposited on the negative electrode was found to be in an

approximate 1:1 ratio for all cells. This suggests that ligands associated with transition metal coordination complexes are formed during dissolution or reduced at the negative electrode. However, further work is necessary to determine the composition of these gases and their origin.

CHAPTER 5 – HIGH LOADING CELL STUDY

This chapter presents results from Li-ion cells with high electrode loadings to show how they compare to cells with regular loading. Comparable cycling performance would translate to cells with increased energy density. A corresponding manuscript has been submitted for publication. Author contributions include cell formation, cycling, post-cycling analysis, data processing and presentation, and finally cell disassembly. J. Harlow also aided in disassembly and interpretation.

Motivation and Additional Background

One simple way to improve energy density is to increase active material loading on the negative and positive electrodes which then minimizes the fractions of inactive materials, such as the separator and current collectors, in the cell. However, previous work has demonstrated that increasing the positive electrode mass loading in cells exposes additional challenges in electrode coating,^{137,138} cell formation, and cell performance.^{137,139} Zheng et al. found that the specific discharge capacity decreased, and internal cell resistance increased when the positive electrode loading of $\text{Li}[\text{Ni}_{1/3}\text{Mn}_{1/3}\text{Co}_{1/3}]\text{O}_2$ (NMC111) increased.¹⁴⁰ In later studies, Park et al. identified uneven state of charge distributions between the active material particles closest to the current collector and farthest from the current collector. In that work, they attributed the uneven state of charge distribution to lower ion conductivity of electrolyte during cycling. Additional work by Kim et al. used stacked active material layers, connected with Al ‘mesh’, to probe degradation at the inner and outer layers of active material on an electrode with higher loading.¹³⁹ Kim et al. found increased SEI thickness and increased resistance in active material particles at the outer

layers of the thick electrodes (farthest from current collector) which caused uneven states of charge in the outer versus inner electrode (closest to current collector).¹³⁹

Kim et al. found the uneven state of charge could be mitigated by altering particle size along electrode thickness which minimized the effect of SEI on the outermost electrode particles.¹³⁹ Others have altered the conductive material added to positive electrode material or altered the electrode pore structure to improve conductivity or tortuosity, respectively, of electrodes with higher loading.¹⁴¹

If electrodes are well prepared, mechanically robust, and well wetted by electrolyte to ensure that particles remain in electrical and ionic contact during charge discharge cycling, then one should be able to make electrodes as thick as one wants, subject to the transport limitations of the electrolyte. As an example, Dahn et al. used 1.0 mm thick electrodes in LiNiO₂/petroleum coke Li-ion coin cells that operated with C/16 currents for over 300 cycles with minimal capacity loss.¹⁴² The electrolyte used was a 50:50 solvent blend of EC and dimethoxyethane to easily wet the thick electrodes and provide high Li-ion conductivity. The petroleum coke electrodes used in Reference 142 had an average voltage versus lithium of about 0.4 V, thus minimizing the risk of lithium plating at the current densities used. Significantly more care is required when a graphite negative electrode is used.

In this study, results from Li[Ni_{0.5}Mn_{0.3}Co_{0.2}]O₂ (NMC532)/graphite Li-ion cells with high electrode loading and low porosity are presented which show comparable charge-discharge cycling performance and ageing to similar cells with regular electrode loading and low porosity without any electrode or electrolyte modifications. Charging currents were selected to avoid lithium plating and were typically limited to a maximum of C/4 for the

high loading cells. The positive electrode material was single crystal NMC532 and positive electrodes were prepared with either 19.3 mg cm⁻² (regular loading) and 29.2 mg cm⁻² (high loading) active material loading. The positive electrodes were calendared to a density of 3.5 g/cm². The negative active electrode material in these cells was Kaijin AML-400 artificial graphite (Kaijin, China). The negative electrode loading was varied proportionally to the positive loading to maintain the same negative to positive capacity balance. Table 5-1 shows the impact of increasing the active material loading and the resulting calculated theoretical stack energy density. This demonstrates how a ~50% increase in active material loading used in this study can translate to over 8% increase in overall stack energy density.

Table 5-1 – Measured electrode loadings and calculated stack energy density. Stack energy density calculations measure the energy per volume of electrode stack (negative electrode coating, copper current collector, negative electrode coating, separator, positive electrode coating, aluminum current collector, positive electrode coating, and separator). Included in the calculation are the positive electrode density (3.5 g cm⁻³), reversible capacity (175 mAh g⁻¹), irreversible capacity (10%), negative electrode density (1.55 g cm⁻³), reversible capacity (350 mAh g⁻¹), and irreversible capacity (8%). The calculations assume the thicknesses of the copper foil, aluminum foil and separator are 8 μm, 15 μm, and 16 μm, respectively. The calculation assumes an N/P ratio of 1:1 at 4.3 V, and a 3.75 V average cell potential.

Pos. Electrode Loading / mg cm ⁻²	% Active Pos. Electrode Material	Neg. Electrode Loading / mg cm ⁻²	% Active Neg. Electrode Material	Stack Energy Density / Wh L ⁻¹
29.2	94	16.6	95.4	956
19.3	94	11.8	95.4	884

Cells in this work underwent Ultra High Precision Coulometry (UHPC) analysis and long-term cycling to compare capacity retention and impedance growth over time for the regular and high loading cells. Charge and discharge rates were chosen to avoid lithium plating.

The included results demonstrate the comparable performance from cells with high electrode loading versus the regular electrode loading, indicating cells with thick electrodes and higher stack energy density are obtainable without additional modification.

Cell Specifications

Pouch cells used in this study were custom manufactured by Li-Fun Technologies (Xinma Industry Zone, Golden Dragon Road, Tianyuan District, Zhuzhou City, Hunan Province, PRC, 412000). The cells contained NMC532 positive electrode materials and AML negative electrode materials described in previous sections (see Chapter 3), however, for this study, the thickness of electrode material on the current collectors varied. The “regular loading” electrodes had a 19.3 mg cm^{-2} positive mass loading covering a geometric area of 67 cm^2 . These cells are comparable to those studied previously by Harlow et al, Li et al., Thompson et al. and Liu et al.^{23,123,126,143} The “high loading” electrodes in this study had a 29.2 mg cm^{-2} positive electrode loading (over 50% increase) covering a geometric area of 49 cm^2 . Negative electrode loadings were 12.2 mg cm^{-2} and 16.6 mg cm^{-2} for regular and high loading cells, respectively. Additionally, the N:P ratios for regular and high loading cells were ~ 1.1 to a 4.3 V balance. The cells had nominal capacities of 230 mAh to 4.3 V. Before filling with electrolyte, cells were opened under inert atmosphere and heated under vacuum to $(100 \pm 1)^\circ\text{C}$ for 14 h to remove residual moisture.

Electrolyte

Two electrolyte mixtures were used in this study. The electrolytes were chosen for their excellent performance measured in previous studies.^{23,85} The first electrolyte blend

contained 1.1 m LiPF₆ dissolved in 25% w/w EC, 5% EMC, and 70% DMC with additional 2% VC, and 1 % DTD as electrolyte additives. The second electrolyte contained 1.1 m LiPF₆ in EC: EMC: DMC (25:5:70 w/w%) with 2% FEC and 1% LiPO₂F₂ additives (see Appendix B for names, sources, and purities). Electrolyte was mixed and added to dried pouch cells as described in previous sections (see Chapter 3). Cells were then immediately transferred to a voltage source and held at 1.5 V for over 48 h. This step was longer than previous work on regular loading cells because of the thicker active material loading. The extended time ensured complete permeation of the entire electrode by the electrolyte.

Cell Formation

After wetting, cells underwent the first, formative charge and discharge cycle on a Maccor series 4000 charger. The cells were charged to their designated upper cutoff potentials (4.1 – 4.4 V) then discharged to the mid-point potential (3.8 V) at C/20 (~11 mAh) current in a temperature-controlled box at 40.0 ± 0.1°C.

EIS Measurements

Alternating current impedance spectra from cells at mid-point potential, 3.8 V, were measured on a BioLogic VMP3 potentiostat after formation. Cells were held at 10.0 ± 0.1°C to increase spectral differences and an AC potential (10 mV amplitude) was applied with varying frequencies (10 mHz – 100kHz). The resulting Nyquist plots were analyzed with RelaxIS software developed by RHD Instruments. This used a simple model to

determine solution resistance (R_s) and charge transfer resistance (R_{CT}). EIS was also measured at the mid-point potential at the end of cycling.

UHPC Cycling

Some cells underwent cycling on the Ultra High Precision Charger (UHPC) developed at Dalhousie University.⁹⁷ Measurements on the UHPC allow small differences in parasitic reaction rates to be identified in a short period of time. Cells with high and regular loading were cycled at $C/20$ at constant current (CC) for 30 cycles or ~ 1200 h. Cells were cycled from 3.0 V to various upper cutoff potentials (4.1 V, 4.2 V, 4.3 V, or 4.4 V). Highly accurate and precise measurements of coulombic efficiency, charge end point capacity, discharge capacity, and voltage polarization were made to probe parasitic reaction rates.

Cell Cycling

Cells were also cycled for about 6000 h (1000 – 2000 cycles) at various temperatures (20°C, 40°C, and 55°C) on Neware battery testers. Cells were cycled from 3.0 V to 4.3 V UCP at various charge and discharge rates (C-rates) using a CCCV protocol for 50 charge and discharge cycles. After every 50 cycles, a $C/20$ discharge, charge, and discharge was applied to obtain the low-rate capacity before returning to the higher rate charge and discharging. C-rates were selected for each testing temperature to avoid Li-plating. Cells at 55 °C were tested at $C/3$ whereas cells at lower temperatures, 40 °C and 20 °C, underwent $C/4$ testing primarily. Selected cells were tested at $C/2$. Under these conditions, Li-plating is not expected to occur and therefore is not expected to contribute to cell degradation.

UHPC Cycling Results

Figure 5-1a. shows the normalized capacity versus time for high and regular loading NMC532/graphite cells containing 2% FEC and 1% LiPO₂F₂ additives. All cells show a similar rate of absolute capacity loss (see Figure A-14a.). Figure 5-1b. shows the normalized voltage polarization versus time. These results showed minimal change in voltage polarization from cycle 10 to the end of cycling (less than 3% change) indicating minimal change to internal resistance. The internal resistance of the regular loading cells tested to an UCP of 4.3 V and the high loading cells cycled to 4.4 V UCP did show a positive increase in voltage polarization for this electrolyte.

Figure 5-1c. shows the coulombic efficiency (CE) and Figure 5-1d. shows the zeroed charge end point capacity versus time. A deviation from 100.00% in coulombic efficiency measurements results from parasitic reactions at both the positive and negative electrodes. Both lithium inventory loss at the negative and oxidation reactions at the positive contribute to a reduction in CE below 1.0000. Active mass loss, which might be more prevalent in cells with high electrode loading, would also cause a reduction in CE. The CE slowly approaches a value near 1.0000 as cycling proceeds as the SEI layer on the negative electrode thickens and passivation layers on the positive electrode become more robust. As seen in previous studies, when the upper cutoff potential is increased, the deviation of the CE from 1.0000 is larger, indicating greater rates of parasitic reactions.^{98,144} Here, the coulombic efficiency of cells with high loading and regular loading cycled to 4.3 V agrees after 1200 h (30 cycles) which shows that the electrode loading does not affect the parasitic reaction rates and that the high loading cells do not have greater rates, if any, of active material loss. The zeroed charge endpoint capacity increases more rapidly when the upper

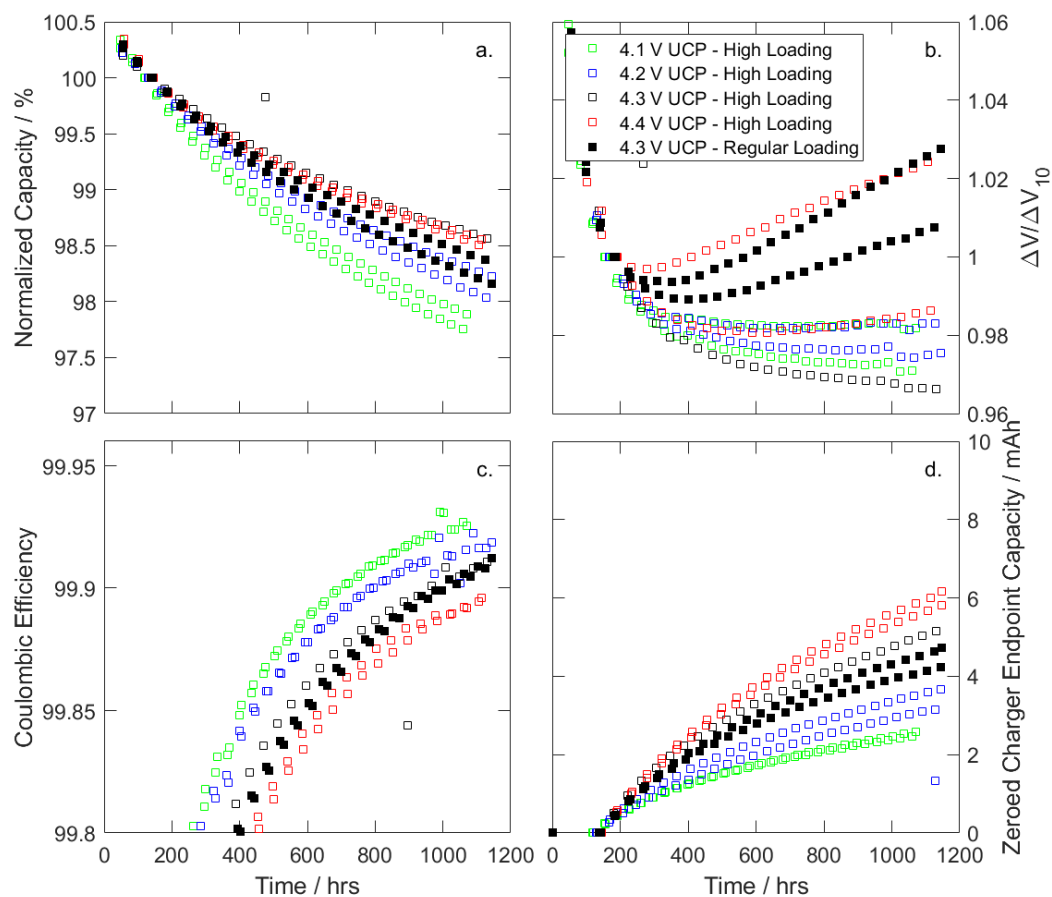


Figure 5-1 – UHPC cycling results for high (open squares) and regular (solid squares) loading cells containing 2% FEC + 1% LiPO₂F₂ additives. Cells were cycled from 3.0 V to various UCPs indicated by marker colour (green, blue, black, and red for UCPs 4.1 V, 4.2 V, 4.3 V and 4.4 V, respectively). Panel (a.) shows the normalized capacity versus time, panel (b.) shows the relative voltage polarization change versus time, and panel (c.) shows the coulombic efficiency versus time. Panel (d.) shows the zeroed charge end point capacity increase versus time.

cutoff potential is increased due to higher rates of electrolyte oxidation. This agrees with previous studies on regular loading cells from Li et al. and Ma et al.^{36,145} Again, the charge endpoint capacity versus time data for cells with regular and high loading electrodes tested

to 4.3 V agree well, showing that the loading does not affect the parasitic reaction rate at the positive electrode.

Figure 5-2a. shows the normalized capacity versus time for high and regular loading NMC532 cells containing 2% VC and 1% DTD tested on the UHPC. Figure A-14b. shows the absolute capacity loss for cells versus time. Figure 5-2a. shows that the high and regular loading cells tested to 4.3 V experience similar rates of capacity loss at the end of the 1200 h period. Figure 5-2b. shows the normalized voltage polarization versus time which is similar for all cells.

Figure 5-2c. shows the coulombic efficiency versus time and Figure 5-1d. shows the zeroed charger end point capacity versus time. The same statements can be made regarding these figures as were made for Figure 5-1d. In summary, Figure 5-1 and Figure 5-2 show that the regular and high loading cells tested between 3.0 and 4.3 V at C/20 and 40°C show the same parasitic reaction rates and that the high loading cells do not have an increased rate of active material loss.

UHPC Gas Production

Figure A-15 shows the volume change of the cells tested on the UHPC due to gas production after 1200 h cycling at 40°C plotted versus the upper cutoff potential. Figure A-15a. shows the results for cells containing 2% FEC and 1% LiPO₂F₂. Here, the measured gas increased for cells cycled to higher upper cutoff potentials. This finding has been

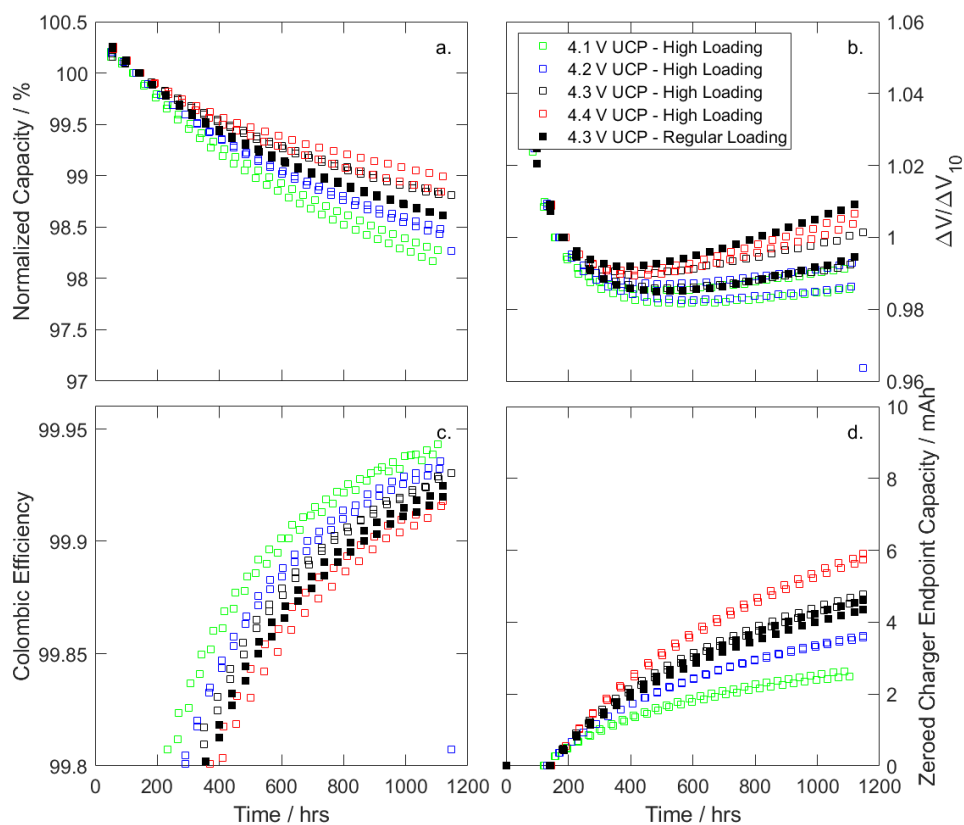


Figure 5-2 – UHPC cycling results for high (open squares) and regular (solid squares) loading cells containing additives 2% VC and 1% DTD cycled from 3.0 V to various upper cutoff potentials indicated in legend. Panel (a.) shows the normalized capacity, panel (b.) shows the relative voltage polarization growth, and panel (c.) shows the fractional charge efficiency versus time. Panel (d.) shows the zeroed charger end point capacity versus time.

observed previously and is consistent with the observed increased presence of parasitic reactions at the positive electrode.¹⁴⁶ The high loading cells showed comparable gas production compared to cells with regular loading. It should be noted that the volume of these pouch cells is 2.5 mL so the amounts of gas production in Figure A-15a. are not noticeable to the human eye.

Figure A-15b. shows the volume change resulting from gas production for high and regular loading cells containing the additives 2% VC and 1% DTD after 1200 hours of testing on the UHPC. Here, cells at lower upper cutoff potentials showed gas consumption. This is likely due to CO₂ gas consumption occurring at the negative electrode as reported by Ellis et al.⁶⁸ Cells cycled to higher upper cutoff potential showed less gas consumption. The observed change in gas volume is indicative of both the rate of production of gasses in the cell and the rate of consumption. Less gas consumption in cells cycled to higher upper cutoff potentials is consistent with higher measured gas production of cells cycled to higher upper cutoff potentials. Again, the volumes of gas being produced or consumed in these cells are extremely small.

Figure A-15 also highlights some of the differences in gas production observed in cells containing additives 2% FEC and 1% LiPO₂F₂ and the cells containing 2% VC and 1% DTD. Cells containing FEC and LiPO₂F₂ show significantly more gas production than cells containing VC and DTD. While both VC and FEC are expected to produce CO₂, the additive FEC has been shown to produce slightly higher amounts of CO₂.³⁹ Additionally, the additive DTD has been shown to decrease gas production in cells especially when paired with VC.^{44,45}

Long-Term Cycling Results

Figure 5-3 shows the discharge capacity, normalized discharge capacity, and voltage polarization increase for NMC532/graphite cells containing 2% FEC and 1% LiPO₂F₂ additives. Panels in the left column show results for cells cycled at 20°C at C/4 and C/2 rates as indicated **in the legend**. The middle column shows results for regular and high

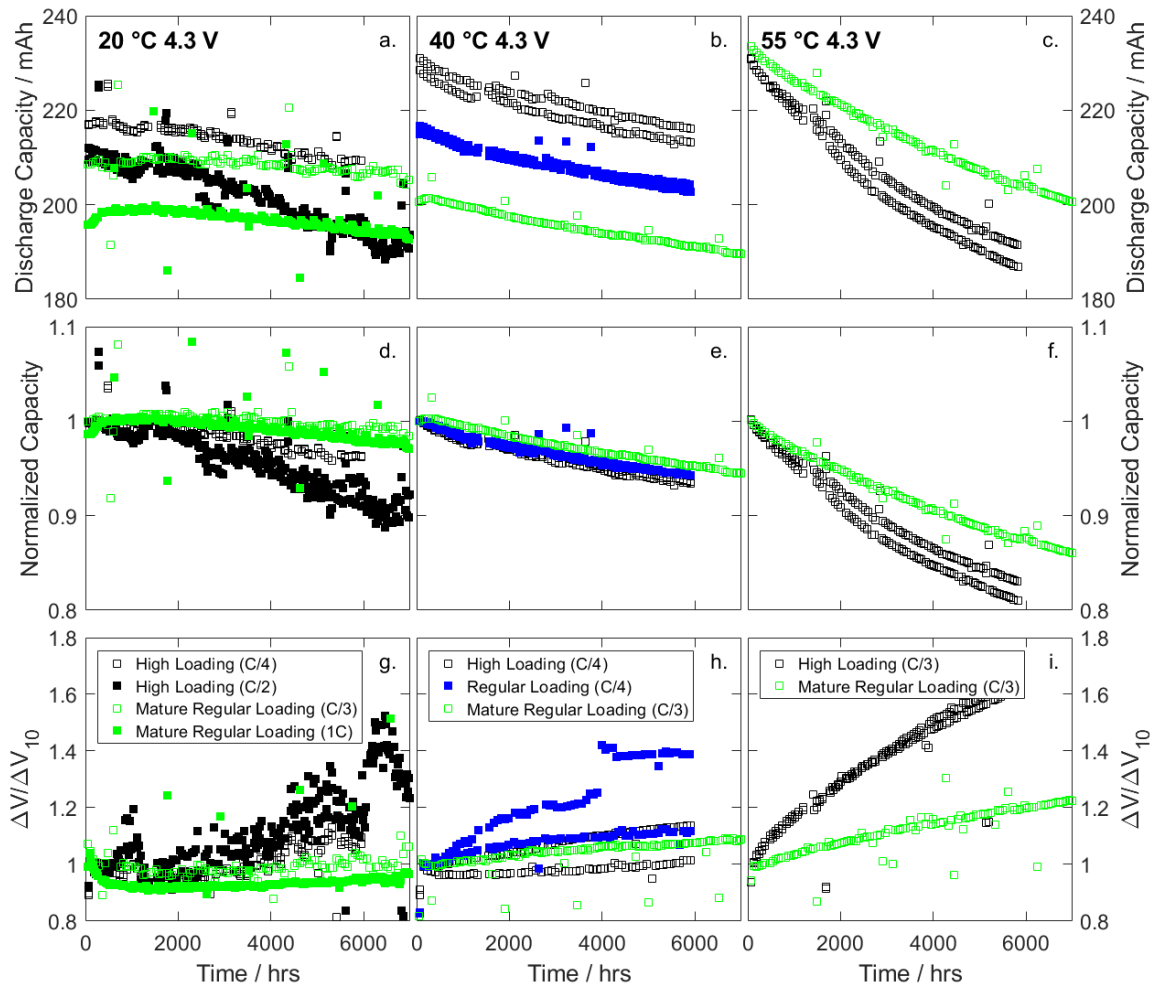


Figure 5-3 – Cycling results from high (black squares) and regular (blue squares) loading cells containing 2% FEC + 1% LiPO₂F₂ additives at various temperatures; 20°C, 40°C, and 55°C (columns a., b., and c. respectively). Rates of charge/discharge from 3.0 to 4.3 V are indicated in legend. Data from older, comparable regular loading cells are shown in green. Panels (a. – c.) show the absolute discharge capacity versus time. Panels (d. – f.) show the normalized capacity versus time. Panels (g. – i.) show the normalized voltage polarization versus time.

loading cells cycled at 40°C at C/4. The right column shows results from high loading cells cycled at C/3 at 55°C. In addition to the regular loading cells from this study, data from cells with the same build and electrolyte called mature regular loading cells are indicated in the middle (40°C) and right columns (55°C).

Figure 5-3d. shows that high loading cells at 20°C cycled at C/4 have better capacity retention (97% after 6000 h) than those cycled at C/2 (92% after 6000 h). This may suggest slight metallic lithium deposition is occurring at C/2. The voltage polarization increase is larger for the cells tested at the higher C-rate. The cells charge and discharged at C/2 C-rate continued to cycle for approximately 12000 more hours (~2000 more cycles, ~1.3 years) until they reached 80% capacity. Figure A-16 shows the extended cycling results for these cells. Figure A-17a. shows photos of negative electrodes removed from these cells at the end of cycling and Figure A-17b. shows a close-up of the left electrode. In this image, Li deposition is observed as metallic lithium (white circles) and dendritic lithium (blue circles)

Figure 5-3e. shows excellent agreement between the normalized capacity versus cycle number of high and regular loading cells at 40°C and at C/4. Additionally, the historical cell agrees well with the other cells. Voltage polarization for this temperature indicates similar internal resistance growth for all cells during testing. Noise measured in voltage polarization panels is likely due to poor connections to the tabs of the cells.

High loading cells cycled to 55 °C show increased capacity fade (83%) compared to a historical normal loading cell (89%) (Figure 5-3c. and Figure 5-3f.). The high loading cells also show a larger increase in voltage polarization. If the parasitic reactions occur at the same rate on the positive electrodes of the high and regular loading cells as suggested by the UHPC results in Figure 5-1 and Figure 5-2, then there will be a greater rate of reaction product generation **per unit area** in the high loading cells. If some of these reaction products move to the negative electrode and film its surface, then one would expect impedance growth rates to be greater in high loading cells tested at extreme temperatures.

To investigate this, the rate of normalized impedance growth from 0 to 6000 h for regular loading cells at 55 °C was multiplied by the ratio of electrode areas to compare with high loading cells cycled at 55 °C. Calculated rates from cells containing both electrolyte chemistries showed no distinguishable difference between regular and high loading impedance growth when standardized to the same electrode area (95% confidence). This is consistent with the observed similar rate of parasitic reactions for the cells with high and regular loading.

Figure 5-4 shows the discharge capacity, normalized capacity, and voltage polarization increase versus time for NMC532/graphite high and regular loading cells containing 2% VC and 1% DTD. Like Figure 5-3, results from cells at 20°C are shown in panels (a, d, and g.), cells at 40°C are shown in panels (b, e, and h.) and cells at 55°C are shown in panels (c, f, and i.). Historical data from older NMC532 cells with 2% VC and 1% DTD are also indicated for selected conditions where data is available.

Figure 5-4d. shows that capacity retention at 20°C is best in the historic cell (99%, C/3, 20 mg/cm²), followed by high loading at C/4 (97%, 30 mg/cm²), and worst is high loading at C/2 (94%). The areal current density is 1.02, 1.10, and 2.19 mA cm⁻² respectively. Figure 5-5 shows the relationship between capacity retention and areal current density of cells from this study and of the mature cells presented in Figure 5-3 and Figure 5-4. The absolute capacity (Figure 5-5a.) and normalized capacity (Figure 5-5c.) versus areal current density for cells containing 2% FEC and 1% LiPO₂F₂ at various cycling temperatures indicates that increasing areal current density for cells at 20, 40, and 55 °C may cause a small decrease in normalized capacity after this time period. Cells containing 2% VC and 1% DTD confirm this relationship. While more data, especially at higher areal densities and

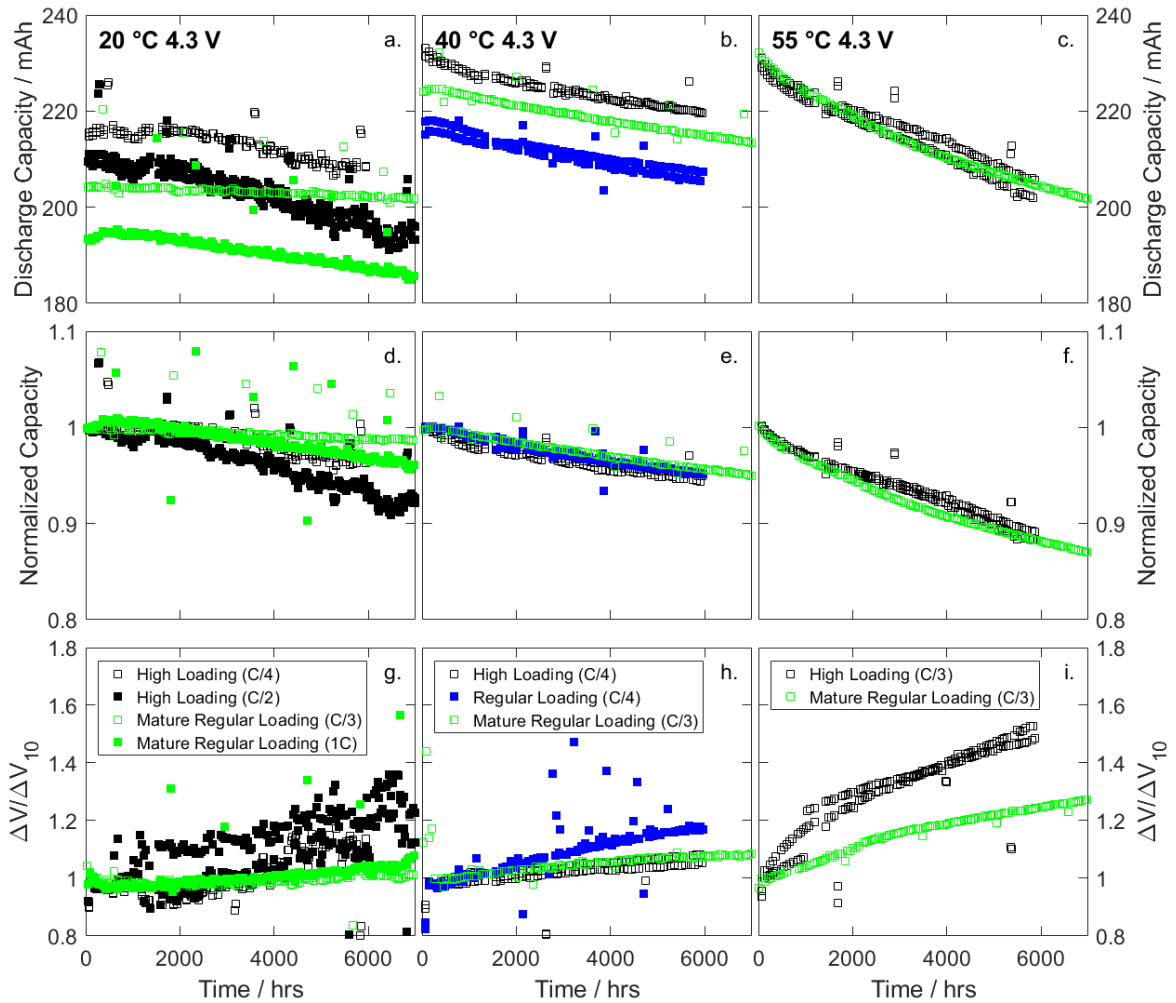


Figure 5-4 – Cycling results from high (black squares) and regular (blue squares) loading cells containing 2% VC + 1% DTD additives at various temperatures 20 °C, 40 °C, and 55 °C (columns a., b., and c. respectively). Rates of charge/discharge from 3.0 to 4.3 V are indicated in legend. Data from older, comparable cells are shown in green as mature, regular loading cells. Panels (a. – c.) show the absolute discharge capacity versus time. Panels (d. – f.) show the normalized capacity versus time. Panels (g. – i.) show the normalized voltage polarization versus time.

higher temperatures, is needed to define concrete relationships, the findings from this study may indicate little effect of increasing areal current density on normalized capacity retention in this temperature and C-rate range. Beyond this C-rate range (above 1C), capacity retention is expected to decrease due to Li deposition, as was reported by Liu et

al.³⁷ It was not until C-rates reached 1.5C (3.2 mAh cm⁻²) and 2C (4.3 mAh cm⁻²), that dramatic capacity loss and Li deposition were detected for their NMC111./graphite cells with similar additive chemistries.^{37,147} Voltage polarization growth was also larger in the higher loading cells. High loading cells with 2% VC and 1% DTD additives continued to cycle at C/2 C-rate for about 12000 additional hours until 80% capacity was reached. Figure A-18 shows the extended cycling results for these cells. Figure A-17c. shows the negative electrode removed from this cell. Here, small areas were identified to have lithium deposition (white circles in Figure A-17c.). The extent of lithium deposition was less than observed in cells with 2% FEC and 1% LiPO₂F₂ additives.

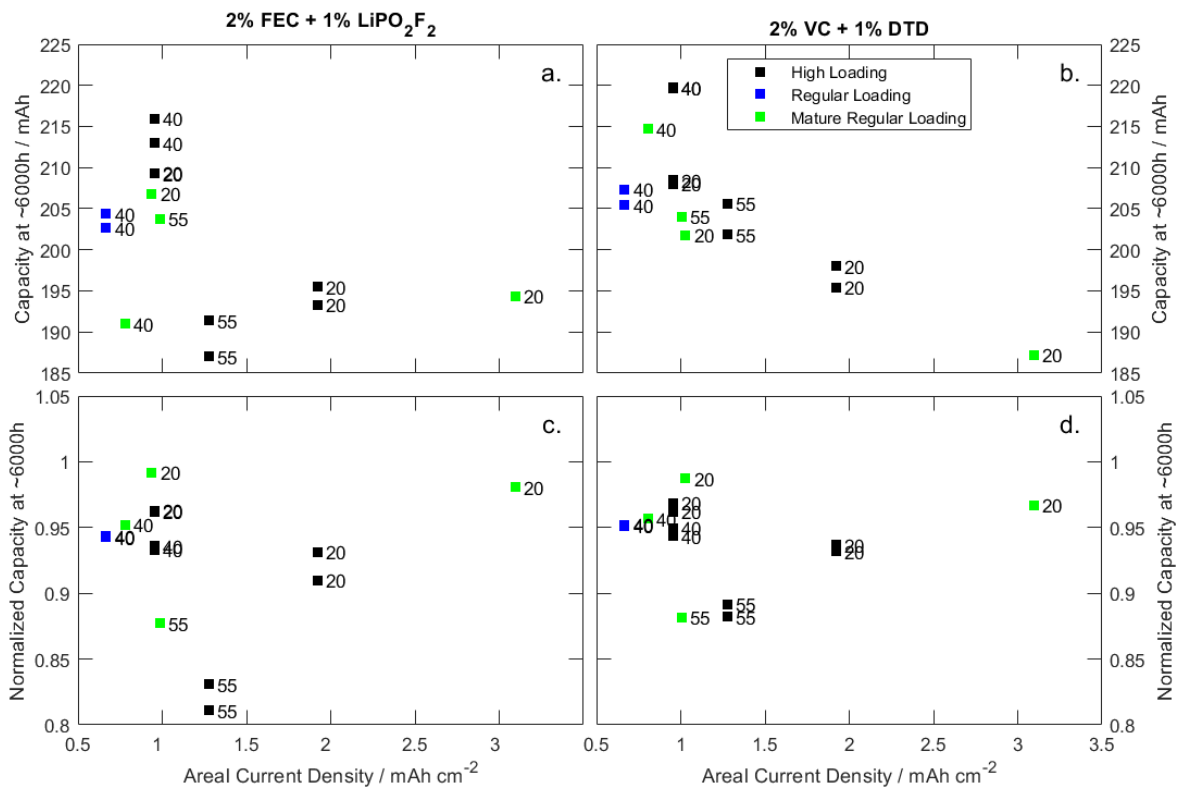


Figure 5-5 – Capacity at ~6000 h versus areal current density for cells with additives 2% FEC + 1% LiPO₂F₂ (a.) and 2% VC + 1% DTD (b.) at 20, 40, and 55 °C (black, blue, and green squares, respectively). The normalized capacity versus areal current density for cells containing 2% FEC and 1% LiPO₂F₂ (c.) and 2% VC + 1% DTD (d.).

Normalized capacity versus cycle number results for cells cycled at 40°C (Figure 5-4e.) show that high loading and regular loading cells have virtually identical behavior (all near 95% original capacity at 6000 h). The voltage polarization growth is also similar for regular and high loading cells: however, the cells with regular loading from this study show slightly higher voltage polarization growth, while the historical cells with regular loading have virtually identical behavior to the high loading cells from this study.

High loading and regular loading cells at 55°C also show comparable normalized capacity results (89% original capacity after 6000 h). However, the voltage polarization growth was also larger in the cells with high loading electrodes as in Figure 5-3i. most likely for the same reasons. The change in the slope of the capacity versus cycle number curve of the high loading cells towards the end of cycling and the increased voltage polarization may indicate the high loading cell would soon experience accelerated capacity loss due to the increased rates of reaction product generation **per unit electrode area**.

Figure A-19 shows the gas production measured from high loading cells containing 2% FEC and 1% LiPO₂F₂ from this study (blue) at the cycled temperatures. Comparable data (from same cell chemistry and cycling protocol) was not available for the equivalent regular loading cells, but data was available from cells that were stored at 4.3 V open circuit potential (versus cycled 3.0 V – 4.3 V) at 20 and 40 °C for 18 months. Previous studies found that the rate of gas production is constant for these cells.¹⁴³ Therefore, it is reasonable to estimate the amount of gas present after 6000 h (~9 months) via interpolation. While comparing previous data, it was also found that the gas volume measured in cells containing 2% FEC and 1% LiPO₂F₂ were within 3% of the gas volume measured in cells containing 1% LiPO₂F₂ only. While this may not hold at 55°C, the volume of gas produced

from these cells with regular loading were also compared (red). Since this data is data from open circuit potential storage, it is expected the gas volume for the equivalent cycled cells will be less.¹⁴³ Still, Figure A-19 suggests that cells with high loading may experience comparable gas production, especially at higher temperatures.

EIS Spectra after Cycling

Figure 5-6 shows an example of EIS spectra measured before (solid lines) and after cycling for 6000 hours (dashed lines) for high loading cells and regular loading cells. The EIS spectra were measured at 10°C and with the cells at 3.8 V. The high loading cells were cycled at 20, 40 or 55 °C while the regular loading cells were cycled at 40°C. Since higher loading cells had 1.5X the positive electrode particles per area of electrode, results for high loading cells were multiplied by 1.5 to compare charge transfer impedances in $\Omega \text{ cm}^2$. Figure 5-6 shows cells with high and regular loading show similar R_S and R_{CT} before and after cycling. Therefore, cells with high and regular electrode loading also have similar increases in R_{CT} over the 6000 h of cycling. This indicates impedance growth associated with the charge transfer at the electrode particles is not significantly changed when the thickness of the active material is increased.

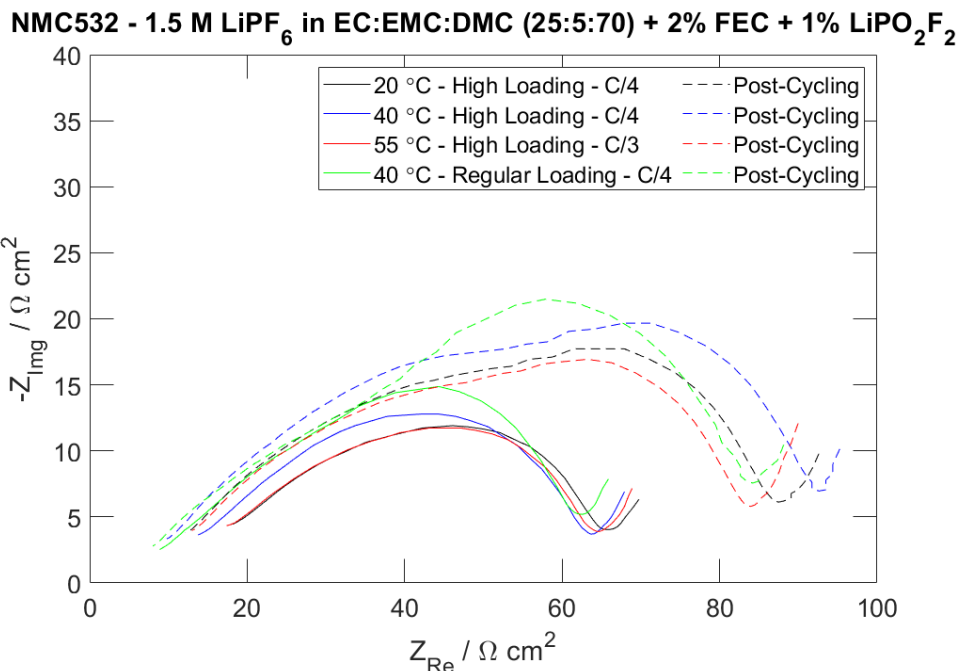


Figure 5-6 – Examples of EIS spectra from high and regular loading cells containing additives 2% FEC + 1% LiPO₂F₂ before (solid lines) and after (dashed lines) cycling for 6000 hours between 3.0 and 4.3 V as in Figure 5-3. High loading cells cycled at 20°C, 40°C, and 55°C are shown in black, blue, and red, respectively. Spectra from high loading cells were multiplied by 1.5 to account for the increased number of electrode particles per surface area. Cells with regular loading at 40°C are shown in green. EIS spectra were measured with the cells at 3.8 V and at 10°C.

Summary

In this study, NMC532 cells with regular and high loading electrodes were compared. The results indicate similar cycling and performance results for cells at 20°C and 40°C when Li-plating is avoided. Findings from UHPC showed similar absolute capacity loss, impedance growth, and similar extents of parasitic reactions. Long-term cycling results confirmed that the normalized capacity loss was comparable for cells at 20 °C and 40 °C when charged and discharged at C/4. High loading cells at 20°C which underwent C/2 charge/discharge showed higher capacity loss and internal impedance growth than their

equivalent regular loading cell, presumably due to small amounts of Li deposition. High loading cells at 55 °C tested under C/3 charge/discharge were shown to have impedance growth rates comparable to regular loading cells when standardized.

These findings suggest that the stack energy density of a cell can be improved by over 8% under optimal temperature and charge-rate conditions, with no further alteration of electrolyte or electrode material. For large-scale cell implementation, this translates to significantly increased energy density, decreased volume of cells, and/or decreased cost of inactive material.

CHAPTER 6 – CONCLUSION

Conclusions

This document presents studies of the changes to the electrolyte and electrodes in Li-ion cells that were tested or stored for periods up to one year. Chapter 3 introduced the analysis methods developed for the long-term electrolyte study. The derived methods allowed salt and organic species concentrations to be determined from a single electrolyte extract. This method employed both ^1H and ^{19}F -NMR to quantify electrolyte species. The salt(s) were removed from the extract for more sensitive, organic component analysis via GC-MS. This method was applied to the large matrix of cells discussed in Chapter 4.

Chapter 4 presented results of a large, multi-variable study of long-term aged Li-ion cells. This study measured the effects of upper cutoff potential selected for cycling or storage at two different temperatures on the electrolyte from single crystal NMC532 and polycrystalline NMC622 cells. Cells were removed periodically for destructive testing. With the methods of Chapter 3 applied, a timeline of electrolyte compositions was generated. Most of the changes that occurred were linear with time. Increasing upper cutoff potential most significantly impacted transition metal deposition and volume of gas produced in stored cells. Increasing temperature primarily increased the rate of transesterification, dimerization, and transition metal deposition. Cells stored at high potentials (versus cycled cells) showed increased transition metal dissolution, dimerization, and transesterification. A decrease in salt concentration, small decrease in relative EC concentration, and an increase in transesterification products was also observed throughout the testing period. The findings indicate that under conservative cycling conditions (low temperatures), the

electrolyte remains mostly unchanged and there is no significant transition metal dissolution. However, under more aggressive storage conditions (increased temperature and upper cutoff potential), the electrolyte undergoes more observable changes presumed to continue as cells age. Here, when cells were cycled to higher upper cutoff potentials there was minimal change to cycling performance and electrolyte composition, thus, increasing cell energy density with limited penalty to cell lifetime.

A simple method for increasing the energy density of Li-ion cells was discussed in Chapter 5. Cells with high electrode loading were studied to show that it is possible to achieve cycling performance comparable to regular loading cells when Li deposition is avoided (i.e., low charge and discharge rate and higher testing temperatures). In this work, the high loading cells were also shown to have similar parasitic reaction rates and impedance growth rates as the regular loading cells. The impacts of this work translated to as much as 8% increased stack energy density, with no changes to electrolyte or electrode chemistries. The practitioner should realize that there is likely no limit to maximum electrode thickness, provided correspondingly low rates are used to avoid Li deposition.

Future Work

The results of electrolyte and electrode analysis from aged cells (Chapter 4) indicate that as Li-ion cells age there are more changes occurring to the electrolyte composition. However, for cycled cells restricted to upper cutoff potentials of 4.3 V (and below) and temperatures of 40 °C (and below), the changes to the electrolyte were minimal after one year. Further investigation into long-term electrolyte compositional changes is warranted for cells tested for longer periods of time and/or under more extreme conditions. The

electrolyte changes presented in Chapter 4 prompt further fundamental studies of electrolyte reactivity, including the residence time of Li-alkoxides, and the consumption of salt, EC, and CO₂. The work also contextualizes the impact of electrolyte changes on solution resistance, and the application of electrolyte studies conducted outside of full Li-ion cells. The presence of transition metals found on the negative electrode, though limited, also pose further questions regarding the mechanism(s) of transition metal dissolution and deposition, such as the gas produced and the selectivity of transition metals. Proposed investigations include gas analysis to support some of the proposed mechanisms discussed previously and a study of transition metal dissolution and deposition conditions to identify the reason for different of Ni, Mn, and Co deposition ratios.

Literature results discussed in Chapter 2 and findings presented in Chapter 4 indicate that the electrolyte in most Li-ion cells is changing throughout cycling. As mentioned previously, this can potentially change the physical properties of the electrolyte, thus, it is valuable to measure how the electrolyte changes in the presence of these reaction products. A future fundamental study could quantify how electrolyte properties, such as conductivity, resistance, boiling and melting point, and stability are affected by the change in salt concentration as well as the presence of transesterification products, dimerization products, oligomeric carbonates, ethylene glycols, and oligo phosphates. This data would quantify the consequences, if any, of parasitic electrolyte reactions in Li-ion cells.

Results presented in Chapter 4 also identified a gradual decrease in salt concentration (and potentially loss of EC) during the testing period. It was also found via EIS, that some of these cells could have increased solution resistance. Chapter 2 and Chapter 4 discussed some of the potential origins for these reactions, however, further investigation of

electrolyte from long-term cycled cells could help confirm the extent of salt and EC reactivity. A future study could involve measuring extracted electrolyte from cells, like those presented in Chapter 4, with HPLC to potentially identify oligomerization originating for EC and/or salt decomposition. If HPLC is not available, more advanced NMR spectra (such as 2D) could be collected to help identify some of these larger compounds. SEI from these cells could also be analyzed via XPS to identify any species expected to originate from EC and LiPF_6 .

Previous studies, conducted outside of a full Li-ion cell (and cited in Chapter 4), reported a relatively short time (i.e., <1 month) with which transesterification can take place in the presence of Li-alkoxides to achieve equilibrium between concentrations of EMC and transesterification products DMC and DEC.¹²⁹ Electrolyte measured in this work from full cells had not reached these concentrations after 12 months. One explanation, discussed in Chapter 4, is the consumption of Li-alkoxides via CO_2 . Future work could attempt to recreate the equilibrium study to look at the influence of CO_2 . This could be achieved by adding electrolyte containing EMC and 1% Li-alkoxide to two pouch bags. One of the pouch bags could then be filled with CO_2 and the other with inert gas. The bags can be stored and monitored via Archimedes measurements for gas production throughout two to four weeks. During this time, if alkoxides are reacting with CO_2 , we would expect to observe a decrease in bag volume in the bag containing CO_2 only. After this period, the pouch bags can be opened, and the electrolyte sampled via GC-MS for transesterification products to confirm whether the presence of CO_2 limits the rate of transesterification. Additionally, the presence of the expected, insoluble product (Li alkyl carbonate) could be

removed via aqueous extraction and quantified via NMR analysis. These combined results would confirm (or refute) the proposed mechanisms.

Another noteworthy finding from Chapter 4 includes the 1:1 transition metal to moles of gas produced ratio observed in cells at 40 °C. Whereas cells at higher temperatures were expected to have experienced electrolyte reduction (identified via transesterification) a process which is expected to dominate gas production, cells at 40 °C showed minimal evidence of electrolyte reduction and correlated gas production. Instead, these cells showed ~1 mole of gas for every 1 mole of transition metal found on the negative electrode. To further investigate this finding, similar cell chemistries and cycling conditions could be created. After short time in cycling and storage (3-6 months) the cells could be opened for transition metal analysis via μ XRF and gas production analysis via GC-MS to determine the composition of the gases produced. Identifying the gases produced may help identify and confirm the previously proposed mechanisms involving transition metal dissolution (either producing CO₂, O₂, or C₂H₄).

The ratios of Ni, Mn, and Co deposition on the negative electrode also suggests Mn and Co are preferentially dissolved and deposited on the negative electrode versus Ni, especially at higher temperatures. The observed difference in relative transition metal deposition is consistent with some literature results presented in Chapter 2, however, the origin of these differences is still unknown. Future studies considering relative amounts of transition metal deposition under additional conditions would help further understand these results. This could be achieved by observing identical cell chemistries at various temperatures (20 °C – 55 °C), at varying degrees of charge and discharge, and/or held at various potentials. Major studies at the Dahn Laboratory involving various depths of

discharge have recently completed long-term cycling and would be excellent candidates to undergo electrolyte and transition metal analysis. The findings from this study would have a high impact on the understanding of transition metal dissolution and deposition in Li-ion cells.

Future long-term electrolyte and transition metal dissolution studies would benefit from employing the ‘pouch bag’ method, developed by Xiong et al. at Dalhousie University and discussed in Chapter 2. The ‘pouch bag’ method exposed various combinations of electrodes (positive and negative, positive only and negative only) to electrolytes to isolate reaction mechanisms at either electrode.¹⁴⁶ This may help identify any cross-talk reaction mechanisms involving Li^+ , PF_6^- , and/or transition metals occurring within the full cells. Like the study by Sahore et al., future work could isolate the electrode and electrolyte reactions via exposing charged and uncharged electrodes to a sample of electrolyte. Part of this study could recreate and confirm the ICP-MS results of Sahore et al., and the samples could also undergo NMR analysis to determine the effect, if any, on LiPF_6 and organic species. Finally, the volumes of the pouch bags could be monitored and sampled for gas composition analysis via GC-MS. This would inform current understanding of dissolution and deposition to determine the dominate mechanism. If conducted under various conditions (such as state of charge or temperature), it may be possible to observed different mechanisms at work. For example, as Sahore et al. presented, HF causing Mn dissolution while the positive electrode was at low states of charge.

This thesis also discussed altering electrode loading to increase the stack energy density of Li-ion cells. The results from Chapter 5 showed that comparable cycling results were obtainable when maintaining a slower charge and discharge rate. As discussed in Chapter

5, cells studied here were mostly limited to charge rates (C/4 and C/3) to avoid Li deposition. A future study may involve the incorporation of a low viscosity solvent to increase electrolyte conductivity, thus improve cycling capability. While an electrolyte blend with low viscosity solvents has been shown to improve cycling capability of regular loading NMC532 cells,^{33,148} it has yet to be attempted with high loading NMC532 cells. The work from Chapter 5 indicates comparable improvements to charge and discharge capabilities may be possible.

This thesis summarizes recent work aimed at improving the lifetime, energy, and stack energy density of Li-ion cells. Studying long-term electrolyte and electrode changes identified some of the reaction mechanisms occurring as cells age. Identifying these reactions, and the conditions which affect them, help inform future development of electrolyte blends and electrode materials. Additionally, it was found that the electrode stack energy density could be increased by increasing the electrode loading without penalty. With a more stable electrolyte, electrodes, and cell engineering, Li-ion cells can be operable at higher potentials and higher capacities, last longer, and can allow cells to tolerate higher rates of charge and discharge. With higher energy densities, longer lifetimes, and better rate capabilities Li-ion cells can fulfill the expanding and diverse energy storage demands of the near future.

REFERENCES

- (1) Barrington-Leigh, C.; Ouliaris, M. The Renewable Energy Landscape in Canada: A Spatial Analysis. *Renew. Sustain. Energy Rev.* **2017**, *75* (December 2015), 809–819. <https://doi.org/10.1016/j.rser.2016.11.061>.
- (2) Canada's Renewable Power Landscape 2016 <https://www.nelone.gc.ca/nrg/sttstc/lctrct/rprt/2016cndrnwblpwr/prvnc/bc-eng.html>.
- (3) Martins, R.; Hesse, H. C.; Jungbauer, J.; Vorbuchner, T.; Musilek, P. Optimal Component Sizing for Peak Shaving in Battery Energy Storage System for Industrial Applications. *Energies* **2018**, *11* (8). <https://doi.org/10.3390/en11082048>.
- (4) Berrueta, A.; San Martín, I.; Sanchis, P.; Ursúa, A. *Lithium-Ion Batteries as Distributed Energy Storage Systems for Microgrids*; 2019. <https://doi.org/10.1016/B978-0-12-817774-7.00006-5>.
- (5) Avilés A., C.; Oliva H., S.; Watts, D. Single-Dwelling and Community Renewable Microgrids: Optimal Sizing and Energy Management for New Business Models. *Appl. Energy* **2019**, *254* (March), 113665. <https://doi.org/10.1016/j.apenergy.2019.113665>.
- (6) Diouf, B.; Pode, R. Potential of Lithium-Ion Batteries in Renewable Energy. *Renew. Energy* **2015**, *76*, 375–380. <https://doi.org/10.1016/j.renene.2014.11.058>.
- (7) Williams, M. VW to have 240 GWh of battery plants in Europe by 2030 <https://www.automotivemanufacturingsolutions.com/emobility/vw-to-have-240-gwh-of-battery-plants-in-europe-by-2030/41684.article>.
- (8) Ecosystem and All-Electric Future <https://www.gm.com/commitments/electrification.html>.
- (9) Irvine, M.; Rinaldo, M. Tesla Battery Day and the Energy Transition <https://www.dnv.com/feature/tesla-battery-day-energy-transition.html>.
- (10) Duan, J.; Tang, X.; Dai, H.; Yang, Y.; Wu, W.; Wei, X.; Huang, Y. *Building Safe Lithium-Ion Batteries for Electric Vehicles: A Review*; Springer Singapore, 2020; Vol. 3. <https://doi.org/10.1007/s41918-019-00060-4>.
- (11) Liang, Y.; Zhao, C.; Yuan, H.; Chen, Y.; Zhang, W.; Huang, J.; Yu, D.; Liu, Y.; Titirici, M.; Chueh, Y.; Yu, H.; Zhang, Q. A Review of Rechargeable Batteries for Portable Electronic Devices. *InfoMat* **2019**, *1* (1), 6–32. <https://doi.org/10.1002/inf2.12000>.
- (12) Blomgren, G. E. The Development and Future of Lithium Ion Batteries. *J. Electrochem. Soc.* **2017**, *164* (1), A5019–A5025. <https://doi.org/10.1149/2.0251701jes>.

- (13) Schultz, C.; Vedder, S.; Winter, M.; Nowak, S. Investigation of the Decomposition of Organic Solvent-Based Lithium Ion Battery Electrolytes with Liquid Chromatography-Mass Spectrometry. *Spectrosc. Eur.* **2016**, *28* (5), 21–24. <https://doi.org/10.1021/acs.analchem.6b03379>.
- (14) Dahn, J.; Ehrlich, G. M. 17A.0. Section A: Lithium-Ion Batteries. In *Linden's Handbook of Batteries*; McGraw-Hill Education: New York, 2019.
- (15) Mohamed, N.; Allam, N. K. Recent Advances in the Design of Cathode Materials for Li-Ion Batteries. *RSC Adv.* **2020**, *10* (37), 21662–21685. <https://doi.org/10.1039/d0ra03314f>.
- (16) Nitta, N.; Wu, F.; Lee, J. T.; Yushin, G. Li-Ion Battery Materials: Present and Future. *Mater. Today* **2015**, *18* (5), 252–264. <https://doi.org/10.1016/j.mattod.2014.10.040>.
- (17) Dahn, J.; Fuller, E.; Obrovac, M.; Vonsacken, U. Thermal Stability of Li_xCoO_2 , Li_xNiO_2 and $\lambda\text{-MnO}_2$ and Consequences for the Safety of Li-Ion Cells. *Solid State Ionics* **1994**, *69* (3–4), 265–270. [https://doi.org/10.1016/0167-2738\(94\)90415-4](https://doi.org/10.1016/0167-2738(94)90415-4).
- (18) Lee, K. K.; Yoon, W. S.; Kim, K. B.; Lee, K. Y.; Hong, S. T. Thermal Behavior and the Decomposition Mechanism of Electrochemically Delithiated $\text{Li}_{1-x}\text{NiO}_2$. *J. Power Sources* **2001**, *97–98*, 321–325. [https://doi.org/10.1016/S0378-7753\(01\)00548-1](https://doi.org/10.1016/S0378-7753(01)00548-1).
- (19) Arai, H.; Okada, S.; Sakurai, Y.; Yamaki, J. I. Thermal Behavior of $\text{Li}_{1-y}\text{NiO}_2$ and the Decomposition Mechanism. *Solid State Ionics* **1998**, *109* (3–4), 295–302. [https://doi.org/10.1016/s0167-2738\(98\)00075-7](https://doi.org/10.1016/s0167-2738(98)00075-7).
- (20) Schmuck, R.; Wagner, R.; Hörpel, G.; Placke, T.; Winter, M. Performance and Cost of Materials for Lithium-Based Rechargeable Automotive Batteries. *Nat. Energy* **2018**, *3* (4), 267–278. <https://doi.org/10.1038/s41560-018-0107-2>.
- (21) Zhang, N.; Zaker, N.; Li, H.; Liu, A.; Inglis, J.; Jing, L.; Li, J.; Li, Y.; Botton, G. A.; Dahn, J. R. Cobalt-Free Nickel-Rich Positive Electrode Materials with a Core-Shell Structure. *Chem. Mater.* **2019**, *31* (24), 10150–10160. <https://doi.org/10.1021/acs.chemmater.9b03515>.
- (22) Li, H.; Cormier, M.; Zhang, N.; Inglis, J.; Li, J.; Dahn, J. R. Is Cobalt Needed in Ni-Rich Positive Electrode Materials for Lithium Ion Batteries? *J. Electrochem. Soc.* **2019**, *166* (4), A429–A439. <https://doi.org/10.1149/2.1381902jes>.
- (23) Harlow, J. E.; Ma, X.; Li, J.; Logan, E.; Liu, Y.; Zhang, N.; Ma, L.; Glazier, S. L.; Cormier, M. M. E.; Genovese, M.; Buteau, S.; Cameron, A.; Stark, J. E.; Dahn, J. R. A Wide Range of Testing Results on an Excellent Lithium-Ion Cell Chemistry to Be Used as Benchmarks for New Battery Technologies. *J. Electrochem. Soc.* **2019**, *166* (13), A3031–A3044. <https://doi.org/10.1149/2.0981913jes>.
- (24) Warshawsky, I. *Rechargeable Batteries*; Zhang, Z., Zhang, S. S., Eds.; Green Energy and Technology; Springer International Publishing: Cham, 2015; Vol. 36. <https://doi.org/10.1007/978-3-319-15458-9>.

- (25) Fong, R.; von Sacken, U.; Dahn, J. R. Studies of Lithium Intercalation into Carbons Using Nonaqueous Electrochemical Cells. *J. Electrochem. Soc.* **1990**, *137* (7), 2009–2013. <https://doi.org/10.1149/1.2086855>.
- (26) Obrovac, M. N.; Chevrier, V. L. Alloy Negative Electrodes for Li-Ion Batteries. *Chem. Rev.* **2014**, *114* (23), 11444–11502. <https://doi.org/10.1021/cr500207g>.
- (27) Xu, K. Nonaqueous Liquid Electrolytes for Lithium-Based Rechargeable Batteries. *Chem. Rev.* **2004**, *104* (10), 4303–4417. <https://doi.org/10.1021/cr030203g>.
- (28) Xu, K. Electrolytes and Interphases in Li-Ion Batteries and Beyond. *Chem. Rev.* **2014**, *114* (23), 11503–11618. <https://doi.org/10.1021/cr500003w>.
- (29) Xu, K.; Von Cresce, A. Interfacing Electrolytes with Electrodes in Li Ion Batteries. *J. Mater. Chem.* **2011**, *21* (27), 9849–9864. <https://doi.org/10.1039/c0jm04309e>.
- (30) Jow, T. R.; Ding, M. S.; Xu, K.; Zhang, S. S.; Allen, J. L.; Amine, K.; Henriksen, G. L. Nonaqueous Electrolytes for Wide-Temperature-Range Operation of Li-Ion Cells. *J. Power Sources* **2003**, *119–121*, 343–348. [https://doi.org/10.1016/S0378-7753\(03\)00153-8](https://doi.org/10.1016/S0378-7753(03)00153-8).
- (31) Logan, E. R.; Tonita, E. M.; Gering, K. L.; Li, J.; Ma, X.; Beaulieu, L. Y.; Dahn, J. R. A Study of the Physical Properties of Li-Ion Battery Electrolytes Containing Esters. *J. Electrochem. Soc.* **2018**, *165* (2), A21–A30. <https://doi.org/10.1149/2.0271802jes>.
- (32) Logan, E. R.; Tonita, E. M.; Gering, K. L.; Dahn, J. R. A Critical Evaluation of the Advanced Electrolyte Model. *J. Electrochem. Soc.* **2018**, *165* (14), A3350–A3359. <https://doi.org/10.1149/2.0471814jes>.
- (33) Logan, E. R.; Dahn, J. R. Electrolyte Design for Fast-Charging Li-Ion Batteries. *Trends Chem.* **2020**, *2* (4), 354–366. <https://doi.org/10.1016/j.trechm.2020.01.011>.
- (34) Birkl, C. R.; Roberts, M. R.; McTurk, E.; Bruce, P. G.; Howey, D. A. Degradation Diagnostics for Lithium Ion Cells. *J. Power Sources* **2017**, *341*, 373–386. <https://doi.org/10.1016/j.jpowsour.2016.12.011>.
- (35) Vetter, J.; Novák, P.; Wagner, M. R.; Veit, C.; Möller, K. C.; Besenhard, J. O.; Winter, M.; Wohlfahrt-Mehrens, M.; Vogler, C.; Hammouche, A. Ageing Mechanisms in Lithium-Ion Batteries. *J. Power Sources* **2005**, *147* (1–2), 269–281. <https://doi.org/10.1016/j.jpowsour.2005.01.006>.
- (36) Ma, L.; Ellis, L.; Glazier, S. L.; Ma, X.; Liu, Q.; Li, J.; Dahn, J. R. LiPO₂F₂ as an Electrolyte Additive in Li[Ni_{0.5}Mn_{0.3}Co_{0.2}]O₂/Graphite Pouch Cells. *J. Electrochem. Soc.* **2018**, *165* (5), A891–A899. <https://doi.org/10.1149/2.0381805jes>.
- (37) Liu, Q. Q.; Ma, L.; Du, C. Y.; Dahn, J. R. Effects of the LiPO₂F₂ Additive on Unwanted Lithium Plating in Lithium-Ion Cells. *Electrochim. Acta* **2018**, *263*, 237–248. <https://doi.org/10.1016/j.electacta.2018.01.058>.

- (38) Madec, L.; Petibon, R.; Tasaki, K.; Xia, J.; Sun, J. P.; Hill, I. G.; Dahn, J. R. Mechanism of Action of Ethylene Sulfite and Vinylene Carbonate Electrolyte Additives in $\text{LiNi}_{1/3}\text{Mn}_{1/3}\text{Co}_{1/3}\text{O}_2$ /Graphite Pouch Cells: Electrochemical, GC-MS and XPS Analysis. *Phys. Chem. Chem. Phys.* **2015**, *17* (40), 27062–27076. <https://doi.org/10.1039/c5cp04221f>.
- (39) Schwenke, K. U.; Solchenbach, S.; Demeaux, J.; Lucht, B. L.; Gasteiger, H. A. The Impact of CO_2 Evolved from VC and FEC during Formation of Graphite Anodes in Lithium-Ion Batteries. *J. Electrochem. Soc.* **2019**, *166* (10), A2035–A2047. <https://doi.org/10.1149/2.0821910jes>.
- (40) Taskovic, T.; Thompson, L. M.; Eldesoky, A.; Lumsden, M. D.; Dahn, J. R. Optimizing Electrolyte Additive Loadings in NMC532/Graphite Cells: Vinylene Carbonate and Ethylene Sulfate. *J. Electrochem. Soc.* **2021**, *168* (1), 010514. <https://doi.org/10.1149/1945-7111/abd833>.
- (41) Wang, L.; Menakath, A.; Han, F.; Wang, Y.; Zavalij, P. Y.; Gaskell, K. J.; Borodin, O.; Iuga, D.; Brown, S. P.; Wang, C.; Xu, K.; Eichhorn, B. W. Identifying the Components of the Solid–Electrolyte Interphase in Li-Ion Batteries. *Nat. Chem.* **2019**, *11* (9), 789–796. <https://doi.org/10.1038/s41557-019-0304-z>.
- (42) Rinkel, B. L. D.; Hall, D. S.; Temprano, I.; Grey, C. P. Electrolyte Oxidation Pathways in Lithium-Ion Batteries. *J. Am. Chem. Soc.* **2020**, *142* (35), 15058–15074. <https://doi.org/10.1021/jacs.0c06363>.
- (43) Jankowski, P.; Lindahl, N.; Weidow, J.; Wiczorek, W.; Johansson, P. Impact of Sulfur-Containing Additives on Lithium-Ion Battery Performance: From Computational Predictions to Full-Cell Assessments. *ACS Appl. Energy Mater.* **2018**, *1* (6), 2582–2591. <https://doi.org/10.1021/acsaem.8b00295>.
- (44) Zhang, X. Q.; Wang, X. M.; Li, B. Q.; Shi, P.; Huang, J. Q.; Chen, A.; Zhang, Q. Crosstalk Shielding of Transition Metal Ions for Long Cycling Lithium-Metal Batteries. *J. Mater. Chem. A* **2020**, *8* (8), 4283–4289. <https://doi.org/10.1039/c9ta12269a>.
- (45) Haregewoin, A. M.; Wotango, A. S.; Hwang, B. J. Electrolyte Additives for Lithium Ion Battery Electrodes: Progress and Perspectives. *Energy Environ. Sci.* **2016**, *9* (6), 1955–1988. <https://doi.org/10.1039/c6ee00123h>.
- (46) An, S. J.; Li, J.; Daniel, C.; Mohanty, D.; Nagpure, S.; Wood, D. L. The State of Understanding of the Lithium-Ion-Battery Graphite Solid Electrolyte Interphase (SEI) and Its Relationship to Formation Cycling. *Carbon N. Y.* **2016**, *105*, 52–76. <https://doi.org/10.1016/j.carbon.2016.04.008>.
- (47) Ellis, L. D.; Allen, J. P.; Hill, I. G.; Dahn, J. R. High-Precision Coulometry Studies of the Impact of Temperature and Time on SEI Formation in Li-Ion Cells. *J. Electrochem. Soc.* **2018**, *165* (7), A1529–A1536. <https://doi.org/10.1149/2.1091807jes>.

- (48) Wu, Z.; Li, S.; Zheng, Y.; Zhang, Z.; Umesh, E.; Zheng, B.; Zheng, X.; Yang, Y. The Roles of Sulfur-Containing Additives and Their Working Mechanism on the Temperature-Dependent Performances of Li-Ion Batteries. *J. Electrochem. Soc.* **2018**, *165* (11), A2792–A2800. <https://doi.org/10.1149/2.0331811jes>.
- (49) Jung, R.; Metzger, M.; Maglia, F.; Stinner, C.; Gasteiger, H. A. Chemical versus Electrochemical Electrolyte Oxidation on NMC111, NMC622, NMC811, LNMO, and Conductive Carbon. *J. Phys. Chem. Lett.* **2017**, *8* (19), 4820–4825. <https://doi.org/10.1021/acs.jpcclett.7b01927>.
- (50) Henschel, J.; Dressler, J. M.; Winter, M.; Nowak, S. Reaction Product Analyses of the Most Active “Inactive” Material in Lithium-Ion Batteries - The Electrolyte. I: Thermal Stress and Marker Molecules. *Chem. Mater.* **2019**, *31* (24), 9970–9976. <https://doi.org/10.1021/acs.chemmater.9b04133>.
- (51) Sasaki, T.; Abe, T.; Iriyama, Y.; Inaba, M.; Ogumi, Z. Formation Mechanism of Alkyl Dicarbonates in Li-Ion Cells. *J. Power Sources* **2005**, *150* (1–2), 208–215. <https://doi.org/10.1016/j.jpowsour.2005.02.021>.
- (52) Onuki, M.; Kinoshita, S.; Sakata, Y.; Yanagidate, M.; Otake, Y.; Ue, M.; Deguchi, M. Identification of the Source of Evolved Gas in Li-Ion Batteries Using [Sup 13]C-Labeled Solvents. *J. Electrochem. Soc.* **2008**, *155* (11), A794. <https://doi.org/10.1149/1.2969947>.
- (53) Yoshida, H.; Fukunaga, T.; Hazama, T.; Terasaki, M.; Mizutani, M.; Yamachi, M. Degradation Mechanism of Alkyl Carbonate Solvents Used in Lithium-Ion Cells during Initial Charging. *J. Power Sources* **1997**, *68* (2), 311–315. [https://doi.org/10.1016/S0378-7753\(97\)02635-9](https://doi.org/10.1016/S0378-7753(97)02635-9).
- (54) Hobold, G. M.; Khurram, A.; Gallant, B. M. Operando Gas Monitoring of Solid Electrolyte Interphase Reactions on Lithium. *Chem. Mater.* **2020**, *32* (6), 2341–2352. <https://doi.org/10.1021/acs.chemmater.9b04550>.
- (55) Leung, K.; Rempe, S. B.; Foster, M. E.; Ma, Y.; Martinez del la Hoz, J. M.; Sai, N.; Balbuena, P. B. Modeling Electrochemical Decomposition of Fluoroethylene Carbonate on Silicon Anode Surfaces in Lithium Ion Batteries. *J. Electrochem. Soc.* **2014**, *161* (3), A213–A221. <https://doi.org/10.1149/2.092401jes>.
- (56) Jung, R.; Metzger, M.; Haering, D.; Solchenbach, S.; Marino, C.; Tsiouvaras, N.; Stinner, C.; Gasteiger, H. A. Consumption of Fluoroethylene Carbonate (FEC) on Si-C Composite Electrodes for Li-Ion Batteries. *J. Electrochem. Soc.* **2016**, *163* (8), A1705–A1716. <https://doi.org/10.1149/2.0951608jes>.
- (57) Nakai, H.; Kubota, T.; Kita, A.; Kawashima, A. Investigation of the Solid Electrolyte Interphase Formed by Fluoroethylene Carbonate on Si Electrodes. *J. Electrochem. Soc.* **2011**, *158* (7), A798. <https://doi.org/10.1149/1.3589300>.

- (58) Hall, D. S.; Allen, J. P.; Glazier, S. L.; Ellis, L. D.; Ma, L.; Peters, J. M.; Hill, I. G.; Dahn, J. R. The Solid-Electrolyte Interphase Formation Reactions of Ethylene Sulfate and Its Synergistic Chemistry with Prop-1-Ene-1,3-Sultone in Lithium-Ion Cells. *J. Electrochem. Soc.* **2017**, *164* (14), A3445–A3453. <https://doi.org/10.1149/2.0181714jes>.
- (59) Xing, L.; Borodin, O. Oxidation Induced Decomposition of Ethylene Carbonate from DFT Calculations - Importance of Explicitly Treating Surrounding Solvent. *Phys. Chem. Chem. Phys.* **2012**, *14* (37), 12838–12843. <https://doi.org/10.1039/c2cp41103b>.
- (60) Yang, L.; Ravdel, B.; Lucht, B. L. Electrolyte Reactions with the Surface of High Voltage LiNi_{0.5}Mn_{1.5}O₄ Cathodes for Lithium-Ion Batteries. *Electrochem. Solid-State Lett.* **2010**, *13* (8), 95–98. <https://doi.org/10.1149/1.3428515>.
- (61) Jung, R.; Metzger, M.; Maglia, F.; Stinner, C.; Gasteiger, H. A. Oxygen Release and Its Effect on the Cycling Stability of LiNi_xMn_yCo_zO₂ (NMC) Cathode Materials for Li-Ion Batteries. *J. Electrochem. Soc.* **2017**, *164* (7), A1361–A1377. <https://doi.org/10.1149/2.0021707jes>.
- (62) Etacheri, V.; Haik, O.; Goffer, Y.; Roberts, G. A.; Stefan, I. C.; Fasching, R.; Aurbach, D. Effect of Fluoroethylene Carbonate (FEC) on the Performance and Surface Chemistry of Si-Nanowire Li-Ion Battery Anodes. *Langmuir* **2012**, *28* (1), 965–976. <https://doi.org/10.1021/la203712s>.
- (63) Ota, H.; Sakata, Y.; Inoue, A.; Yamaguchi, S. Analysis of Vinylene Carbonate Derived SEI Layers on Graphite Anode. *J. Electrochem. Soc.* **2004**, *151* (10), A1659. <https://doi.org/10.1149/1.1785795>.
- (64) Zhang, B.; Metzger, M.; Solchenbach, S.; Payne, M.; Meini, S.; Gasteiger, H. A.; Garsuch, A.; Lucht, B. L. Role of 1,3-Propane Sultone and Vinylene Carbonate in Solid Electrolyte Interface Formation and Gas Generation. *J. Phys. Chem. C* **2015**, *119* (21), 11337–11348. <https://doi.org/10.1021/acs.jpcc.5b00072>.
- (65) Kawamura, T.; Okada, S.; Yamaki, J. Decomposition Reaction of LiPF₆-Based Electrolytes for Lithium Ion Cells. *J. Power Sources* **2006**, *156* (2), 547–554. <https://doi.org/10.1016/j.jpowsour.2005.05.084>.
- (66) Zaban, A.; Zinigrad, E.; Aurbach, D. Impedance Spectroscopy of Li Electrodes. 4. A General Simple Model of the Li-Solution Interphase in Polar Aprotic Systems. *J. Phys. Chem.* **1996**, *100* (8), 3089–3101. <https://doi.org/10.1021/jp9514279>.
- (67) Kim, G. Interaction between Cathode and Anode and Its Impact on the Production of Alkyl Dicarbonates in Lithium Ion Batteries. *Electrochim. Acta* **2016**, *200*, 46–52. <https://doi.org/10.1016/j.electacta.2016.03.142>.
- (68) Ellis, L. D.; Allen, J. P.; Thompson, L. M.; Harlow, J. E.; Stone, W. J.; Hill, I. G.; Dahn, J. R. Quantifying, Understanding and Evaluating the Effects of Gas Consumption in Lithium-Ion Cells. *J. Electrochem. Soc.* **2017**, *164* (14), A3518–A3528. <https://doi.org/10.1149/2.0191714jes>.

- (69) Parimalam, B. S.; MacIntosh, A. D.; Kadam, R.; Lucht, B. L. Decomposition Reactions of Anode Solid Electrolyte Interphase (SEI) Components with LiPF₆. *J. Phys. Chem. C* **2017**, *121* (41), 22733–22738. <https://doi.org/10.1021/acs.jpcc.7b08433>.
- (70) Freiberg, A. T. S.; Sicklinger, J.; Solchenbach, S.; Gasteiger, H. A. Li₂CO₃ Decomposition in Li-Ion Batteries Induced by the Electrochemical Oxidation of the Electrolyte and of Electrolyte Impurities. *Electrochim. Acta* **2020**, *346*, 136271. <https://doi.org/10.1016/j.electacta.2020.136271>.
- (71) Xiong, D. J.; Hynes, T.; Ellis, L. D.; Dahn, J. R. Effects of Surface Coating on Gas Evolution and Impedance Growth at Li[Ni_xMn_yCo_{1-x-y}]O₂ Positive Electrodes in Li-Ion Cells. *J. Electrochem. Soc.* **2017**, *164* (13), A3174–A3181. <https://doi.org/10.1149/2.0991713jes>.
- (72) Xiong, D. J.; Petibon, R.; Nie, M.; Ma, L.; Xia, J.; Dahn, J. R. Interactions between Positive and Negative Electrodes in Li-Ion Cells Operated at High Temperature and High Voltage. *J. Electrochem. Soc.* **2016**, *163* (3), A546–A551. <https://doi.org/10.1149/2.0951603jes>.
- (73) Harris, O. C.; Tang, M. H. Molecular Probes Reveal Chemical Selectivity of the Solid-Electrolyte Interphase. *J. Phys. Chem. C* **2018**, *122* (36), 20632–20641. <https://doi.org/10.1021/acs.jpcc.8b06564>.
- (74) Xu, K.; Zhuang, G. V.; Allen, J. L.; Lee, U.; Zhang, S. S.; Ross, P. N.; Jow, T. R. Syntheses and Characterization of Lithium Alkyl Mono- and Bicarbonates as Components of Surface Films in Li-Ion Batteries. *J. Phys. Chem. B* **2006**, *110* (15), 7708–7719. <https://doi.org/10.1021/jp0601522>.
- (75) Henschel, J.; Peschel, C.; Günter, F.; Reinhart, G.; Winter, M.; Nowak, S. Reaction Product Analysis of the Most Active “Inactive” Material in Lithium-Ion Batteries - The Electrolyte. II: Battery Operation and Additive Impact. *Chem. Mater.* **2019**, *31* (24), 9977–9983. <https://doi.org/10.1021/acs.chemmater.9b04135>.
- (76) Henschel, J.; Peschel, C.; Klein, S.; Horsthemke, F.; Winter, M.; Nowak, S. Clarification of Decomposition Pathways in a State-of-the-Art Lithium Ion Battery Electrolyte through ¹³C-Labeling of Electrolyte Components. *Angew. Chemie - Int. Ed.* **2020**, *132* (15), 6184–6193. <https://doi.org/10.1002/anie.202000727>.
- (77) Thompson, L. M.; Stone, W.; Eldesoky, A.; Smith, N. K.; McFarlane, C. R. M.; Kim, J. S.; Johnson, M. B.; Petibon, R.; Dahn, J. R. Quantifying Changes to the Electrolyte and Negative Electrode in Aged NMC532/Graphite Lithium-Ion Cells. *J. Electrochem. Soc.* **2018**, *165* (11), A2732–A2740. <https://doi.org/10.1149/2.0721811jes>.
- (78) Gilbert, J. A.; Shkrob, I. A.; Abraham, D. P. Transition Metal Dissolution, Ion Migration, Electrocatalytic Reduction and Capacity Loss in Lithium-Ion Full Cells. *J. Electrochem. Soc.* **2017**, *164* (2), A389–A399. <https://doi.org/10.1149/2.1111702jes>.

- (79) Wandt, J.; Freiberg, A.; Thomas, R.; Gorlin, Y.; Siebel, A.; Jung, R.; Gasteiger, H. A.; Tromp, M. Transition Metal Dissolution and Deposition in Li-Ion Batteries Investigated by Operando X-Ray Absorption Spectroscopy. *J. Mater. Chem. A* **2016**, *4* (47), 18300–18305. <https://doi.org/10.1039/C6TA08865A>.
- (80) Zhan, C.; Wu, T.; Lu, J.; Amine, K. Dissolution, Migration, and Deposition of Transition Metal Ions in Li-Ion Batteries Exemplified by Mn-Based Cathodes-A Critical Review. *Energy Environ. Sci.* **2018**, *11* (2), 243–257. <https://doi.org/10.1039/c7ee03122j>.
- (81) Gallus, D. R.; Schmitz, R. R. W.; Wagner, R.; Hoffmann, B.; Nowak, S.; Cekic-Laskovic, I.; Schmitz, R. R. W.; Winter, M. The Influence of Different Conducting Salts on the Metal Dissolution and Capacity Fading of NCM Cathode Material. *Electrochim. Acta* **2014**, *134*, 393–398. <https://doi.org/10.1016/j.electacta.2014.04.091>.
- (82) Sahore, R.; O'Hanlon, D. C.; Tornheim, A.; Lee, C.-W.; Garcia, J. C.; Iddir, H.; Balasubramanian, M.; Bloom, I. Revisiting the Mechanism Behind Transition-Metal Dissolution from Delithiated $\text{LiNi}_x\text{Mn}_y\text{Co}_z\text{O}_2$ (NMC) Cathodes. *J. Electrochem. Soc.* **2020**, *167* (2), 020513. <https://doi.org/10.1149/1945-7111/ab6826>.
- (83) Li, J.; Cameron, A. R.; Li, H.; Glazier, S.; Xiong, D.; Chatzidakis, M.; Allen, J.; Botton, G. A.; Dahn, J. R. Comparison of Single Crystal and Polycrystalline $\text{LiNi}_{0.5}\text{Mn}_{0.3}\text{Co}_{0.2}\text{O}_2$ Positive Electrode Materials for High Voltage Li-Ion Cells. *J. Electrochem. Soc.* **2017**, *164* (7), A1534–A1544. <https://doi.org/10.1149/2.0991707jes>.
- (84) Ma, L.; Young, S.; Ellis, L. D.; Huang, Q.; Ma, X.; Chatzidakis, M.; Li, H.; Thompson, L.; Eldesoky, A.; McFarlane, C. R. M.; Botton, G. A.; Hill, I. G.; Dahn, J. R. Impact of a Titanium-Based Surface Coating Applied to $\text{Li}[\text{Ni}_{0.5}\text{Mn}_{0.3}\text{Co}_{0.2}]\text{O}_2$ on Lithium-Ion Cell Performance. *ACS Appl. Energy Mater.* **2018**, *1* (12), 7052–7064. <https://doi.org/10.1021/acsaem.8b01472>.
- (85) Li, J.; Li, H.; Stone, W.; Glazier, S.; Dahn, J. R. Development of Electrolytes for Single Crystal NMC532/Artificial Graphite Cells with Long Lifetime. *J. Electrochem. Soc.* **2018**, *165* (3), A626–A635. <https://doi.org/10.1149/2.0971803jes>.
- (86) Qian, Y.; Hu, S.; Zou, X.; Deng, Z.; Xu, Y.; Cao, Z.; Kang, Y.; Deng, Y.; Shi, Q.; Xu, K.; Deng, Y. How Electrolyte Additives Work in Li-Ion Batteries. *Energy Storage Mater.* **2019**, *20* (September 2018), 208–215. <https://doi.org/10.1016/j.ensm.2018.11.015>.
- (87) Aiken, C. P.; Xia, J.; Wang, D. Y.; Stevens, D. A.; Trussler, S.; Dahn, J. R. An Apparatus for the Study of In Situ Gas Evolution in Li-Ion Pouch Cells. *J. Electrochem. Soc.* **2014**, *161* (10), A1548–A1554. <https://doi.org/10.1149/2.0151410jes>.

- (88) Oldenburger, M.; Bedürftig, B.; Gruhle, A.; Grismann, F.; Richter, E.; Findeisen, R.; Hintennach, A. Investigation of the Low Frequency Warburg Impedance of Li-Ion Cells by Frequency Domain Measurements. *J. Energy Storage* **2019**, *21* (November 2018), 272–280. <https://doi.org/10.1016/j.est.2018.11.029>.
- (89) Zhang, S.; Ding, M. S.; Xu, K.; Allen, J.; Jow, T. R. Understanding Solid Electrolyte Interface Film Formation on Graphite Electrodes. *Electrochem. Solid-State Lett.* **2001**, *4* (12), 206–209. <https://doi.org/10.1149/1.1414946>.
- (90) Osaka, T.; Momma, T.; Mukoyama, D.; Nara, H. Proposal of Novel Equivalent Circuit for Electrochemical Impedance Analysis of Commercially Available Lithium Ion Battery. *J. Power Sources* **2012**, *205*, 483–486. <https://doi.org/10.1016/j.jpowsour.2012.01.070>.
- (91) Suresh, P.; Shukla, A. K.; Munichandraiah, N. Temperature Dependence Studies of a.c. Impedance of Lithium-Ion Cells. *J. Appl. Electrochem.* **2002**, *32* (3), 267–273. <https://doi.org/10.1023/A:1015565404343>.
- (92) Abarbanel, D. W.; Nelson, K. J.; Dahn, J. R. Exploring Impedance Growth in High Voltage NMC/Graphite Li-Ion Cells Using a Transmission Line Model. *J. Electrochem. Soc.* **2016**, *163* (3), A522–A529. <https://doi.org/10.1149/2.0901603jes>.
- (93) Nelson, K. J.; Abarbanel, D. W.; Xia, J.; Lu, Z.; Dahn, J. R. Effects of Upper Cutoff Potential on LaPO₄-Coated and Uncoated Li[Ni_{0.42}Mn_{0.42}Co_{0.16}]O₂/Graphite Pouch Cells. *J. Electrochem. Soc.* **2016**, *163* (2), A272–A280. <https://doi.org/10.1149/2.0691602jes>.
- (94) Keefe, A. S.; Buteau, S.; Hill, I. G.; Dahn, J. R. Temperature Dependent EIS Studies Separating Charge Transfer Impedance from Contact Impedance in Lithium-Ion Symmetric Cells. *J. Electrochem. Soc.* **2019**, *166* (14), A3272–A3279. <https://doi.org/10.1149/2.0541914jes>.
- (95) Nelson, K. J.; Harlow, J. E.; Dahn, J. R. A Comparison of NMC/Graphite Pouch Cells and Commercially Available LiCoO₂/Graphite Pouch Cells Tested to High Potential. *J. Electrochem. Soc.* **2018**, *165* (3), A456–A462. <https://doi.org/10.1149/2.0041803jes>.
- (96) Sinha, N. N.; Smith, A. J.; Burns, J. C.; Jain, G.; Eberman, K. W.; Scott, E.; Gardner, J. P.; Dahn, J. R. The Use of Elevated Temperature Storage Experiments to Learn about Parasitic Reactions in Wound LiCoO₂/Graphite Cells. *J. Electrochem. Soc.* **2011**, *158* (11), A1194. <https://doi.org/10.1149/2.007111jes>.
- (97) Bond, T. M.; Burns, J. C.; Stevens, D. A.; Dahn, H. M.; Dahn, J. R. Improving Precision and Accuracy in Coulombic Efficiency Measurements of Li-Ion Batteries. *J. Electrochem. Soc.* **2013**, *160* (3), A521–A527. <https://doi.org/10.1149/2.014304jes>.
- (98) Smith, A. J.; Burns, J. C.; Xiong, D.; Dahn, J. R. Interpreting High Precision Coulometry Results on Li-Ion Cells. *J. Electrochem. Soc.* **2011**, *158* (10), A1136. <https://doi.org/10.1149/1.3625232>.

- (99) Smith, A. J.; Burns, J. C.; Dahn, J. R. A High Precision Study of the Coulombic Efficiency of Li-Ion Batteries. *Electrochem. Solid-State Lett.* **2010**, *13* (12), 177–180. <https://doi.org/10.1149/1.3487637>.
- (100) Smith, A. J.; Burns, J. C.; Trussler, S.; Dahn, J. R. Precision Measurements of the Coulombic Efficiency of Lithium-Ion Batteries and of Electrode Materials for Lithium-Ion Batteries. *J. Electrochem. Soc.* **2010**, *157* (2), A196. <https://doi.org/10.1149/1.3268129>.
- (101) Dahn, H. M.; Smith, A. J.; Burns, J. C.; Stevens, D. A.; Dahn, J. R. User-Friendly Differential Voltage Analysis Freeware for the Analysis of Degradation Mechanisms in Li-Ion Batteries. *J. Electrochem. Soc.* **2012**, *159* (9), A1405–A1409. <https://doi.org/10.1149/2.013209jes>.
- (102) Honkura, K.; Horiba, T. Study of the Deterioration Mechanism of LiCoO₂/Graphite Cells in Charge/Discharge Cycles Using the Discharge Curve Analysis. *J. Power Sources* **2014**, *264*, 140–146. <https://doi.org/10.1016/j.jpowsour.2014.04.036>.
- (103) Honkura, K.; Takahashi, K.; Horiba, T. Capacity-Fading Prediction of Lithium-Ion Batteries Based on Discharge Curves Analysis. *J. Power Sources* **2011**, *196* (23), 10141–10147. <https://doi.org/10.1016/j.jpowsour.2011.08.020>.
- (104) Bloom, I.; Christophersen, J. P.; Abraham, D. P.; Gering, K. L. Differential Voltage Analyses of High-Power Lithium-Ion Cells. *J. Power Sources* **2006**, *157* (1), 537–542. <https://doi.org/10.1016/j.jpowsour.2005.07.054>.
- (105) Ender, M.; Weber, A.; Ellen, I.-T. Analysis of Three-Electrode Setups for AC-Impedance Measurements on Lithium-Ion Cells by FEM Simulations. *J. Electrochem. Soc.* **2011**, *159* (2), A128–A136. <https://doi.org/10.1149/2.100202jes>.
- (106) Dees, D. W.; Jansen, A. N.; Abraham, D. P. Theoretical Examination of Reference Electrodes for Lithium-Ion Cells. *J. Power Sources* **2007**, *174* (2), 1001–1006. <https://doi.org/10.1016/j.jpowsour.2007.06.128>.
- (107) Solchenbach, S.; Pritzl, D.; Kong, E. J. Y.; Landesfeind, J.; Gasteiger, H. A. A Gold Micro-Reference Electrode for Impedance and Potential Measurements in Lithium Ion Batteries. *J. Electrochem. Soc.* **2016**, *163* (10), A2265–A2272. <https://doi.org/10.1149/2.0581610jes>.
- (108) Harlow, J. E.; Glazier, S. L.; Li, J.; Dahn, J. R. Use of Asymmetric Average Charge- and Average Discharge- Voltages as an Indicator of the Onset of Unwanted Lithium Deposition in Lithium-Ion Cells. *J. Electrochem. Soc.* **2018**, *165* (16), A3595–A3601. <https://doi.org/10.1149/2.0011816jes>.
- (109) Day, R. P.; Xia, J.; Petibon, R.; Rucska, J.; Wang, H.; Wright, A. T. B.; Dahn, J. R. Differential Thermal Analysis of Li-Ion Cells as an Effective Probe of Liquid Electrolyte Evolution during Aging. *J. Electrochem. Soc.* **2015**, *162* (14), A2577–A2581. <https://doi.org/10.1149/2.0181514jes>.

- (110) Rupich, M. W.; Pitts, L.; Abraham, K. M. Characterization of Reactions and Products of the Discharge and Forced Overdischarge of Li / SO₂ Cells. *J. Electrochem. Soc.* **1982**, *129* (9), 1857–1861. <https://doi.org/10.1149/1.2124314>.
- (111) Hornak, J. The Basics of NMR <https://www.cis.rit.edu/htbooks/nmr/> (accessed Mar 6, 2021).
- (112) Keeler, J. Understanding NMR Spectroscopy <http://www-keeler.ch.cam.ac.uk/lectures/Irvine/> (accessed Mar 6, 2021).
- (113) Kitson, F.; Larsen, B.; McEwen, C. *Gas Chromatography and Mass Spectrometry: A Practical Guide*; Academic Press.: San Diego, CA, 1996.
- (114) Poole, C. *Gas Chromatography*; Elsevier Inc.: Waltham, MA, 2012.
- (115) Ashcroft, A.; Barnett, N. *Ionization Methods in Organic Mass Spectrometry*; Royal Society of Chemistry: Cambridge, UK, 1997.
- (116) Valente, I. M.; Gonçalves, L. M.; Rodrigues, J. A. Another Glimpse over the Salting-out Assisted Liquid-Liquid Extraction in Acetonitrile/Water Mixtures. *J. Chromatogr. A* **2013**, *1308*, 58–62. <https://doi.org/10.1016/j.chroma.2013.08.014>.
- (117) Haschke, M. *Laboratory Micro-X-Ray Fluorescence Spectroscopy*; Springer Series in Surface Sciences; Springer International Publishing: Cham, 2014; Vol. 55. <https://doi.org/10.1007/978-3-319-04864-2>.
- (118) Beckhoff, B.; Kanngießer, B.; Langhoff, N.; Wedell, R.; Wolff, H. *Handbook of Practical X-Ray Fluorescence Analysis*; Beckhoff, B., Kanngießer, habil. B., Langhoff, N., Wedell, R., Wolff, H., Eds.; Springer Berlin Heidelberg: Berlin, Heidelberg, 2006. <https://doi.org/10.1007/978-3-540-36722-2>.
- (119) Choi, W.; Manthiram, A. Comparison of Metal Ion Dissolutions from Lithium Ion Battery Cathodes. *J. Electrochem. Soc.* **2006**, *153* (9), A1760. <https://doi.org/10.1149/1.2219710>.
- (120) Strehle, B.; Solchenbach, S.; Metzger, M.; Schwenke, K. U.; Gasteiger, H. A. The Effect of CO₂ on Alkyl Carbonate Trans-Esterification during Formation of Graphite Electrodes in Li-Ion Batteries. *J. Electrochem. Soc.* **2017**, *164* (12), A2513–A2526. <https://doi.org/10.1149/2.1001712jes>.
- (121) Nelson, K. J.; d'Eon, G. L.; Wright, A. T. B.; Ma, L.; Xia, J.; Dahn, J. R. Studies of the Effect of High Voltage on the Impedance and Cycling Performance of Li[Ni_{0.4}Mn_{0.4}Co_{0.2}]O₂/Graphite Lithium-Ion Pouch Cells. *J. Electrochem. Soc.* **2015**, *162* (6), A1046–A1054. <https://doi.org/10.1149/2.0831506jes>.
- (122) Ma, X.; Harlow, J. E.; Li, J.; Ma, L.; Hall, D. S.; Buteau, S.; Genovese, M.; Cormier, M.; Dahn, J. R. Hindering Rollover Failure of Li[Ni_{0.5}Mn_{0.3}Co_{0.2}]O₂/Graphite Pouch Cells during Long-Term Cycling. *J. Electrochem. Soc.* **2019**, *166* (4), A711–A724. <https://doi.org/10.1149/2.0801904jes>.

- (123) Li, J.; Liu, H.; Xia, J.; Cameron, A. R.; Nie, M.; Botton, G. A.; Dahn, J. R. The Impact of Electrolyte Additives and Upper Cut-off Voltage on the Formation of a Rocksalt Surface Layer in $\text{LiNi}_{0.8}\text{Mn}_{0.1}\text{Co}_{0.1}\text{O}_2$ Electrodes. *J. Electrochem. Soc.* **2017**, *164* (4), A655–A665. <https://doi.org/10.1149/2.0651704jes>.
- (124) Li, W. Review—An Unpredictable Hazard in Lithium-Ion Batteries from Transition Metal Ions: Dissolution from Cathodes, Deposition on Anodes and Elimination Strategies. *J. Electrochem. Soc.* **2020**, *167* (9), 090514. <https://doi.org/10.1149/1945-7111/ab847f>.
- (125) Stich, M.; Göttlinger, M.; Kurniawan, M.; Schmidt, U.; Bund, A. Hydrolysis of LiPF_6 in Carbonate-Based Electrolytes for Lithium-Ion Batteries and in Aqueous Media. *J. Phys. Chem. C* **2018**, *122* (16), 8836–8842. <https://doi.org/10.1021/acs.jpcc.8b02080>.
- (126) Liu, Y.; Harlow, J.; Dahn, J. Microstructural Observations of “Single Crystal” Positive Electrode Materials Before and After Long Term Cycling by Cross-Section Scanning Electron Microscopy. *J. Electrochem. Soc.* **2020**, *167* (2), 020512. <https://doi.org/10.1149/1945-7111/ab6288>.
- (127) Li, H.; Liu, A.; Zhang, N.; Wang, Y.; Yin, S.; Wu, H.; Dahn, J. R. An Unavoidable Challenge for Ni-Rich Positive Electrode Materials for Lithium-Ion Batteries. *Chem. Mater.* **2019**, *31* (18), 7574–7583. <https://doi.org/10.1021/acs.chemmater.9b02372>.
- (128) Kim, H.; Grugeon, S.; Gachot, G.; Armand, M.; Sannier, L.; Laruelle, S. Ethylene Bis-Carbonates as Telltales of SEI and Electrolyte Health, Role of Carbonate Type and New Additives. *Electrochim. Acta* **2014**, *136*, 157–165. <https://doi.org/10.1016/j.electacta.2014.05.072>.
- (129) Petibon, R. Study of the Reactivity of Electrolyte Solvents and Additives in Li-Ion Cells and Design of New Electrolyte Blends, Dalhousie University, 2016.
- (130) Ellis, L. D.; Buteau, S.; Hames, S. G.; Thompson, L. M.; Hall, D. S.; Dahn, J. R. A New Method for Determining the Concentration of Electrolyte Components in Lithium-Ion Cells, Using Fourier Transform Infrared Spectroscopy and Machine Learning. *J. Electrochem. Soc.* **2018**, *165* (2), A256–A262. <https://doi.org/10.1149/2.0861802jes>.
- (131) Zhang, S. S. A Review on Electrolyte Additives for Lithium-Ion Batteries. *J. Power Sources* **2006**, *162* (2 SPEC. ISS.), 1379–1394. <https://doi.org/10.1016/j.jpowsour.2006.07.074>.
- (132) Gireaud, L.; Grugeon, S.; Laruelle, S.; Pilard, S.; Tarascon, J.-M. Identification of Li Battery Electrolyte Degradation Products Through Direct Synthesis and Characterization of Alkyl Carbonate Salts. *J. Electrochem. Soc.* **2005**, *152* (5), A850. <https://doi.org/10.1149/1.1872673>.

- (133) Sloop, S. E.; Pugh, J. K.; Wang, S.; Kerr, J. B.; Kinoshita, K. Chemical Reactivity of PF₅ and LiPF₆ in Ethylene Carbonate/Dimethyl Carbonate Solutions. *Electrochem. Solid-State Lett.* **2001**, *4* (4), 42–45. <https://doi.org/10.1149/1.1353158>.
- (134) Sloop, S. E.; Kerr, J. B.; Kinoshita, K. The Role of Li-Ion Battery Electrolyte Reactivity in Performance Decline and Self-Discharge. *J. Power Sources* **2003**, *119–121*, 330–337. [https://doi.org/10.1016/S0378-7753\(03\)00149-6](https://doi.org/10.1016/S0378-7753(03)00149-6).
- (135) Jarry, A.; Gottis, S.; Yu, Y. S.; Roque-Rosell, J.; Kim, C.; Cabana, J.; Kerr, J.; Kosteci, R. The Formation Mechanism of Fluorescent Metal Complexes at the Li_xNi_{0.5}Mn_{1.5}O_{4.8}/Carbonate Ester Electrolyte Interface. *J. Am. Chem. Soc.* **2015**, *137* (10), 3533–3539. <https://doi.org/10.1021/ja5116698>.
- (136) Delacourt, C.; Kwong, A.; Liu, X.; Qiao, R.; Yang, W. L.; Lu, P.; Harris, S. J.; Srinivasan, V. Effect of Manganese Contamination on the Solid-Electrolyte-Interphase Properties in Li-Ion Batteries. *J. Electrochem. Soc.* **2013**, *160* (8), A1099–A1107. <https://doi.org/10.1149/2.035308jes>.
- (137) Kuang, Y.; Chen, C.; Kirsch, D.; Hu, L. Thick Electrode Batteries: Principles, Opportunities, and Challenges. *Adv. Energy Mater.* **2019**, *9* (33), 1–19. <https://doi.org/10.1002/aenm.201901457>.
- (138) Kremer, L. S.; Hoffmann, A.; Danner, T.; Hein, S.; Prifling, B.; Westhoff, D.; Dreer, C.; Latz, A.; Schmidt, V.; Wohlfahrt-Mehrens, M. Manufacturing Process for Improved Ultra-Thick Cathodes in High-Energy Lithium-Ion Batteries. *Energy Technol.* **2020**, *8* (2), 1–14. <https://doi.org/10.1002/ente.201900167>.
- (139) Kim, H.; Oh, S. K.; Lee, J.; Doo, S. W.; Kim, Y.; Lee, K. T. Failure Mode of Thick Cathodes for Li-Ion Batteries: Variation of State-of-Charge along the Electrode Thickness Direction. *Electrochim. Acta* **2021**, *370*, 137743. <https://doi.org/10.1016/j.electacta.2021.137743>.
- (140) Zheng, H.; Li, J.; Song, X.; Liu, G.; Battaglia, V. S. A Comprehensive Understanding of Electrode Thickness Effects on the Electrochemical Performances of Li-Ion Battery Cathodes. *Electrochim. Acta* **2012**, *71*, 258–265. <https://doi.org/10.1016/j.electacta.2012.03.161>.
- (141) Li, G.; Ouyang, T.; Xiong, T.; Jiang, Z.; Adekoya, D.; Wu, Y.; Huang, Y.; Balogun, M.-S. (Jie T. All-Carbon-Frameworks Enabled Thick Electrode with Exceptional High-Areal-Capacity for Li-Ion Storage. *Carbon N. Y.* **2021**, *174*, 1–9. <https://doi.org/10.1016/j.carbon.2020.12.018>.
- (142) Dahn, J. R. Rechargeable LiNiO₂/Carbon Cells. *J. Electrochem. Soc.* **1991**, *138* (8), 2207–2211.
- (143) Thompson, L. M.; Harlow, J. E.; Eldesoky, A.; Bauer, M. K. G.; Cheng, J. H.; Stone, W. S.; Taskovic, T.; McFarlane, C. R. M.; Dahn, J. R. Study of Electrolyte and Electrode Composition Changes vs Time in Aged Li-Ion Cells. *J. Electrochem. Soc.* **2021**, *168* (2), 020532. <https://doi.org/10.1149/1945-7111/abe1da>.

- (144) Ohzuku, T.; Ueda, A.; Yamamoto, N.; Iwakoshi, Y. Factor Affecting the Capacity Retention of Lithium-Ion Cells. *J. Power Sources* **1995**, *54* (1), 99–102. [https://doi.org/10.1016/0378-7753\(94\)02047-7](https://doi.org/10.1016/0378-7753(94)02047-7).
- (145) Li, J.; Glazier, S. L.; Nelson, K.; Ma, X.; Harlow, J.; Paulsen, J.; Dahn, J. R. Effect of Choices of Positive Electrode Material, Electrolyte, Upper Cut-Off Voltage and Testing Temperature on the Life Time of Lithium-Ion Cells. *J. Electrochem. Soc.* **2018**, *165* (13), A3195–A3204. <https://doi.org/10.1149/2.0931813jes>.
- (146) Xiong, D. J.; Ellis, L. D.; Petibon, R.; Hynes, T.; Liu, Q. Q.; Dahn, J. R. Studies of Gas Generation, Gas Consumption and Impedance Growth in Li-Ion Cells with Carbonate or Fluorinated Electrolytes Using the Pouch Bag Method. *J. Electrochem. Soc.* **2017**, *164* (2), A340–A347. <https://doi.org/10.1149/2.1091702jes>.
- (147) Liu, Q. Q.; Petibon, R.; Du, C. Y.; Dahn, J. R. Effects of Electrolyte Additives and Solvents on Unwanted Lithium Plating in Lithium-Ion Cells. *J. Electrochem. Soc.* **2017**, *164* (6), A1173–A1183. <https://doi.org/10.1149/2.1081706jes>.
- (148) Hall, D. S.; Eldesoky, A.; Logan, E. R.; Tonita, E. M.; Ma, X.; Dahn, J. R. Exploring Classes of Co-Solvents for Fast-Charging Lithium-Ion Cells. *J. Electrochem. Soc.* **2018**, *165* (10), A2365–A2373. <https://doi.org/10.1149/2.1351810jes>.

APPENDIX A – SUPPLEMENTAL FIGURES

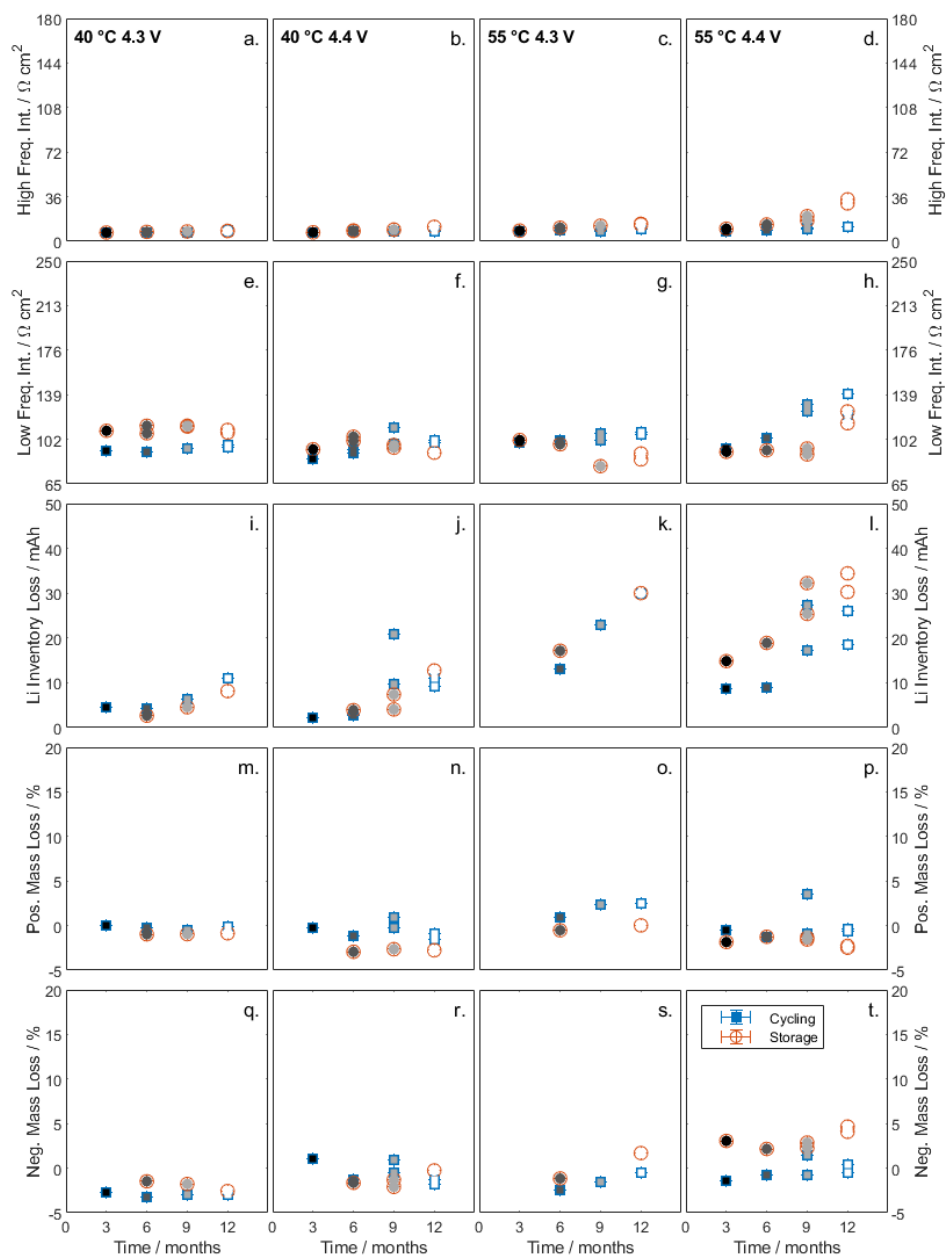


Figure A-1 – Post-cycling/storage results from NMC532 cycled and stored cells (blue squares and orange circles, respectively) are presented versus time. Panels (a.-d.) include the cycling/storage conditions for the panels that follow below. Panels (a.-d.) show the high frequency intercept and panels (e.-h.) show the low frequency intercept measured via EIS. Panels (i.-l.) show Li inventory loss and panels (m.-p.) show the positive electrode slippage measured via UHPC. Panels (q.-t.) show the estimated positive electrode mass loss percent measured via UHPC.

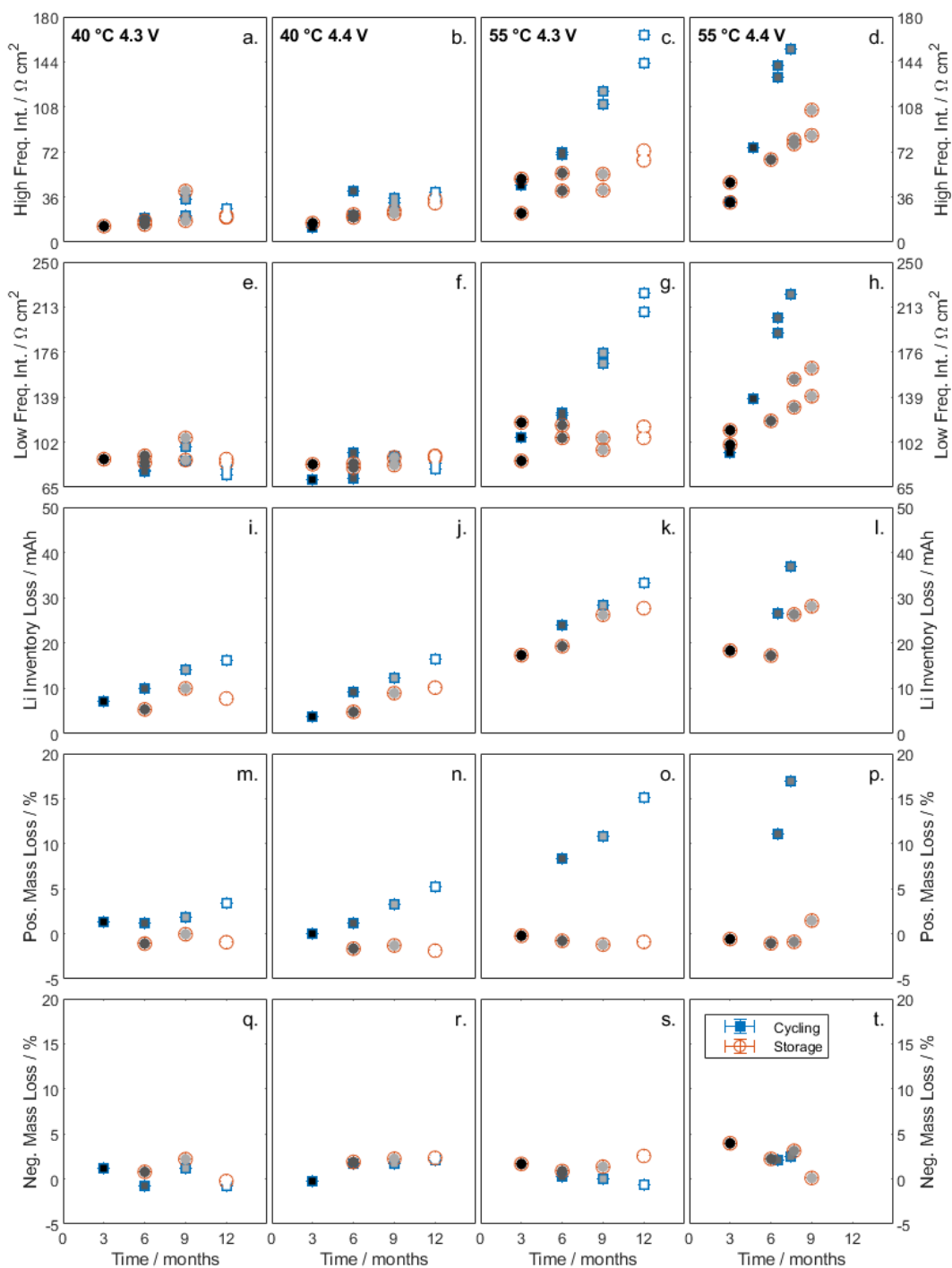


Figure A-2 – Post-cycling/storage results from NMC622 cycled and stored cells (blue squares and orange circles, respectively) are presented versus time. Panels (a.-d.) include the cycling/storage conditions for the panels that follow below. Panels (a.-d.) show the high frequency intercept and panels (e.-h.) show the low frequency intercept measured via EIS. Panels (i.-l.) show Li inventory loss and panels (m.-p.) show the positive electrode mass loss measured via UHPC. Panels (q.-t.) show the estimated negative electrode mass loss percent measured via UHPC.

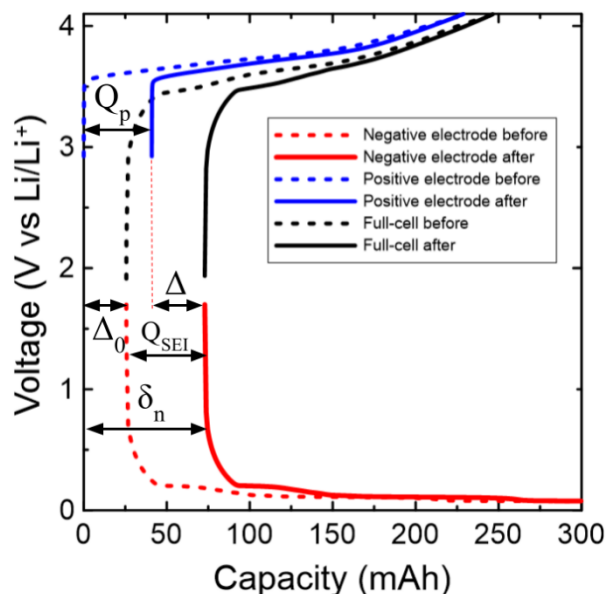


Figure A-3 – Example of voltage versus capacity curves (determined from dV/dQ analysis) from before cycling (dashed line) and after cycling (solid line) for positive electrode (red), negative electrode (blue), and full-cell (black). Lithium inventory loss (Q_{SEI}) can be obtained from this data by summing the absolute positive electrode slippage (Q_p) with full-cell slippage after cycling (Δ) and subtracting the full cell slippage before cycling (Δ_0) or from subtracting the negative electrode slippage before cycling (δ_{n0}) from the negative electrode slippage after cycling (δ_n). This can be summarized in the following Equation(s) A-1:

$$Q_{SEI} = (\Delta - \Delta_0) + Q_p = (\delta_n - \delta_{n0}) \quad (\text{A-1})$$

Positive electrode slippage after cycling can be calculated from the original capacity (Q_0) and the positive electrode mass before (m_{p0}) and after cycling (m_p) according to Equation A-2:

$$Q_p = Q_0 (1 - m_p/m_{p0}) \quad (\text{A-2})$$

This figure was reproduced with permission from R. Gauthier, submitted to *J. Electrochem Soc.* for publication.

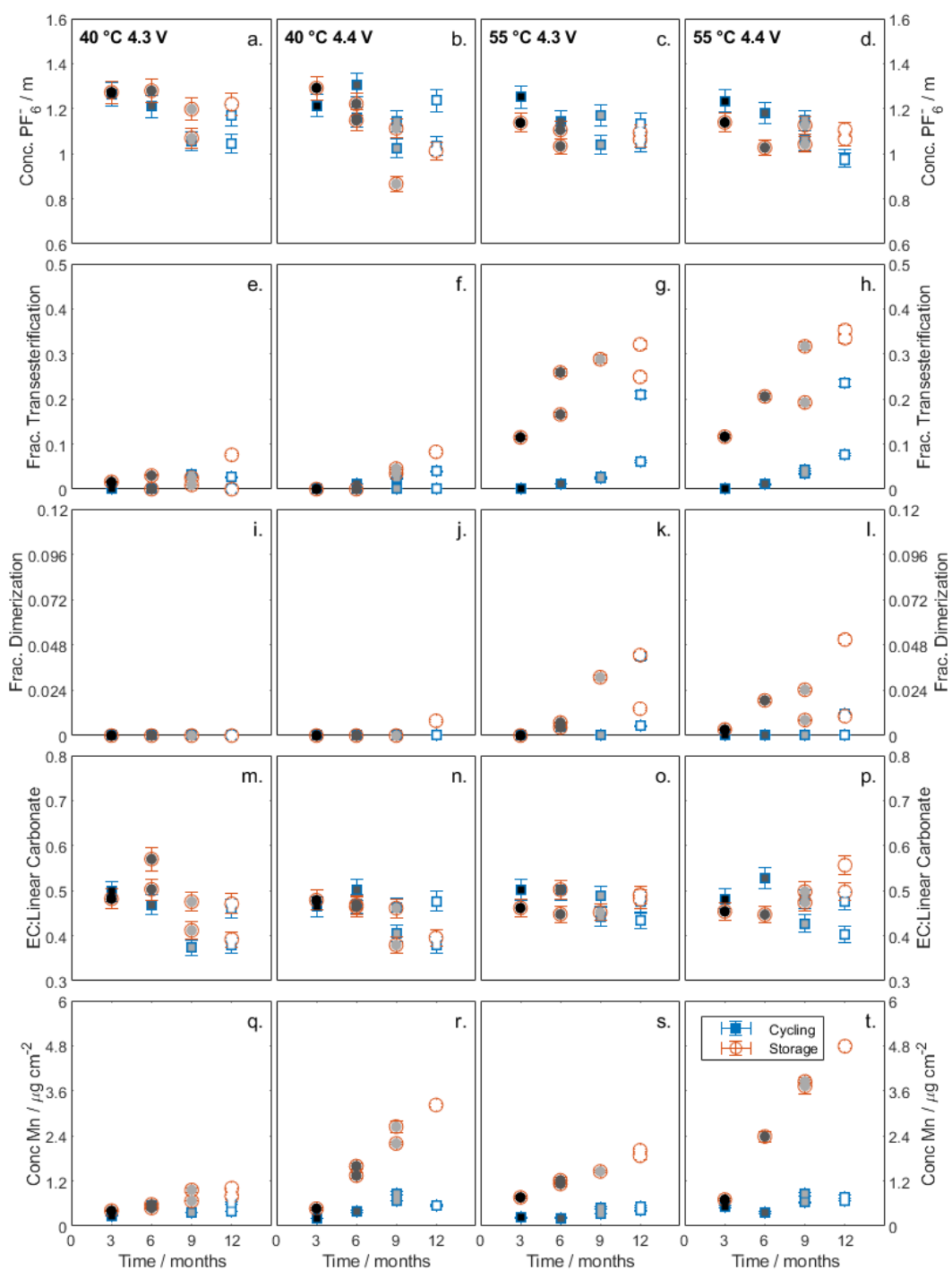


Figure A-4 – Electrode and electrolyte analysis results for NMC532 cycled and stored cells (blue squares and orange circles, respectively) are presented versus time. Panels (a.-d.) include the cycling/storage conditions for the panels that follow below. Panels (a.-d.) show the calculated PF_6^- concentration in the electrolyte. Panels (e.-h.) show the fraction of transesterification and panels (i.-l.) show the fraction of dimerization. Panels (m.-p.) show the measured EC:linear carbonate ratio of electrolyte. Panels (q.-t.) show the Mn loading on the negative electrode.

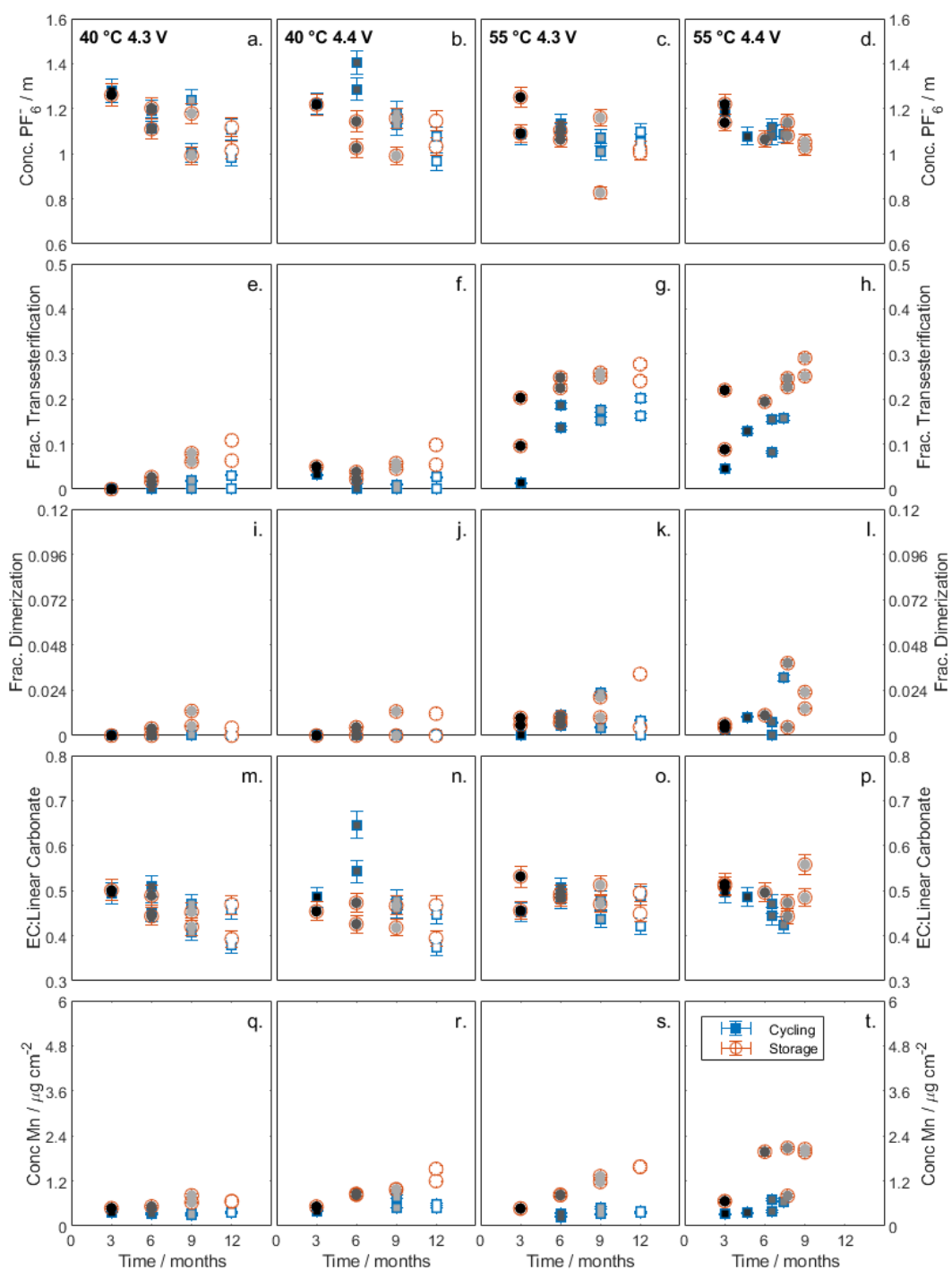


Figure A-5 – Electrode and electrolyte analysis results for NMC622 cycled and stored cells (blue squares and orange circles, respectively) are presented versus time. Panels (a.-d.) include the cycling/storage conditions for the panels that follow below. Panels (a.-d.) show the calculated PF_6^- concentration in the electrolyte. Panels (e.-h.) show the fraction of transesterification and panels (i.-l.) show the fraction of dimerization. Panels (m.-p.) show the measured EC:linear carbonate ratio of electrolyte. Panels (q.-t.) show the Mn loading at the negative electrode.

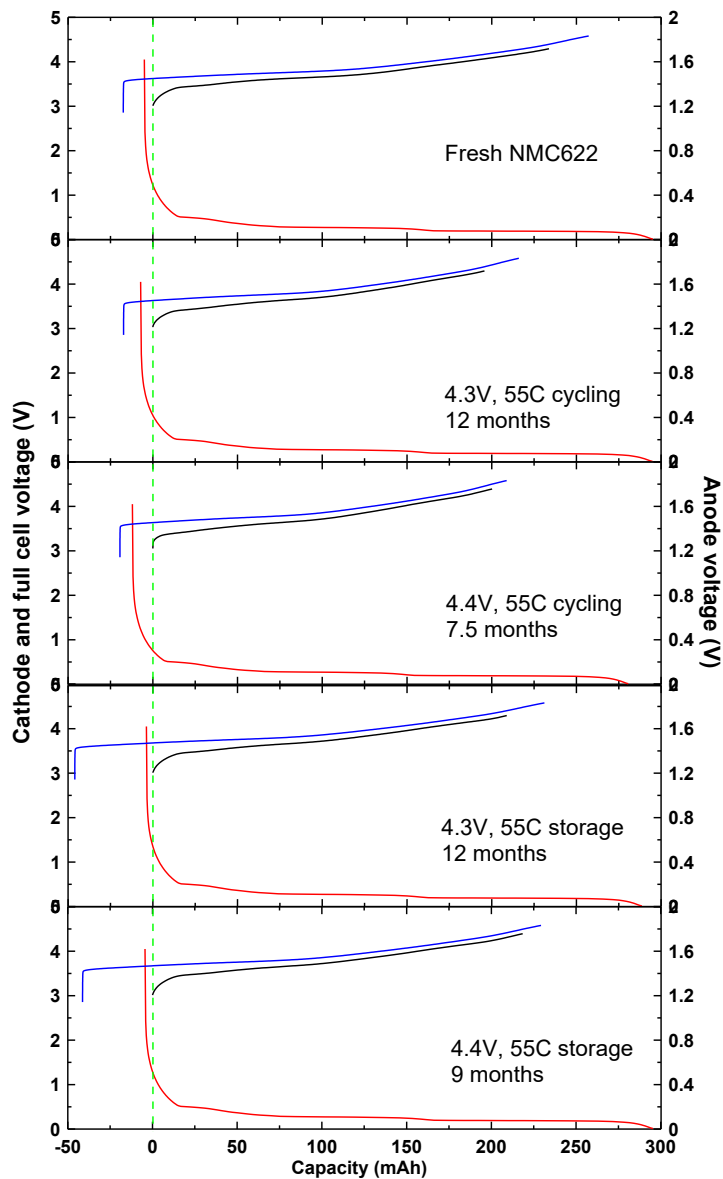


Figure A-6 – Illustration showing electrode capacities and alignment as determined using dV/dQ analysis from fresh NMC622 cell (a.), cycled cells (b. and c.) (4.3 V and 4.4 V UCP, respectively), and stored cells (d. and e.) (4.3 V and 4.4 V UCP, respectively) at 55°C. This figure was produced by J. Harlow for publication in *J. Electrochem Soc.* 168, 020532 (2021).

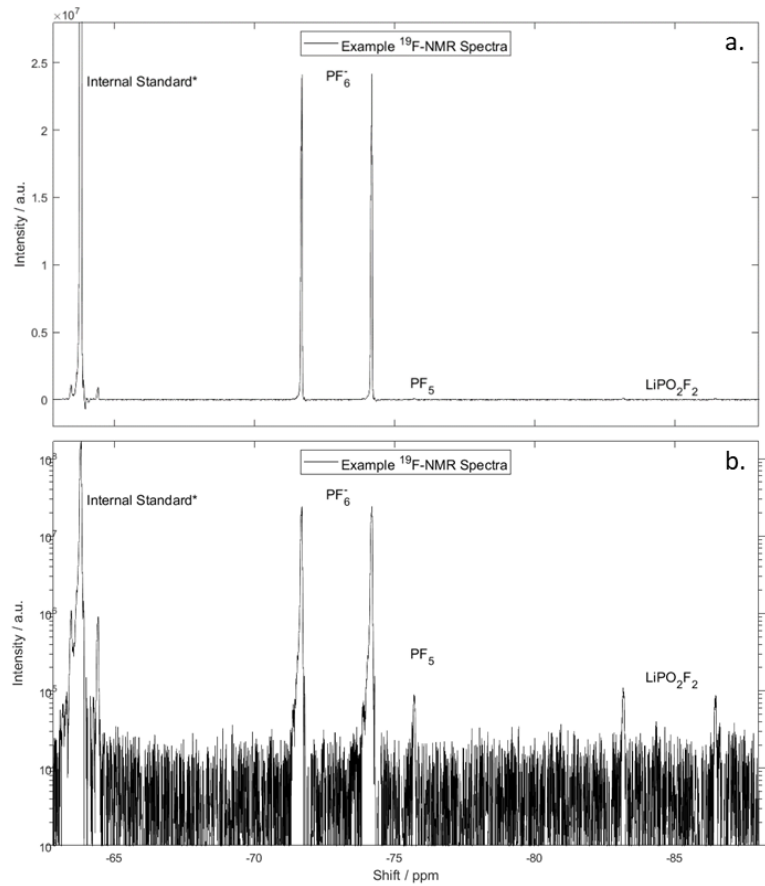


Figure A-7 – Example of ^{19}F -NMR spectra with linear scale (a.) and logarithmic scale (b.) to show minor PF_5 (attributed to contamination) and LiPO_2F_2 peaks

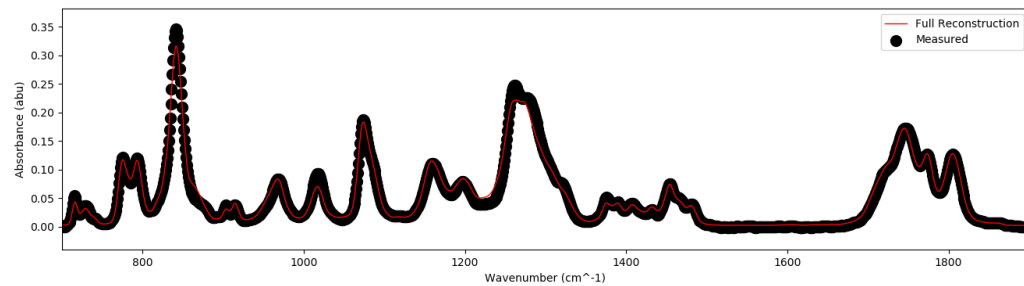


Figure A-8 – FTIR measured (black dots) and reconstructed fit (red).

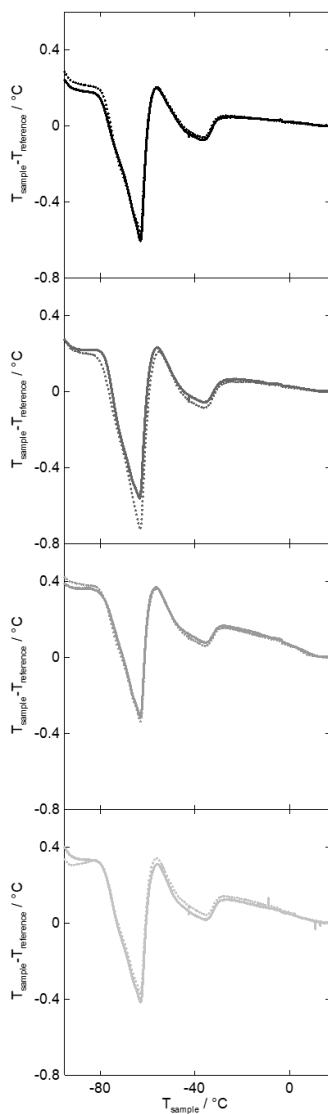


Figure A-9 – All results from DTA on NMC532 cells cycled at 40°C to an upper cutoff of 4.4 V. Time of testing is represented by line color ranging from 3 to 12 (black to grey, respectively). Pair cell tests are represented by dashed lines. Figure produced by M. Bauer for publication in *J. Electrochem Soc.* 168, 020532 (2021).

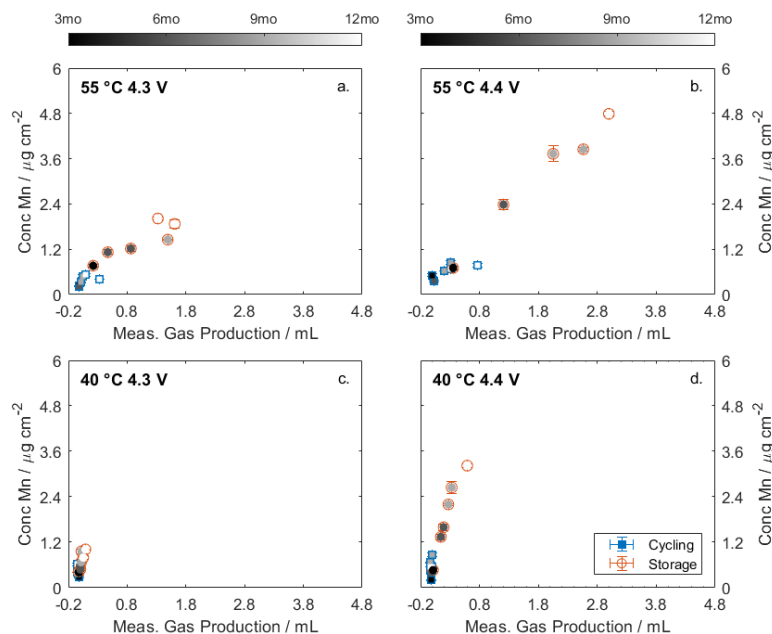


Figure A-10 – The concentration of Mn measured on the negative electrode is shown versus measured gas produced in NMC532 cycled (blue squares) and stored cells (orange circles). Time of cycling/storage is represented in the fill color ranging from black to white (3 mo. and 12 mo., respectively). Cycling/storage conditions are shown in the top left of each graph.

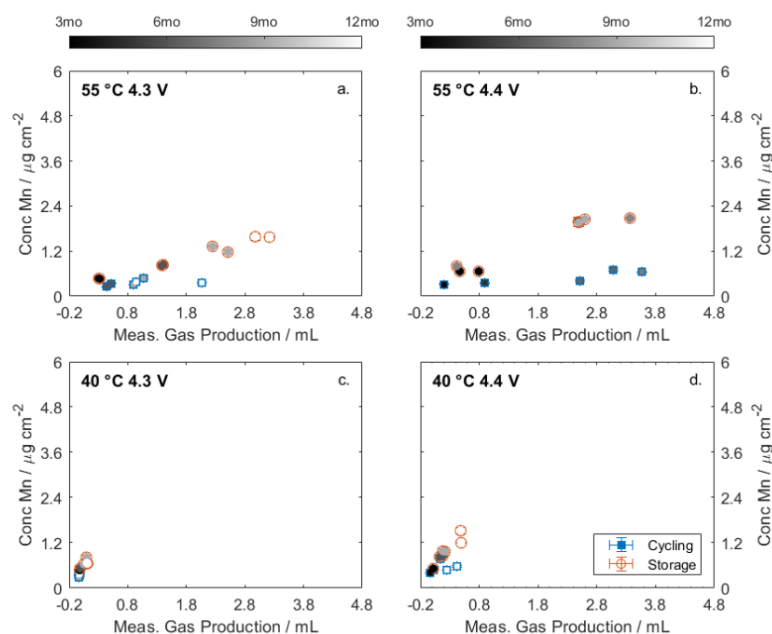


Figure A-11 – The concentration of Mn measured on the negative electrode is shown versus measured gas produced in NMC622 cycled (blue squares) and stored cells (orange circles). Time of cycling/storage is represented in the fill color ranging from black to white (3 mo. and 12 mo., respectively). Cycling/storage conditions are shown in the top left of each graph.

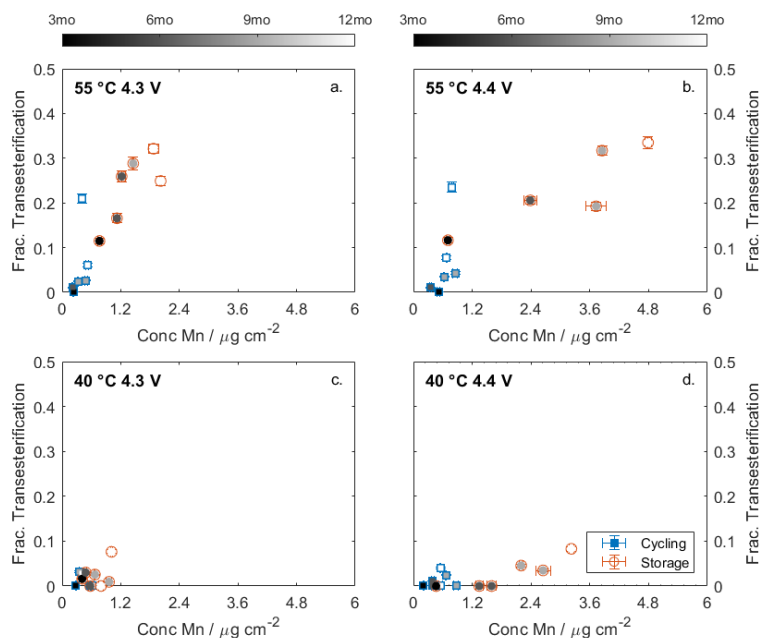


Figure A-12 – The fraction of transesterification is shown versus concentration of Mn measured on the negative electrode of NMC532 cycled (blue squares) and stored cells (orange circles). Time of cycling/storage is represented in the fill color ranging from black to white (3 mo. and 12 mo., respectively). Cycling/storage conditions are shown in the top left of each graph.

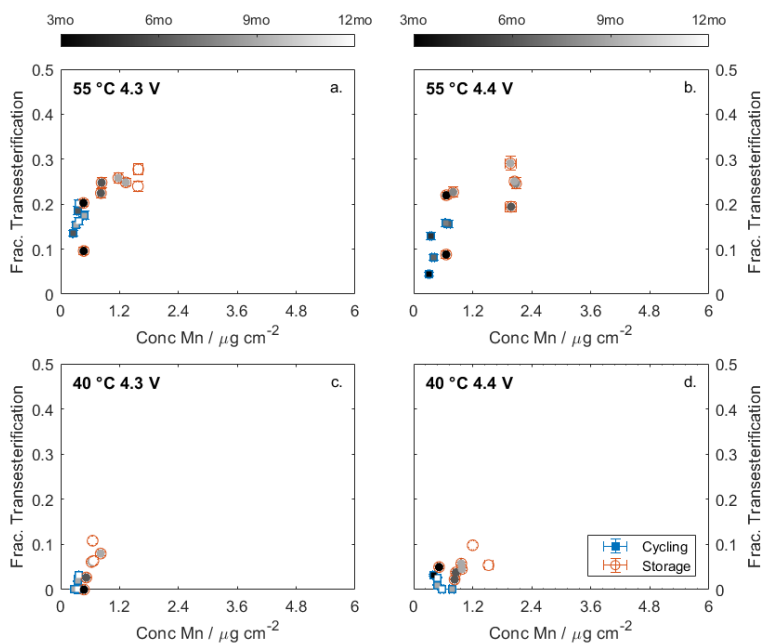


Figure A-13 – The fraction of transesterification is shown versus concentration of Mn measured on the negative electrode of NMC622 cycled (blue squares) and stored cells (orange circles). Time of cycling/storage is represented in the fill color ranging from black to white (3 mo. and 12 mo., respectively). Cycling/storage conditions are shown in the top left of each graph.

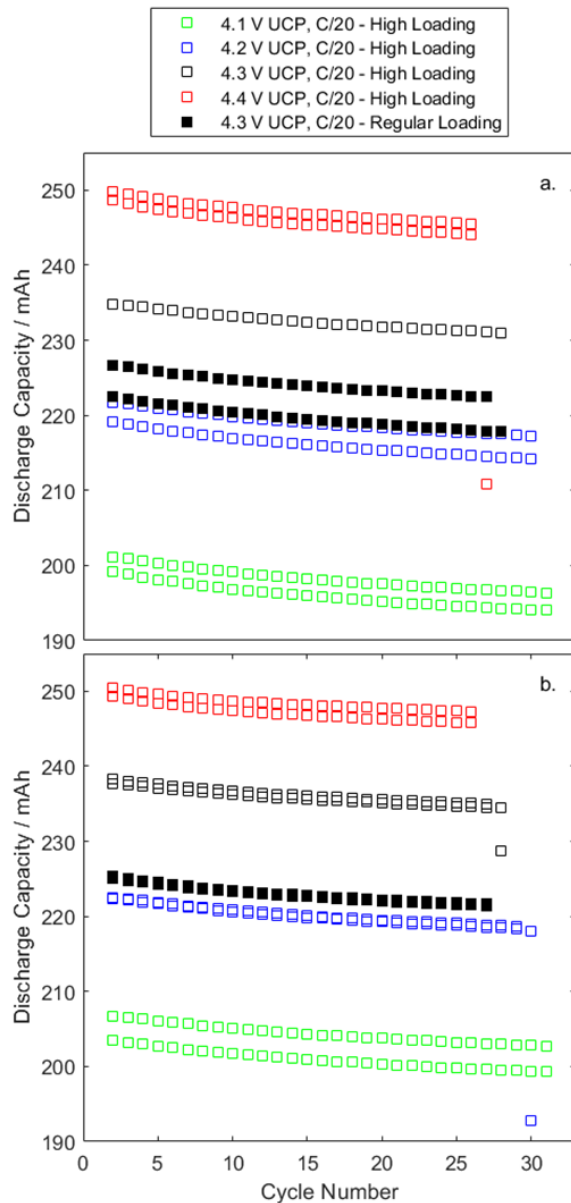


Figure A-14 – Absolute discharge capacity versus cycle number for cells with high (open squares) and regular loading (solid squares) at various upper cutoff potentials 4.1, 4.2, 4.3, and 4.4 V (green, blue, black, and red, respectively). Cells containing additives 2% FEC and 1% LiPO₂F₂ are shown in panel (a.) and cells containing additives 2% VC and 1% DTD are shown in panel (b.). The testing was performed using the UHPC at C/20 and 40°C.

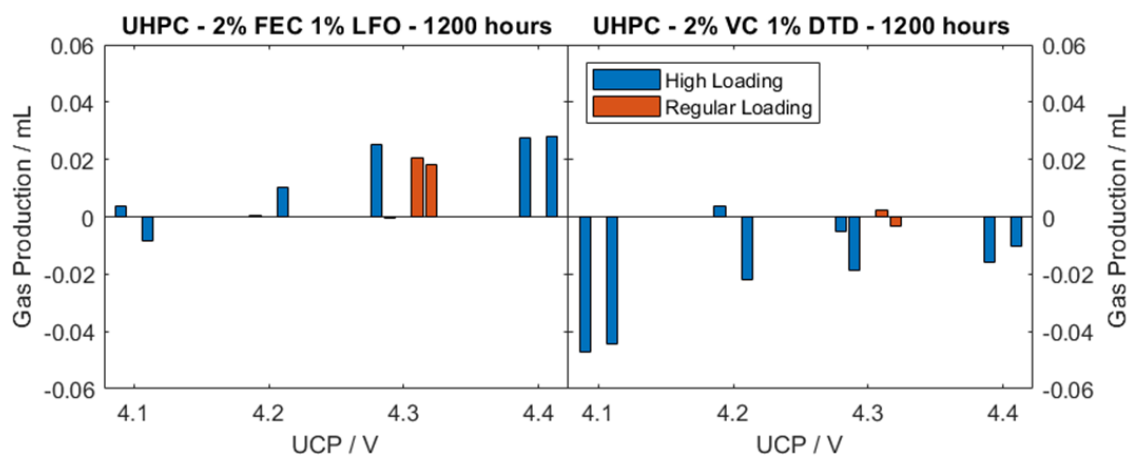


Figure A-15 – Gas production measured after 1200 h of cycling on UHPC. Panel (a.) shows the change in gas volume versus designated UCP for cells containing 2% FEC and 1% LiPO₂F₂. Panel (b.) shows the change in gas volume versus designated UCP for cells containing additives 2% VC and 1% DTD.

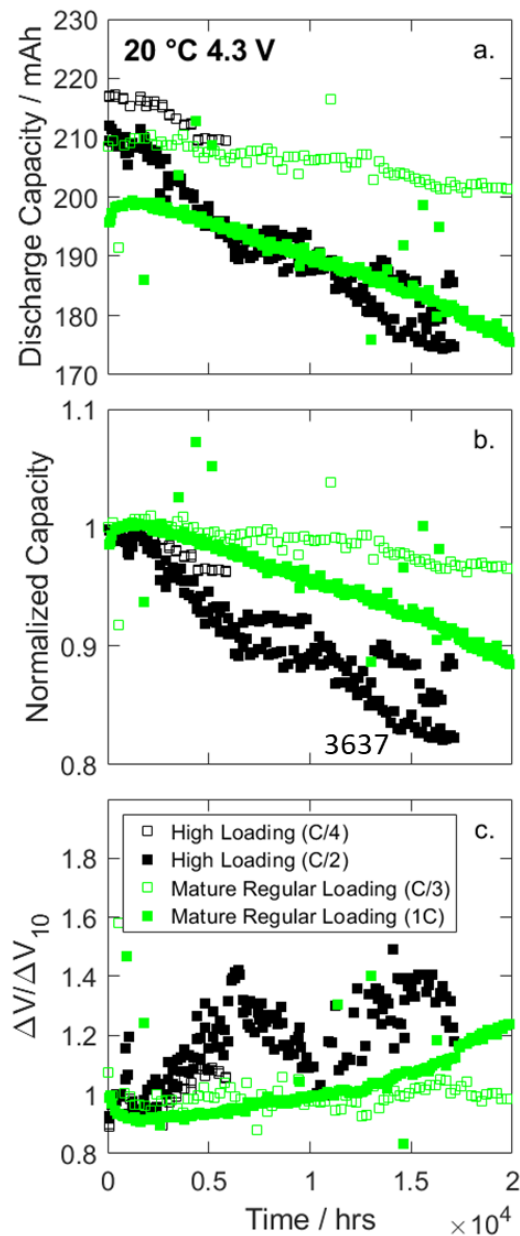


Figure A-16 – Extended cycling results for cells containing additives 2% FEC and 1% LiPO₂F₂. Panel (a.) shows absolute discharge capacity versus time and panel (b.) shows normalized capacity versus time for the cells with high electrode loading (black, at C/2) and mature cells with regular loading (green, at C/3 and 1C as indicated in legend). The cycle number for the high loading cells are shown in black on panel (b.). Panel (c.) shows the voltage polarization versus time for these cells.

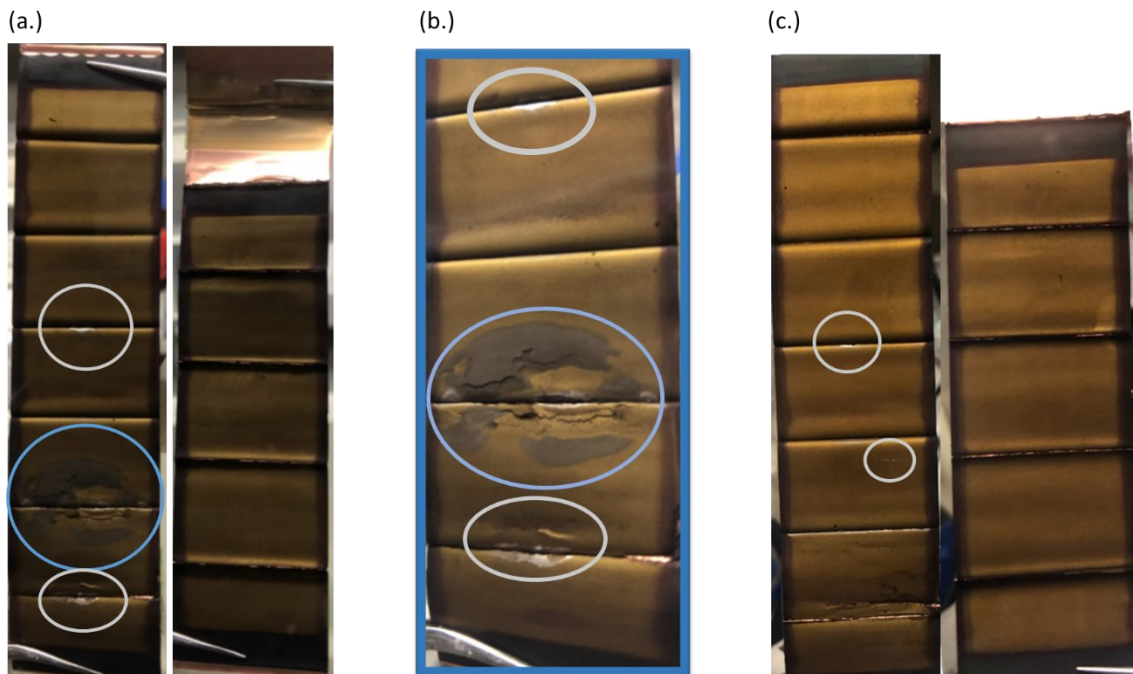


Figure A-17 – Photos of negative electrodes removed from cells with high loading cycled at $C/2$ C-rate. Panel (a.) shows electrodes from cells with additives 2% FEC and 1% LiPO_2F_2 . Panel (b.) shows a closer view of panel (a.). Panel (c.) shows negative electrodes from cells with 2% VC and 1% DTD additives. Photos taken with help from J. Harlow.

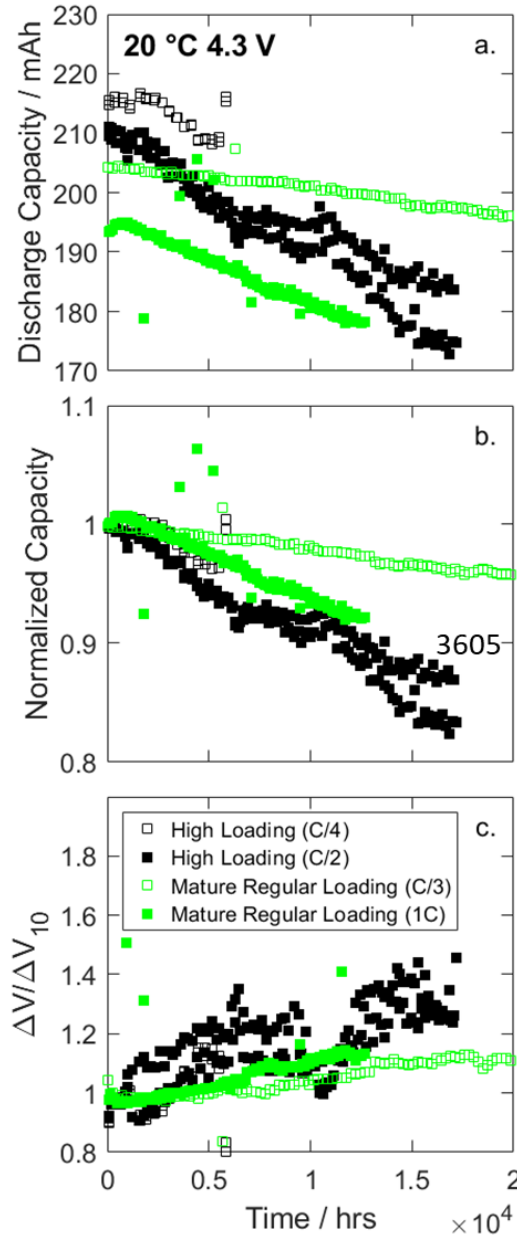


Figure A-18 – Extended cycling results for cells containing additives 2% VC and 1% DTD. Panel (a.) shows absolute discharge capacity versus time and panel (b.) shows normalized capacity versus time for the cells with high electrode loading (black, at C/2) and mature cells with regular loading (green, at C/3 and 1C as indicated in legend). The cycle number for the high loading cells are shown in black on panel (b.). Panel (c.) shows the voltage polarization versus time for these cells.

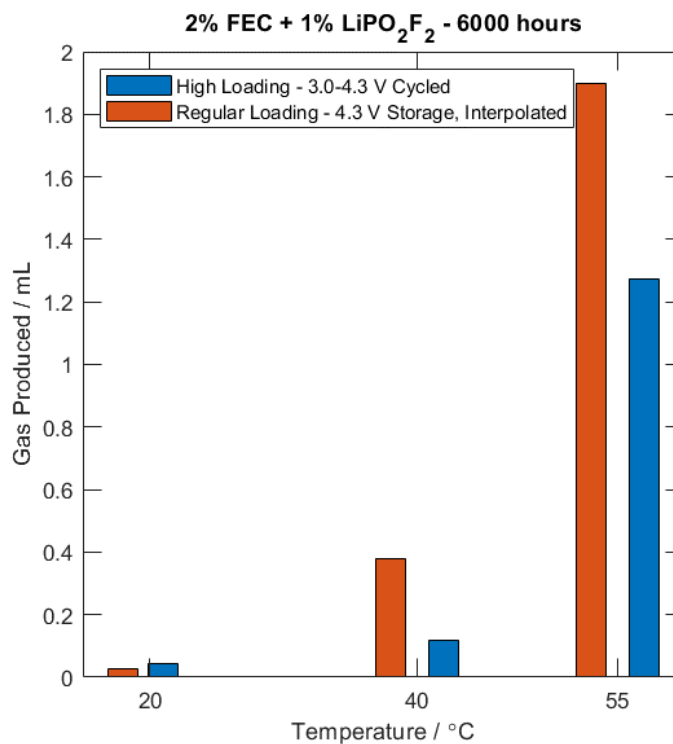


Figure A-19 – Examples of gas produced from cycled high loading cells (3.0 to 4.3 V) containing 2% FEC + 1% LiPO₂F₂ from this study (blue) and *interpolated gas produced after 6000h* from stored regular loading cells containing 2% FEC +1% LiPO₂F₂ /1% LiPO₂F₂ from previous studies at Dahn Lab (red) at 20, 40, and 55 °C.

APPENDIX B – TABLE OF CHEMICALS

Table B-0-1 – Table of reagents used in electrolyte construction and in GC-MS/NMR calibration and verification.

<u>Name</u>	<u>Abbreviation</u>	<u>Source</u>	<u>Purity Notes</u>
Ethyl methyl carbonate	EMC	BASF, USA/ Capchem, China	99.99%, H ₂ O < 14 ppm
Dimethyl carbonate	DMC	Capchem, China	99.95%
Diethyl carbonate	DEC	Capchem, China	99.95% H ₂ O < 20ppm
Ethylene carbonate	EC	BASF, USA/	99.95%, H ₂ O < 10 ppm
Lithium hexafluorophosphate	LiPF ₆	BASF, USA/ Capchem, China	99.94%, H ₂ O < 20 ppm
Vinylene carbonate	VC	Capchem, China	99.5%, H ₂ O < 100 ppm
Fluoroethylene carbonate	FEC	Capchem, China	99.94%
Methylene methane disulfonate	MMDS	Tinci Mat., China	>98.7%
Ethylene sulfite	DTD	Sigma Aldrich, USA	98%
Lithium difluorophosphate	LiPO ₂ F ₂	Capchem, China	>99.8%
Dimethyl-2,5-dioxahexane carboxylate	DMOHC	Tinci Mat., China	>98%
Diethyl-2,5-dioxahexane carboxylate	DEOHC	Tinci Mat., China	>98%
Methyl acetate	MA	BASF, USA/ Capchem, China	> 99.95% H ₂ O < 20 ppm

APPENDIX C – COPYRIGHT STATEMENT



TRANSFER OF COPYRIGHT AGREEMENT (revised August 2015)

The Electrochemical Society (ECS)

65 South Main Street, Pennington, NJ 08534-2839, USA

E-mail: publications@electrochem.org; Fax: 1.609.730.0629

Thank you for submitting your Work for publication. In order to expedite the publishing process and enable ECS to disseminate your work to the fullest extent, we need to have this Agreement signed and returned to us as soon as possible. If the Work is not accepted for publication this Agreement shall be null and void.

Article entitled (the "Work"): _____

ECS System Tracking # _____

Submitted by the following author(s) (list all authors) ("Author(s)"): _____

for publication in (check one):

Interface *ECS Transactions* *Journal of The Electrochemical Society (JES)* *ECS Journal of Solid State Science and Technology (JSS)*

1. **Transfer** — In consideration of ECS agreeing to publish the Work, the Authors grant to ECS for the full term of copyright in the Work and any extensions to the term, the exclusive right to (a) publish, reproduce, distribute, display, and store the Work in all forms, formats, and media now known or later developed (including without limitation in print, digital, and electronic form) throughout the world; (b) translate the Work into other languages, create adaptations, summaries or extracts of the Work or other derivative works based on the Work and exercise all of the rights set forth in (a) above in such translations, adaptations, summaries, extracts, and derivative works; and (c) license others to do any or all of the above. All accepted Works become the property of ECS and may not be published elsewhere without prior written permission of ECS, except as noted in Section 2 below.
2. **Rights of Authors** — The Author(s), and in the case of a Work Made for Hire as defined in the U.S. Copyright Code, 17 U.S.C. §101, the employer named below, shall retain the following nonexclusive rights (the "Author Rights"):
 - a. All other proprietary rights not transferred to ECS, such as patent rights.
 - b. The nonexclusive right, after publication by ECS, to give permission to third parties to republish print versions of the Article or a translation thereof, or excerpts therefrom, without obtaining permission from ECS, provided the ECS-formatted version is not used for this purpose and provided the Article is not to be published in another journal. If the ECS version is used, permission from ECS must be obtained.
 - c. The right, after publication by ECS, to use all or part of the Article without revision or modification, including the ECS-formatted version, in print compilations or other print publications of the author(s)' and/or the employer's own works, and on the author(s)' and/or the employer's website, and to make copies of all or part of the Article for the author(s)' and/or the employer's use for lecture or classroom purposes; provided that the copyright notices are not removed and provided that copies are not offered for sale and are not distributed in a commercial way outside of Author(s)'s employing institution.
 - d. The right to post and update the Article on e-print servers as long as files prepared and/or formatted by ECS or its vendors are not used for that purpose. Any such posting made or updated after acceptance of the Article for publication shall include a link to the online abstract in the ECS publication of origin or to the entry page of that publication.
 - e. If the Article was prepared under a U.S. Government contract, the government shall have the rights under the copyright to the extent required by the contract.
3. **Required Copyright Notice** — All copies, paper or electronic, or other use of the Work in any form must include the following notice: "© The Electrochemical Society, Inc. [year]. All rights reserved. Except as provided under U.S. copyright law, this work may not be reproduced, resold, distributed, or modified without the express permission of The Electrochemical Society (ECS). The archival version of this work was published in [insert bibliographic information here]." Please refer requests for all uses not in Section 2 above to The Electrochemical Society.
4. **Warranties** — By signing this Agreement, the Author(s), and in the case of a Work Made for Hire, the employer, jointly and severally represent and warrant that (1) the Work is original with the Author(s); (2) does not infringe any copyright or violate any other right of any third parties; and (3) that the Work has not been published elsewhere, other than an ECS publication, and is not being considered for publication elsewhere in any form, except as provided herein. If each Author's signature does not appear below, the signing Author(s) represent that they sign this Agreement as authorized agents for and on behalf of all the Authors, and that this Agreement and authorization is made on behalf of all the authors. The signing Author(s) (and, in the case of a Work Made for Hire, the signing employer) also represent and warrant that they have the full power to enter into this Agreement and to make the grants contained herein. If excerpts from copyrighted works are included in the Work, the Author(s) have obtained or will obtain written permission from the copyright owners and will credit such sources in the Work.